Petrogenesis of Eocene calc-alkaline magmatism at Electric Peak and Sepulcher Mountain, Absaroka Volcanic Province, Montana and Wyoming
by Charles Roger Lindsay

A thesis submitted in partial fulfillment of the requirements for the degree of Master of Science in Earth Sciences
Montana State University

Abstract:
Electric Peak and Sepulcher Mountain represent the well-exposed intrusive and extrusive components of an early Eocene eruptive center in the Absaroka volcanic province of Montana and Wyoming. Geological field relationships, petrographic analysis, and mineral and whole rock geochemical compositions were used to investigate the petrogenesis of this eruptive center. The Electric Peak stock has an outcrop area of ~lkm3 and consists of six intrusive phases ranging in composition from quartz diorite to granite, representing multiple intrusions of compositionally distinct magmas. Stratigraphic constraints and Al-in-hornblende geobarometry indicate that these magmas stalled and solidified at a depth of ~3 km. Lava flows and dikes at Sepulcher Mountain are basaltic-andesitic to rhyolitic in composition and silicic rocks are peripheral to mafic rocks. Collectively, intrusive and extrusive rocks represent a medium- to high-K, calc-alkaline, comagmatic suite. Important geochemical characteristics of these rocks include high Ni and Cr concentrations in andesitic and dacitic rocks, lower rare earth element concentrations in evolved rocks relative to more mafic rocks, non-uniform Sr and Nd isotopic ratios, and strong relative depletions in high field strength elements relative to large ion lithophile elements. Although petrographic evidence permissive of magma mixing is limited, quantitative petrogenetic modeling demonstrates that intermediate composition rocks are hybrids formed by mixing of variably fractionated and contaminated mantle-derived mafic magmas with diverse composition crustal-derived silicic magmas and their differentiates. Chemical compositions indicate that mafic magmas were derived from ancient, enriched lithospheric mantle and that silicic magmas represent partial melts of amphibolitic crust leaving restites with variable modal mineralogy. The significance of these results is that a considerable crustal component was involved in generating Eocene calc-alkaline magmas in the Absaroka volcanic province.

PETROGENESIS OF EOCENE CALC-ALKALINE MAGMATISM AT ELECTRIC PEAK AND SEPULCHER MOUNTAIN, ABSAROKA VOLCANIC PROVINCE, MONTANA AND WYOMING

by

Charles Roger Lindsay

A thesis submitted in partial fulfillment
of the requirements for the degree

of

Master of Science

in

Earth Sciences

MONTANA STATE UNIVERSITY
Bozeman, Montana

January, 2002

APPROVAL

of a thesis submitted by

Charles Roger Lindsay

This thesis has been read by each member of the thesis committee and has been found to be satisfactory regarding content, English usage, format, citations, bibliographic style, and consistency, and is ready for submission to the College of Graduate Studies.

Dr. Todd C. Feeley ____________________ 1/28/02
Date

Approved for the Department of Earth Sciences

Dr. James G. Schmitt ____________________ 1/28/02
Date

Approved for the College of Graduate Studies

Dr. Bruce McLeod ____________________ 1-28-02
Date

STATEMENT OF PERMISSION TO USE

In presenting this thesis in partial fulfillment of the requirements for a master's degree at Montana State University, I agree that the Library shall make it available to borrowers under the rules of the Library.

If I have indicated my intention to copyright this thesis by including a copyright notice page, copying is allowable only for scholarly purposes, consistent with "fair use" as prescribed in the U.S. Copyright Law. Requests for permission for extended quotation from or reproduction of this thesis in whole or in parts may be granted only by the copyright holder.

Signature C. Lindsay

Date 1-28-02

ACKNOWLEDGMENTS

The National Science Foundation, the Geological Society of America, and Sigma-Xi Grants-in-Aid of Research generously provided support for this project. Thank you also to the Department of Earth Sciences at Montana State University and the Barry C. Bishop Scholarship for Mountain Research for additional funding. The Radiation Center at Oregon State University kindly provided the instrumental neutron activation analyses. Thank you to Roger Nielson and François Bussy for assistance with the electron microprobe. I thank Anita Varley and Kerry Gunther for their assistance and permission to conduct fieldwork in Yellowstone National Park. I am indebted to Alan Swanson for his able and cheerful assistance in the field despite thunderstorms, mosquitoes, and grizzly bears. Special thanks to Dr. David Blackwell, Dr. Gordon G. Goles, Dr. Edward Taylor, and Dr. Anita Grunder for inspiration. Dr. David Eggler, Dr. B. Carter Hearn, and Dr. Margaret Hiza provided valuable insight and thoughtful discussion. I thank Cal Ruleman and Dr. Tom Kalakay for stimulating discussions and support during difficult times. Thank you Eric Hammond for listening and believing. Thank you Grace Winer for taking care of me. I thank my committee members, Dr. Jim Schmitt and Dr. Dave Mogk, for their large commitment of both time and resources. I thank my advisor Dr. Todd Feeley for his unwavering support and patience; your advice and guidance have helped me grow as a student, teacher, and scientist. Thank you Katie Johnson –for everything. I thank my parents for their support and encouragement. I thank my grandmother for the curiosity that she inspired within me.

TABLE OF CONTENTS

TABLE OF CONTENTS – CONTINUED

TABLE OF CONTENTS – CONTINUED

LIST OF TABLES

LIST OF FIGURES

LIST OF FIGURES – CONTINUED

LIST OF FIGURES – CONTINUED

ABSTRACT

Electric Peak and Sepulcher Mountain represent the well-exposed intrusive and extrusive components of an early Eocene eruptive center in the Absaroka volcanic province of Montana and Wyoming. Geological field relationships, petrographic analysis, and mineral and whole rock geochemical compositions were used to investigate the petrogenesis of this eruptive center. The Electric Peak stock has an outcrop area of ~1km^3 and consists of six intrusive phases ranging in composition from quartz diorite to granite, representing multiple intrusions of compositionally distinct magmas. Stratigraphic constraints and Al-in-hornblende geobarometry indicate that these magmas stalled and solidified at a depth of ~3 km. Lava flows and dikes at Sepulcher Mountain are basaltic-andesitic to rhyolitic in composition and silicic rocks are peripheral to mafic rocks. Collectively, intrusive and extrusive rocks represent a medium- to high-K, calc-alkaline, comagmatic suite. Important geochemical characteristics of these rocks include high Ni and Cr concentrations in andesitic and dacitic rocks, lower rare earth element concentrations in evolved rocks relative to more mafic rocks, non-uniform Sr and Nd isotopic ratios, and strong relative depletions in high field strength elements relative to large ion lithophile elements. Although petrographic evidence permissive of magma mixing is limited, quantitative petrogenetic modeling demonstrates that intermediate composition rocks are hybrids formed by mixing of variably fractionated and contaminated mantle-derived mafic magmas with diverse composition crustal-derived silicic magmas and their differentiates. Chemical compositions indicate that mafic magmas were derived from ancient, enriched lithospheric mantle and that silicic magmas represent partial melts of amphibolitic crust leaving restites with variable modal mineralogy. The significance of these results is that a considerable crustal component was involved in generating Eocene calc-alkaline magmas in the Absaroka volcanic province.

CHAPTER 1

INTRODUCTION

A widespread magmatic event affected northwestern North America during the Eocene, emplacing several large igneous provinces throughout the Cordillera and adjacent foreland (Figure 1). The genesis of this magmatic activity remains poorly understood as reflected by the numerous contrasting models that have been proposed to account for it (e.g. Lipman and Glazner, 1991; Lipman, 1992). As one of the largest volcanic fields in this region, the Absaroka volcanic province (AVP; Figure 1) is similarly difficult to place in a proper tectonomagmatic context. Understanding the magmatic processes involved in the evolution of individual eruptive centers is critical to unraveling the origin of the volcanic field as a whole. Therefore, this study investigates the petrogenesis of Electric Peak and Sepulcher Mountain, the well-exposed intrusive and extrusive components of a moderate-volume, calc-alkaline, early Eocene eruptive center in the AVP. Specifically, the goals of this study are to (1) document the compositional ranges of extrusive and intrusive rocks present; (2) characterize the relationship between intrusive rocks at Electric Peak and extrusive rocks at Sepulcher Mountain; and (3) evaluate the possible roles of different petrogenetic processes in producing the compositional diversity of these rocks.

Electric Peak and Sepulcher Mountain were chosen for this study for two reasons. First, there are few contemporary petrologic studies of calc-alkaline eruptive centers in the AVP (Hiza, 1999; Feeley et al., *in press*). Second, intrusive bodies at Electric Peak

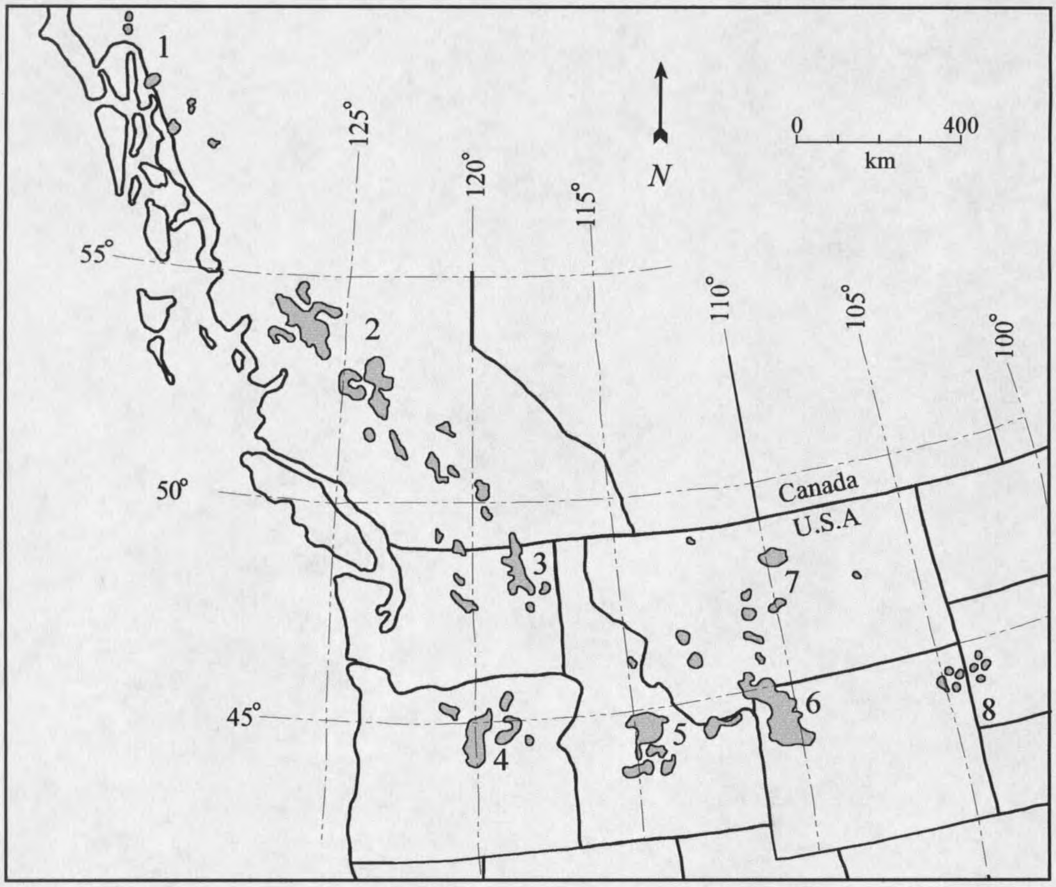

Figure 1. The northwestern United States and Canadian Cordillera showing the location of early- to middle-Eocene volcanic fields (adapted from Chadwick, 1985; Armstrong, 1988; Dudas, 1991; Norman and Mertzman, 1991; Luedke, 1994; and Morris et al., 2000). Numbers refer to: 1. Sloko volcanic province, 2. Francois Lake igneous complex, 3. Colville igneous complex, 4. Clarno volcanics, 5. Challis volcanic province, 6. Absaroka volcanic province, 7. Montana alkalic province, 8. Black Hills-Bear Lodge Mountains igneous centers.

are thought to represent subvolcanic intrusive bodies related to extrusive rocks at Sepulcher Mountain (Iddings, 1891; Smedes and Prostka, 1972), but no genetic relationship has been established, and thus they have never been formally included in the Absaroka Volcanic Supergroup (Smedes and Prostka, 1972).

Significance of Eocene Magmatism in the Northern Cordillera

Eocene igneous provinces are distributed throughout the northern Rocky Mountains forming a belt that stretches from southern Yukon to Wyoming. This belt is relatively narrow in British Columbia (~70-300 km) and is diffuse (~1400 km) in the northwestern United States between 43° and 48° north latitude (Figure 1). Collectively, these igneous provinces were originally interpreted as an early Tertiary magmatic arc (Lipman et al., 1972; Coney and Reynolds, 1977), analogous to those formed above modern subduction zones (e.g. the Cascade and Andean arcs). This "arc" is sometimes referred to as the "Challis Arc", although in this study it is termed the Eocene magmatic belt.

Two notable features of the Eocene magmatic belt are its width between 43° and 48° north latitude and the number of discrete igneous provinces located within this region (Figure 1). Three large (>15,000 km^3), roughly contemporaneous volcanic fields, the Clarno (~47-34 Ma; Vance, 1988; Urbanczyk and Lilligren, 1990), Challis (~51-40 Ma; Norman and Mertzman, 1991), and Absaroka (~55-38 Ma; Hiza, 1999; Lindsay et al., 2000; Feeley et al., *in press*) fields, are located across this region. Four smaller areas situated across this region were also strongly affected by Eocene magmatism. These include the Colville igneous complex, Montana alkalic province, and the Black Hills-

Bear Lodge Mountains igneous centers. Petrologic investigations of these igneous provinces over the last four decades have documented the chemical compositions of rocks present, allowing for general comparison.

Rocks with either calc-alkaline or alkaline-potassic geochemical affinities characterize Eocene igneous rocks across this region. Calc-alkaline rocks are volumetrically dominant and include intermediate (~54-65 wt % SiO_2), high-alumina (>15 wt % Al_2O_3), and low- to high-K (LeMaitre et al., 1989) compositions. These compositions are typical of rocks documented at the Challis (Norman and Mertzman, 1991) and Absaroka (Chadwick, 1970) volcanic fields as well as at the Colville igneous complex (Morris et al., 2000). Alkaline-potassic rocks are generally strongly silica undersaturated (Ne-normative, ≤30%), potassic ($K_2O/Na_2O \approx 1.0$-6.0), and predominately mafic, compositions typical of rocks documented across the Montana alkalic province and at the Black Hills-Bear Lodge Mountains igneous centers (Jenner, 1989).

Lipman et al. (1972) first recognized that the distribution of calc-alkaline and alkaline-potassic rocks across this region reflects generally increasing K_2O contents eastward across the region. Although rocks from a specific igneous province generally exhibit either calc-alkaline or alkaline-potassic affinities, both types also occur in close proximity at the Crazy Mountains in the Montana alkalic province (Dudás, 1991) and at the Independence volcano in the AVP (Meen and Eggler, 1987). In addition to exhibiting either calc-alkaline or alkaline-potassic affinities, widely distributed igneous rocks from across the Eocene magmatic belt display remarkable chemical similarities to each other and to rocks found at modern volcanic arcs.

Striking features shared to some extent by both calc-alkaline and alkaline rocks from the Eocene magmatic province are high abundances of large ion lithophile elements (LILE) relative to abundances of high field strength elements (HFSE). For example, extreme LILE abundances of Ba >1000 ppm, Sr >450 ppm, and Rb >60 ppm and HFSE abundances of Zr <200 ppm, Nb <20 ppm, Ta <2.0 ppm, and Ti <6000 ppm are typical of rocks from the Colville igneous complex, (Morris et al., 2000), Challis volcanic field (Norman and Mertzman, 1991), Absaroka volcanic province (Meen, 1987), and Montana alkalic province (Dudás, 1991). Enrichment in LILE relative to HFSE is considered a characteristic geochemical signature of arc-related igneous rocks (Pearce and Norry, 1979; Perfit et al., 1981). Specifically, values of Ba/Ta >450 and Ba/Nb >25 are considered diagnostic of subduction-related magmatism (Gill, 1981). In light of these parameters, a cursory interpretation of these compositions might suggest the involvement of a subduction-related component.

Petrogenetic hypotheses regarding the origin of these igneous rocks are both varied and controversial, and strikingly different tectonomagmatic models have been proposed for their origin. Recognition of the predominately calc-alkaline nature of rocks emplaced contemporaneously with subduction of the Farallon Plate beneath western North America led early workers to develop models that related these rocks to subduction. Eastward increasing potassium contents across the magmatic belt were thought to represent increasing depth to the subducting Farallon Plate and, therefore, increasing interaction of subduction-related magmas with continental crust (K-h relationship of Dickinson and Hatherton, 1967). Lipman et al. (1971) interpreted the changing compositions of rocks and distribution of igneous activity across the belt in relation to evolving subduction geometry between the North American and Farallon Plate and suggested that an "imbricate" double subduction zone was responsible for producing arc-like magmatism far inland from the Eocene trench. Further research modified this hypothesis, suggesting that changing plate convergence rates caused the dip of the subducted slab to shift from steep to shallow angles, resulting in temporally shifting loci of arc-like magmatism across a broad region (Bird, 1984; Ward, 1995). Eocene calc-alkaline and alkaline-potassic rocks from the Crazy and Highwood Mountains of the Montana alkalic province are currently interpreted to represent subduction-related magmas (O'Brien et al., 1991; du Bray and Harlan, 1996).

Other studies, although acknowledging that Eocene igneous rocks exhibit a "subduction-related geochemical signature", recognize a close spatial and temporal association between magmatism and large-scale crustal extension. This relationship is well documented at the Challis volcanic field (Norman and Mertzman, 1991) and Colville igneous complex (Morris et al., 2000) and has also been proposed for the AVP (Hiza, 1999). Petrogenetic models developed for these regions suggest that regional extension led to consequent decompression partial melting of the upper mantle and lower crust. The arc-like geochemical signature is interpreted as being inherited by Eocene magmas through interaction with, or derivation from, lithospheric mantle (Dudás, 1991) and continental crust (Morris et al., 2000) that was chemically "enriched" through pre-Eocene subduction-related magmatism. Alternatively, some researchers argue that Eocene magmatism across this region cannot be explained by simple subduction or extension related models and suggest that it may not be possible to identify a single causative melt-generation process or simple tectonomagmatic setting for Eocene magmatism in northwestern North America (Meen and Eggler, 1987; Dudás, 1991; Irving and O'Brien, 1991; MacDonald et al., 1992).

The compositional significance and origin of Eocene magmatic rocks in the AVP remain poorly understood. One of the outstanding problems in deciphering the regional significance of the AVP is that petrologic data have been obtained from only a small fraction of the magmatic rocks exposed. Most previous studies have concentrated on mineralized areas and nearly all geochemical data is based on small sets of major-element analyses from widely separated localities (Chadwick, 1970; La Pointe, 1977; Nelson et al., 1980). Thus, the relative contributions of mantle, crustal, and potentially subducted sources to parental magmas and their subsequent differentiation processes are not well known. This study presents new information on the petrogenesis of a calc-alkaline magmatic center in the AVP and contributes to studies whose ultimate goal is to better understand the origin and tectonic significance of this large-scale Eocene magmatic event.

CHAPTER 2

GEOLOGIC SETTING

Tectonic Setting

The AVP is bordered on the west by the Yellowstone Plateau, on the northwest by the Madison Range, on the northeast by the Beartooth Mountains, on the east by the Bighorn Basin, and on the south by the Wind River Basin. The volcanic province occupies the Absaroka basin, a shallow Laramide foreland basin (Sundell, 1993) that formed concurrently with surrounding basement-cored uplifts exposed in the Washakie, Gallatin-Madison, and Beartooth mountain ranges. The majority of these uplifts experienced episodic contractional deformation from late Cretaceous through middle Eocene time (Schmidt and Garihan, 1983; Winterfield and Conrad, 1983). The AVP rests unconformably on deformed Paleozoic to Mesozoic carbonate and clastic sedimentary strata and on high-grade metamorphic and igneous rocks of the Wyoming Province, an Archean granite-gneiss craton that underlies much of Wyoming, Montana, and southeastern Idaho. Seismic refraction studies indicate that the crust beneath the AVP at present is ~45-50 km thick (Prodehl and Lipman, 1989) and lithospheric thickness is estimated to be at least 170 km thick based on the presence of a weak low-velocity zone at 170-225 km depth (Iyer and Hitchcock, 1989). Although the composition of the deep crust beneath the AVP is poorly constrained, an amphibolitic to granulitic lower-crust is inferred through geochemical evidence (Meen and Eggler, 1989) and xenolith geothermobarometry (Joswiak, 1992).

Regional extension associated with crustal thinning and development of metamorphic core complexes occurred during the early-to-mid Eocene in northeastern Washington (Morris and Hooper, 1997), north-central Idaho (Wust, 1986; Janecke, 1992; Janecke and Snee, 1993), and westernmost Montana (Foster and Fanning, 1997). Although contemporaneous with magmatism in the AVP, little evidence is documented for major Eocene extensional faulting within or directly adjacent to the AVP. Both listric and normal faults have been recognized and mapped across the AVP, but they are not acknowledged as products of regional extension (Montagne and Chadwick, 1982; Sundell, 1993). It has also been suggested that the Heart Mountain detachment may be associated with regional extensional faulting (Hiza, 1999), but there is little conclusive evidence to support this relationship. The Heart Mountain detachment is a shallow-rooted, bedding-parallel, low-angle normal fault that accommodated transport of the hanging wall for a distance of 50 km or more (Hauge, 1993). It appears to represent a structure associated with large-scale, eastward-directed, gravitational sliding of a growing volcanic highland (Hauge, 1985) and not regional crustal extension.

Magmatism in the AVP occurred between 55 and 38 Ma (Hiza, 1999; Lindsay et al., 2000; Feeley et al., *in press*), apparently during a transitional period in the tectonic framework of the northern Rocky Mountains. The earliest eruptions occurred directly after, but possibly overlapping with the last phases of Sevier- and Laramide-style contractional deformation (Love et al., 1975; Sundell, 1993). Magmatism also coincided with the onset of regional crustal extension in the northern Rocky Mountains directly west of the AVP (Burchfiel et al., 1992; Janecke and Snee, 1993; Foster and Fanning, 1997). Thus, magmatism in the AVP occurred during period critical to understanding the tectonomagmatic framework of the northern Cordillera in the early Tertiary period.

Physical Volcanology of the AVP

Encompassing an area of approximately 23,000 km^2 with a maximum thickness of 1500 m, the AVP is one of the most voluminous Eocene volcanic fields in the northern Cordillera (Steven et al., 1972). The inferred depositional setting for the AVP is an approximately 90 km wide belt of large stratovolcanoes, shield volcanoes, and dike swarms flanked by coalescing alluvial aprons (Sundell, 1993). Volcaniclastic rocks are volumetrically dominant and include volcaniclastic sandstone, siltstone, claystone, conglomerate, and breccia (Smedes and Prostka, 1972). Intercalated primary volcanic rocks increase in abundance near eruptive centers and include effusive lava flows, flow breccias, and domes as well as pyroclastic flow and fall deposits. Hypabyssal intrusive bodies are common at many of the eruptive centers and include dikes, sills, ring dikes, cone sheets, plugs, stocks, and laccoliths (Parsons, 1969).

Smedes and Prostka (1972) defined the Absaroka Volcanic Supergroup to include all volcanic rocks within the AVP as well as associated outliers erupted or deposited during the Eocene. They defined three stratigraphic divisions: the Washburn, Sunlight, and Thorofare groups. Rocks exposed at Sepulcher Mountain represent the type section for the Sepulcher Formation, the western member of the Washburn Group. The aerial distribution of these groups (Figure 2) and stratigraphic divisions are, however, currently under revision (e.g. Sundell and Eaton, 1982; Hiza, 1999).

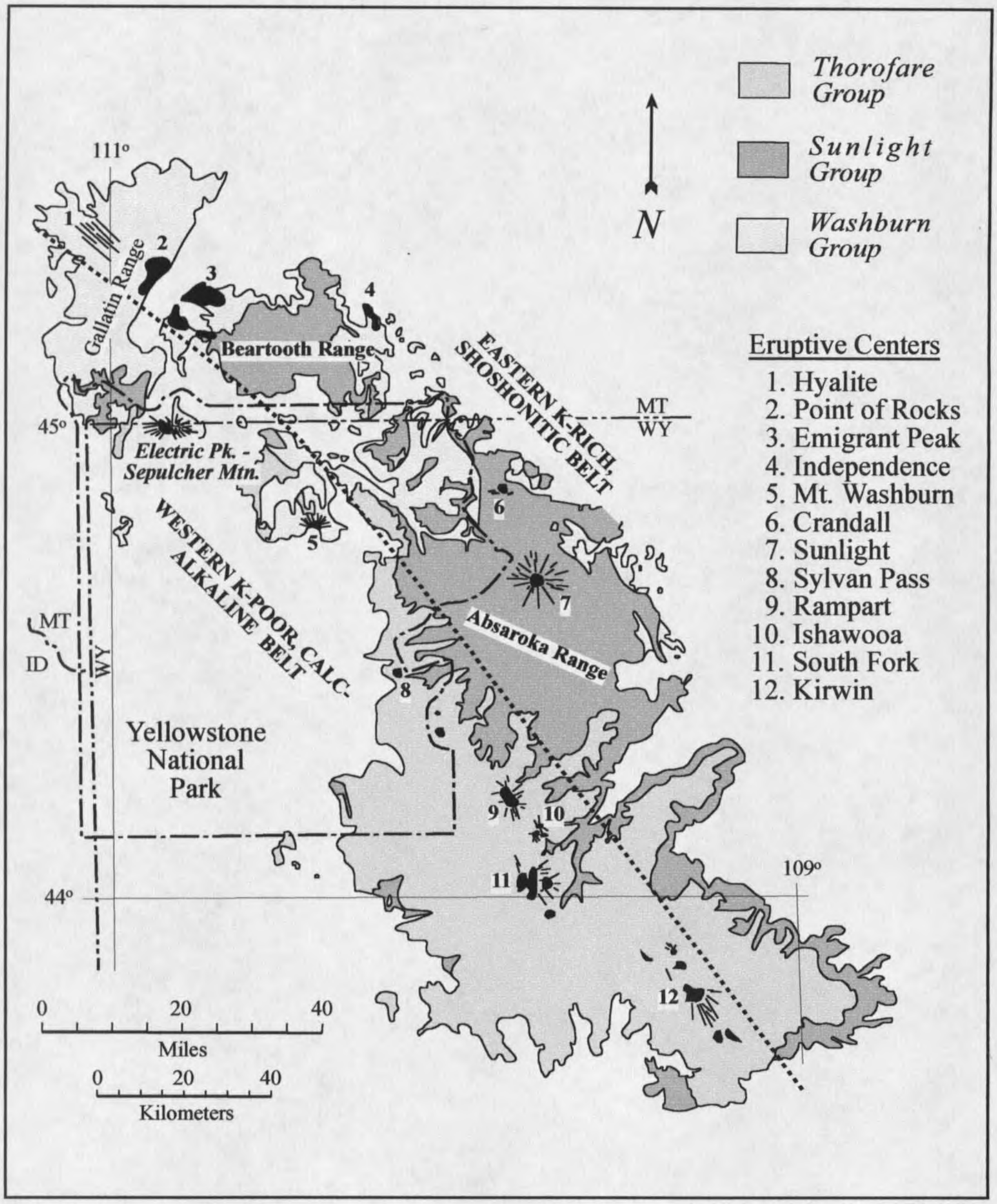

Figure 2. Generalized geologic map of the Absaroka volcanic province showing spatial extent of the major stratigraphic divisions of the Absaroka Volcanic Supergroup (modified from Smedes and Prostka, 1972; Chadwick, 1970) and location of the Electric Peak - Sepulcher Mountain eruptive center. Other eruptive centers discussed in the text are numbered for reference. Thick dashed line shows the approximate division between western potassium-poor and eastern potassium-rich belts (after Chadwick, 1970). Single dot-dashed line is the boundary of Yellowstone National Park.

Eruptive styles within the AVP were varied and are represented by Plinian airfall deposits (Sundell and Eaton, 1982), Hawaiian-style dike-fed lava flows and lava lakes (Nelson and Pierce, 1968), as well as deposits from Vesuvian-, Strombolian-, and Pelean-style eruptions (Wilson, 1964; Rubel, 1971; LaPointe, 1977). In addition, the Castle Rocks "chaos" is interpreted to be the deposit of a stratovolcano sector collapse that was one hundred times larger than that of the 1980 Mt. St. Helens eruption (Sundell, 1985). Although significantly eroded, edifice types likely included composite cones, shield volcanoes, silicic domes, small Mt. Mazama-sized calderas, and dike swarms. Paleo-relief was likely greater than 3,000 m between the highest terrain (stratovolcanoes) and adjacent lowlands (alluvial aprons) based on compositional and morphological differences in fossil fauna and flora (Fritz, 1982; Yuretich, 1984).

Across-Strike Geochemical Variations

Thirteen distinct eruptive centers are presently recognized in the AVP and are aligned along two sub-parallel belts (Figure 2). Chadwick (1970) interpreted these lineaments as Precambrian structures that were reactivated during the Laramide Orogeny. On the basis of major element compositions from ~50 rocks from nine eruptive centers, Chadwick (1970) demonstrated that the two sub-parallel belts of eruptive centers exhibit significant compositional differences with respect to potassium content and differentiated a western "K-poor" calc-alkaline belt and an eastern "K-rich" shoshonitic belt (Figure 2). These across-strike variations in potassium content are similar to those observed at many subduction-related volcanic arcs (e.g. Gill, 1981; Tatsumi and Eggins, 1995) although the petrogenetic origin of these variations in the AVP is unclear.

Southern Gallatin Range

Electric Peak and Sepulcher Mountain (EPSM), a western-belt, calc-alkaline eruptive center, is located in the northwest corner of the AVP (Figure 2). Samples for this study were collected from an area bound on the northwest by the Yellowstone River, on the east by the North Entrance Road, to the south by the North Fork of the Gardner River, and on the west by ~111°52' west longitude (Figure 3). Although the region is semi-arid, bedrock geology is only moderately exposed at lower elevations due to extensive landslide deposits in both Eocene volcanic and Cretaceous sedimentary strata. Eocene igneous rocks are well exposed through late Tertiary to Quaternary normal faulting and Pleistocene glacial erosion at higher elevations on Electric Peak and Sepulcher Mountain.

The dominant structural feature in the area is the north-to-south oriented east Gallatin-Reese Creek fault system, represented by a 600 m fault scarp (Figure 3). The Reese Creek fault separates Electric Peak from Sepulcher Mountain and exhibits greater than 1200 m of stratigraphic displacement of Paleozoic and Mesozoic sedimentary strata (Pierce et al., 1991). The uplifted southern Gallatin Range footwall block consists of gently folded Paleozoic and Mesozoic carbonate and clastic sedimentary rocks that overlie Archean biotite-bearing gneissic granitoids. The sedimentary strata dip gently (~10°-20°) to the north-northeast exposing almost the entire stratigraphic section from the Cambrian Flathead Sandstone to the Late Cretaceous Landslide Creek Formation. Laccoliths, stocks, sills, and dikes intrude the sedimentary strata in the southern Gallatin Range. Consistent with the age relationships recognized by Iddings (1889), Ruppel

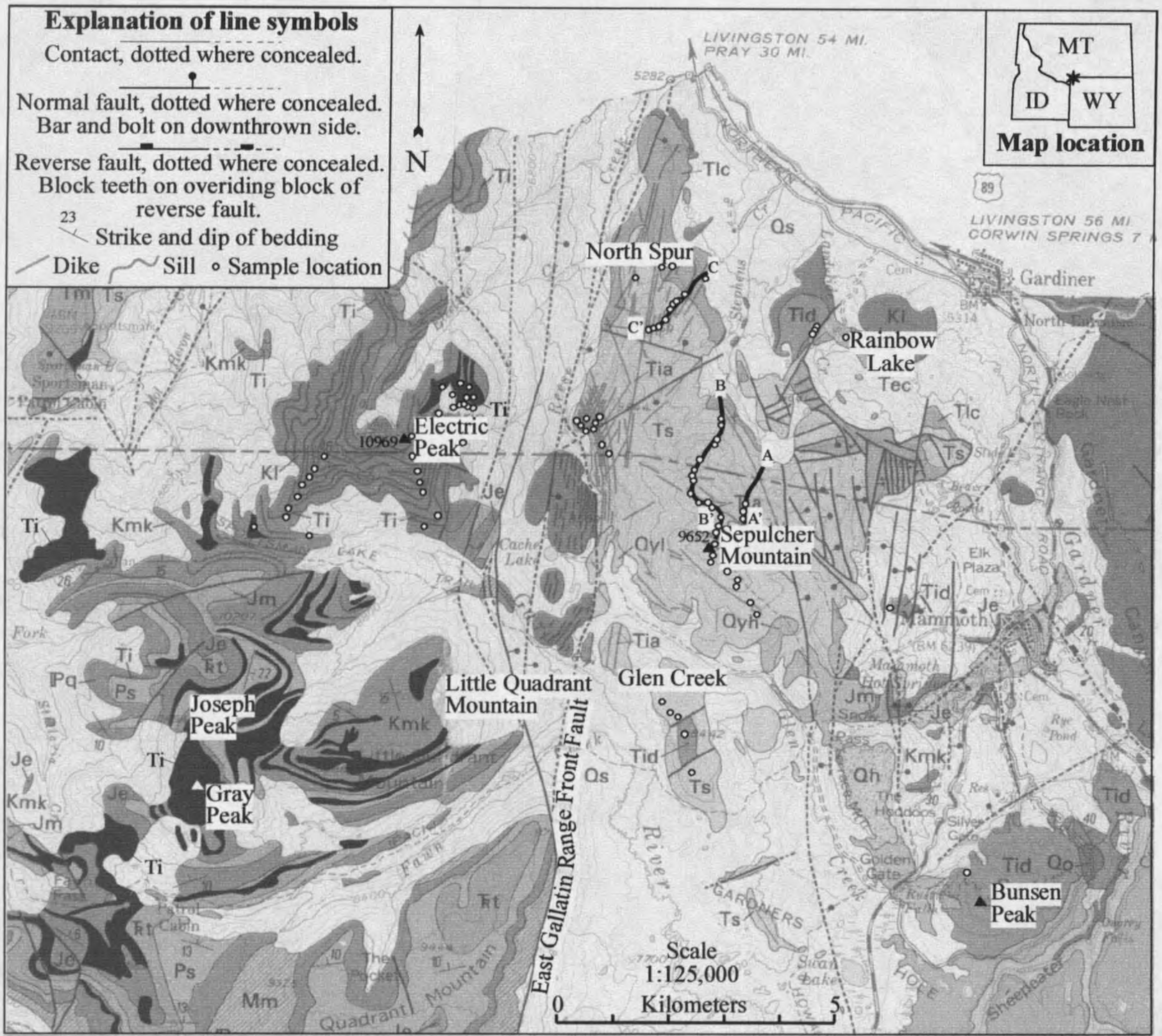

Explanation of Map Units

Quaternary

Surficial deposits

Qs	Qh

Qs, detrital deposits
Qh, hot-spring deposits

Yellowstone Volcanic Rocks

Qo	Qsl	Qyl	Qyh

Qo, Osprey Basalt
Qsl, Swan Lake Basalt
Qyl, Lava Creek Tuff of Yellowstone Group
Qyh, Huckleberry Ridge Tuff of Yellowstone Group

Tertiary

Intrusive Rocks

Ti	Tia	Tid

Intrusive rocks: plugs, laccoliths, dikes sills, and irregular bodies. Age relations not known for all rocks. Gray Peak: 50.0 Ma (Hiza, 1999); Bunsen Peak: 37.9 Ma (Lindsay et al., 2000)

Ti, rhyodacite, quartz latite, quartz monzonite, quartz diorite, quartz monzodiorite, granodiorite, and granite in the southern Gallatin Range.
Tia, andesitic dikes and sills
Tid, dacite

Absaroka Volcanic Supergroup

Tm	Ts	Tlc	Tec

Tm, Mount Wallace Formation of Sunlight Group; dominantly andesitic and basaltic lava flows, lesser volcanic sediments.
Ts, Sepulcher Formation of Washburn Group; dominantly light-colored andesitic rocks.
Tlc, Lost Creek Tuff Member of Ts; light-colored rhyodacite block and ash-flow tuff, 53.4 Ma (Hiza, 1999).
Tec, Elk Creek Basalt Member of Ts.

Cretaceous

Kl	Kmk

Kl, Landslide Creek Fm., Everts Fm., Eagle Sandstone, Telegraph Crk. Fm., Cody Shale, and Frontier Sandstone.
Kmk, Mowry Shale, Thermopolis Shale, and Kootenai Fm.

Jurassic

Jm	Je

Jm, Morrison Formation
Je, Ellis Group

Triassic

Trt	Thaynes, Woodside and Dinwoody Fm.

Permian

Ps	Shedhorn Sandstone

Carboniferous

Pq	Mm

Pq, Quadrant Sandstone and Amsden Fm.
Mm, Madison Group

Figure 3. Geologic map of a portion of northwestern Yellowstone National Park (U.S.G.S., 1972). The locations of generalized stratgraphic sections for the volcanic sequence at Sepulcher Mountain are indicated with lines labeled: A-A', B-B', and C-C'.

(1972) suggests that there is a south-to-north age progression of intrusive activity in the southern Gallatin Range, with the Mt. Holmes stock in the southern end of the range being the oldest and the Electric Peak stock at the northern end being the youngest. However, both of these interpretations are based on often poorly exposed field relationships. Only the Gray Peak laccolith (Figure 3) has yielded a reliable radiometric age (50.00 ± 0.09 Ma; $^{40}Ar/^{39}Ar$ on biotite separate; Hiza, 1999).

Electric Peak Stock

Electric Peak is the highest point (3,342 m) on the 30 km long ridge that forms the southern Gallatin Range. It consists of predominately Cretaceous shallow marine clastic sedimentary rocks including the Frontier Sandstone, Cody Shale, Telegraph Creek Formation, and Eagle Sandstone. Numerous sills intrude these sedimentary rocks. The sills are typically 1-5 m thick, porphyritic, and dacitic in composition. They are characterized by phenocrysts of plagioclase feldspar, amphibole, and biotite and are pervasively altered, often appearing bleached. These sills radiate from the Gray Peak laccolith (Figure 3), located ~6 km southwest of Electric Peak (Ruppel, 1972). Ruppel (1972) estimates that the Cretaceous stratigraphic section in the northern part of the Southern Gallatin Range is doubled in thickness due to the large number of sills present. Collectively, the sills and sedimentary sequence at Electric Peak are faulted, crosscut, and weakly metamorphosed through contact with the Electric Peak stock that cores the peak.

The Electric Peak stock has an outcrop area of ~1 km^3 and is pyramidal in shape. It is exposed in the walls of two glacial cirques on the east and northeast side of Electric Peak and on the dividing arête (Figure 4). A geologic map of the Electric Peak stock is

Figure 4. Two of the three main intrusive bodies of the Electric Peak stock viewed from the south. The darker wedge shaped body in the center foreground of the photograph is ~ 90 m in height and is composed of five intrusive phases ranging in composition from quartz diorite to granite. The darker knobs on the ridge in center midground of the photograph are smaller holocrystalline outcrops projecting from the roof of an intrusion probably similar in shape to the one in the foreground. Emigrant Peak, another early Eocene eruptive center in the Absaroka Volcanic Province, is visible on the skyline in the background of the photograph.

presented in Figure 5. Although the bulk of the stock is covered with talus, six intrusive phases are recognized: five holocrystalline phases of the stock and one hypocrystalline phase represented by dikes. Collectively, the six intrusive phases represent a texturally and compositionally zoned, hypabyssal, small-volume stock.

Individual intrusive phases of the Electric Peak stock exhibit minor textural zonation. Silicic holocrystalline phases are typically fine- to medium-grained and intermediate composition holocrystalline phases are typically fine-grained. The deceptive coarse-grained appearance of holocrystalline rocks is due to the presence of abundant mafic and felsic glomerocrysts. Dikes are porphyritic, contain a hypocrystalline groundmass, and are typically fine-to medium-grained. Chilled margins are present in both hypocrystalline and holocrystalline phases with grain size decreasing within 0.10 m of intrusive contacts with country rock.

Intrusive phases of the Electric Peak stock display sharp, discordant contacts with the Cody Shale, Telegraph Creek Formation, and Eagle Sandstone. Contacts are typically narrow (<0.01 m), jagged, and discordant to sedimentary bedding. Sedimentary and metamorphic xenoliths are abundant along the margins of the intrusion. Shale and sandstone xenoliths are lithologically similar to Cretaceous sedimentary country rock (e.g. Cody Shale, Frontier Sandstone) and hornblende-plagioclase-garnet gneissic xenoliths are similar to Archean metamorphic lithologies exposed in Yankee Jim Canyon (~5 km north of the study area). Sedimentary and metamorphic xenoliths commonly exhibit sharp (<0.005 m) contacts with their intrusive host and are often surrounded by a thin (<0.01 m) concentration of leucocratic rock. Medium-to coarse-grained hornblende gabbro magmatic inclusions (0.005-0.10 m long-axis) are abundant at the base of one

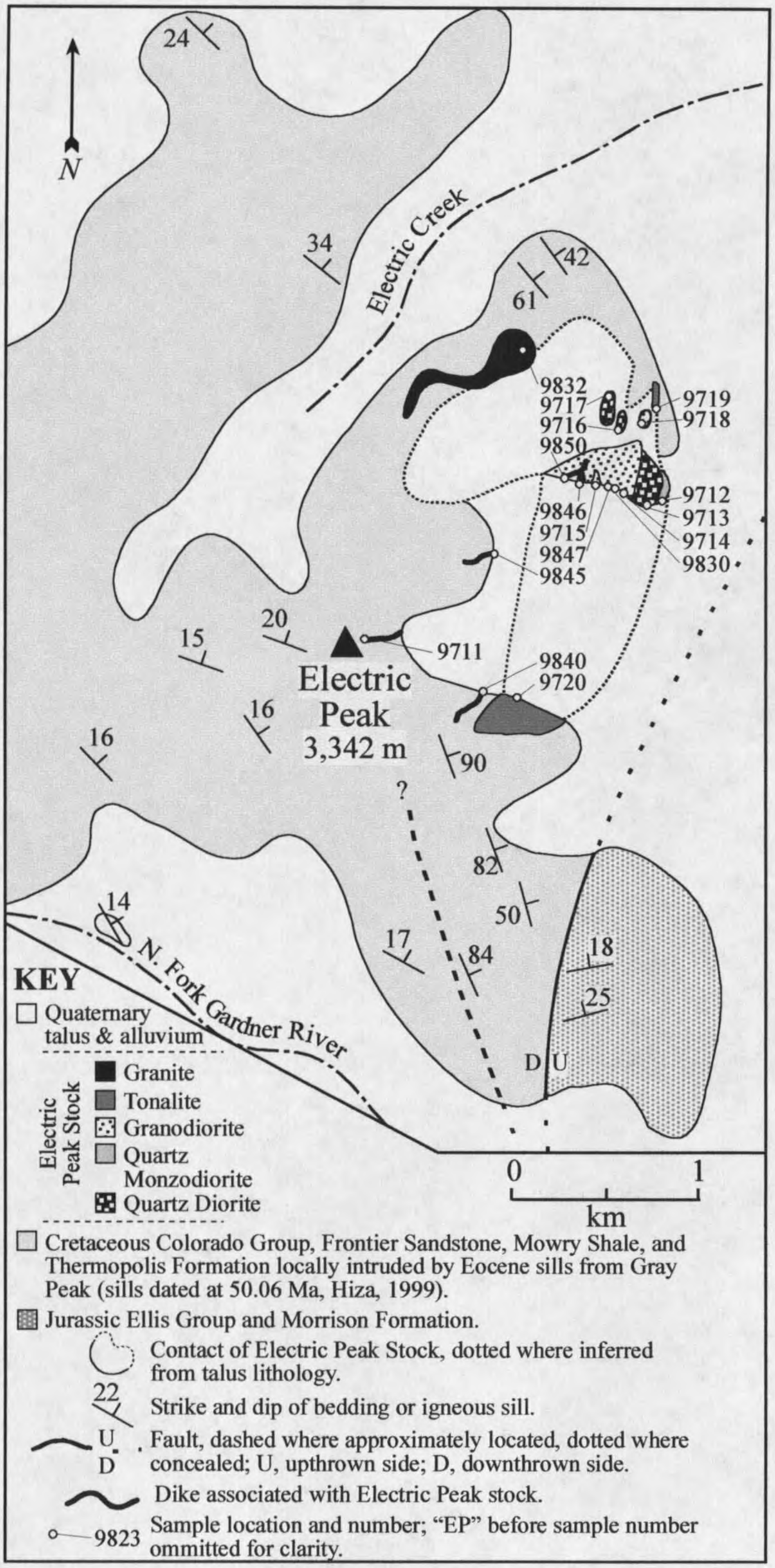

Figure 5. Geologic Map of the Electric Peak stock.

granodiorite outcrop (EP9714) and are less abundant, but present, throughout all holocrystalline phases of the Electric Peak stock.

The Electric Peak stock exhibits considerable compositional diversity. Normalized modal compositions of samples from the Electric Peak Stock are plotted in Figure 6 (Streckeisen, 1979). Rocks from discrete intrusive bodies within the stock range compositionally from biotite-amphibole quartz diorite to amphibole-bearing biotite granite. A spatial pattern in the distribution of intrusive compositions is difficult to recognize, however, silicic phases appear to be peripheral to more intermediate phases (Figure 5). Individual intrusions of the Electric Peak stock do not exhibit mineralogical phase zoning but do exhibit mineralogical ratio zoning. The mafic- to felsic-mineral ratio generally increases slightly within 5 – 10 m of intrusive contacts. Contacts between individual intrusions range from sharp to diffuse but are always less than 0.10 m in width and are typically as sharp as 0.01 m.

The relatively sharp contacts between different intrusive phases and lack of significant compositional zonation (e.g. phase zoning) within individual intrusive phases indicate a composite origin for the stock. Textural and compositional zoning within the stock as a whole are thus not interpreted to represent the *in situ* differentiation of a single intrusion. Alternatively, these features likely resulted from multiple intrusions of diverse composition magma. The spatial distribution of compositions may be entirely random, the result of different magma density on emplacement, or the result of successive tapping of a deeper, temporally evolving magmatic system.

Intrusive rocks of the Electric Peak stock cut the numerous sills present at Electric Peak. The geologic map of Ruppel (1972) shows these sills as radiating from the Gray

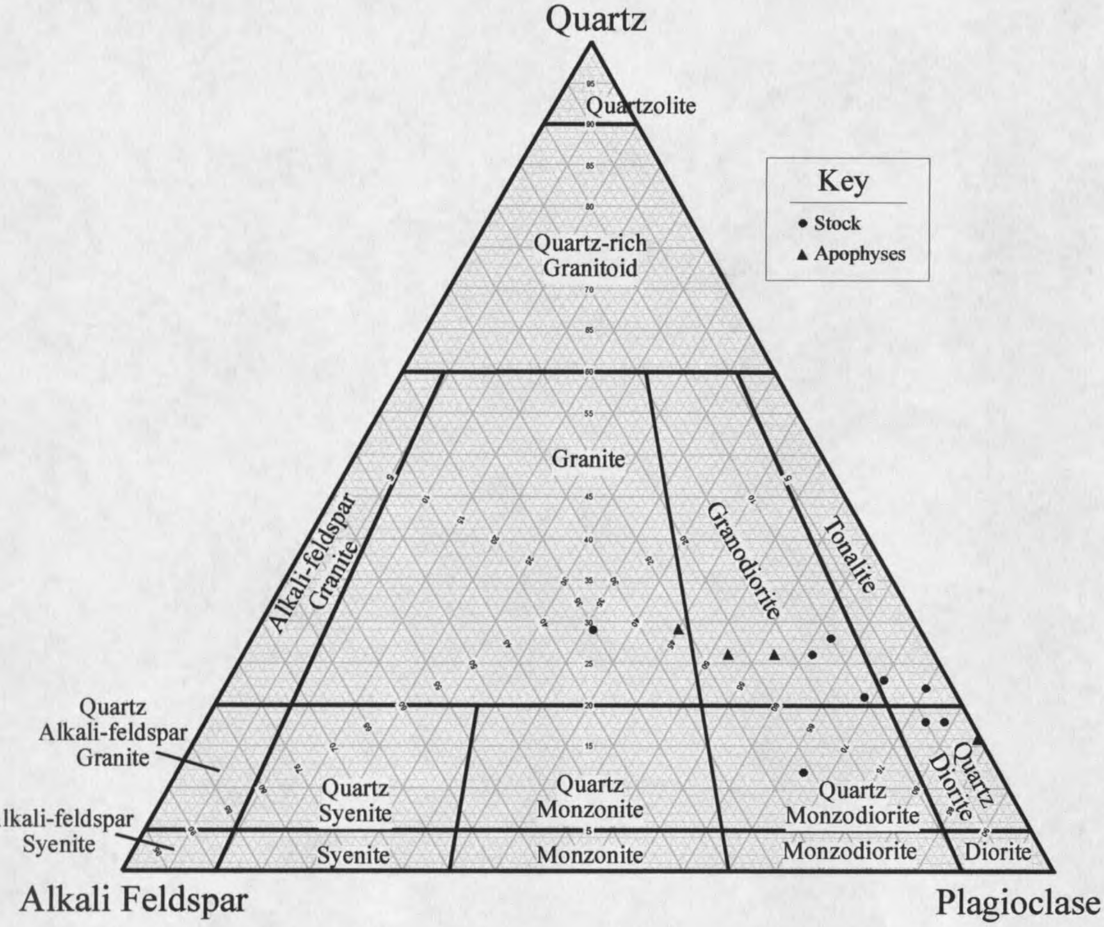

Figure 6. IUGS modal classification of holocrystalline intrusive rocks from Electric Peak (modified after Streckeisen, 1979). Circles represent samples from the Electric Peak stock, triangles represent samples from apophyses of this stock. Modal classifications of some samples (n=7) are qualitative as modal abundances of alkali feldspar were estimated in unstained thin sections.

Peak laccolith (Figure 3), which has been radiometrically dated by the $^{40}Ar/^{39}Ar$ method at 50.06 Ma (Hiza, 1999). This crosscutting relationship suggests that the Electric Peak stock is younger than 50.06 Ma. Age relationships within the Electric Peak stock are difficult to ascertain. Although crosscutting relationships are recognizable at individual outcrops, these relationships are entirely buried by talus between different outcrops of the Electric Peak Stock. Although tentative, cross-cutting age relationships recognized in the field were extrapolated to outcrops of similar composition. Intrusive activity began with emplacement of quartz diorite and was followed by intrusion of quartz monzodiorite, granodiorite, tonalite, and granite. Dikes crosscut the granite phase and are interpreted to represent the terminal stage of intrusive activity at Electric Peak.

Sub-solidus alteration is extensive at Electric Peak. Both sills emanating from the Gray Peak laccolith and dikes radiating from the Electric Peak stock exhibit pervasive sericitic alteration and secondary growth of calcite. Sills characteristically appear bleached, and plagioclase in these rocks is often completely replaced by sericite. Dikes are typically oxidized to a dark red color and exhibit secondary crystallization of calcite in vesicles, replacement of plagioclase by sericite, and replacement of both amphibole and biotite by chlorite. Holocrystalline intrusive phases are considerably less altered and extreme care was taken in the field to collect only fresh, unaltered samples.

Sepulcher Mountain and Peripheral Volcanic Vents

Volcanic rocks of the Sepulcher Formation are exposed along a structural low of the east Gallatin-Reese Creek fault system (Pierce et al., 1991; Figure 3). Primary volcanic rocks are abundant in this region and grade laterally eastwards into volcaniclastic sedimentary rocks. Although a central vent region was not identified, the high concentration of primary volcanic rocks present at Sepulcher Mountain suggests that it represents the preserved remnant of an eroded volcanic edifice (Iddings, 1891; Smedes and Prostka; 1972).

The north side of Sepulcher Mountain consists of a vertical section of intercalated volcanic products, greater than 1000 m thick (Figure 7), which grade from basal epiclastic alluvial facies into an upper sequence of vent facies lava flows and flow breccias. Lava flows are horizontal to shallow dipping and dikes are abundant. Nearly complete stratigraphic sections of primary volcanic rocks are exposed at the cliffs above Stephens Creek (section A-A'; Figure 3), along the north ridge of Sepulcher Mountain (section B-B'; Figures 3 and 7), and at the north spur of Sepulcher Mountain (section C-C'; Figure 3). Primary volcanic rocks are also present at several small eruptive centers along Glen Creek (Figure 3), at a rhyodacite dome near Rainbow Lakes (Figure 3), and at Bunsen Peak, a rhyodacite plug five kilometers southwest of Sepulcher Mountain (Figure 3). Bunsen Peak, however, is significantly younger (37.9 Ma, $^{40}Ar/^{39}Ar$ on biotite separate) than other rocks present at Sepulcher Mountain and is thus not related (Lindsay et al., 2000).

The Sepulcher block and ash-flow tuff is exposed at the base of the north spur of Sepulcher Mountain (Figure 3). This tuff was included as part of a regional stratigraphic and geochronologic study by Hiza (1999) because it was originally considered to be part of the Lost Creek Tuff, a regional ash-flow tuff. $^{40}Ar/^{39}Ar$ dating of biotite from the Sepulcher block and ash-flow tuff yielded a disturbed spectrum caused by excess Argon. The maximum estimate for the age of this unit based on the disturbed spectrum is 53.36 ±

Figure 7. The North Ridge of Sepulcher Mountain viewed from the Reese Creek drainage. Approximately 900 vertical meters of roughly horizontal, intercalated eruptive products are visibile in this photograph. The prominent buttress in the center of the photograph is capped by a two-pyroxene andesite lava flow ~15 m thick. The section below is composed mostly of epiclastic volcanic breccias and tuffs, while the section above is composed of andesitic lava flows, ash-flow tuffs, and epiclastic breccias.

0.3 Ma (Hiza, 1999). An interpretation of Hiza's maximum age estimate suggests that volcanism at Sepulcher Mountain commenced by 53 Ma.

Three generalized stratigraphic sections for the volcanic sequence at Sepulcher Mountain are presented in Figure 8. The locations of these sections are identified in Figure 3. The volcanic sequence at Stephens Creek (A-A') and the north ridge (B-B') of Sepulcher Mountain grade upward from predominately alluvial facies epiclastic breccias to vent facies lava flows and dikes. The section at the north spur (C-C') of Sepulcher Mountain notably lacks the lower epiclastic breccias and the entire exposed section is compositionally similar to the upper sections at Stephens Creek and at the north ridge. This feature likely results from stratigraphic offset along the normal fault disscused above.

The stratigraphic section at the north ridge is dominated by andesites with subordinate basaltic andesites and dacites, whereas rocks at the north spur are more silicic with dacites dominating the stratigraphic section (Figure 8). However, this compositional feature may be exaggerated due to a more restricted data set from this locality. A weakly defined compositional trend is apparent at the north ridge section where rocks exhibit increasingly silicic and potassic compositions with higher stratigraphic position. Spatial variations are more pronounced than stratigraphic variations in bulk chemistry in the Sepulcher Mountain volcanic sequence.

Texturally and compositionally, dikes and lava flows at Sepulcher Mountain are very similar to each other. They are both typically fine-to medium-grained, porphyritic, orthopyroxene + clinopyroxene andesites and biotite + amphibole dacites. Dikes are more abundant than lava flows on the east side of Sepulcher Mountain although the

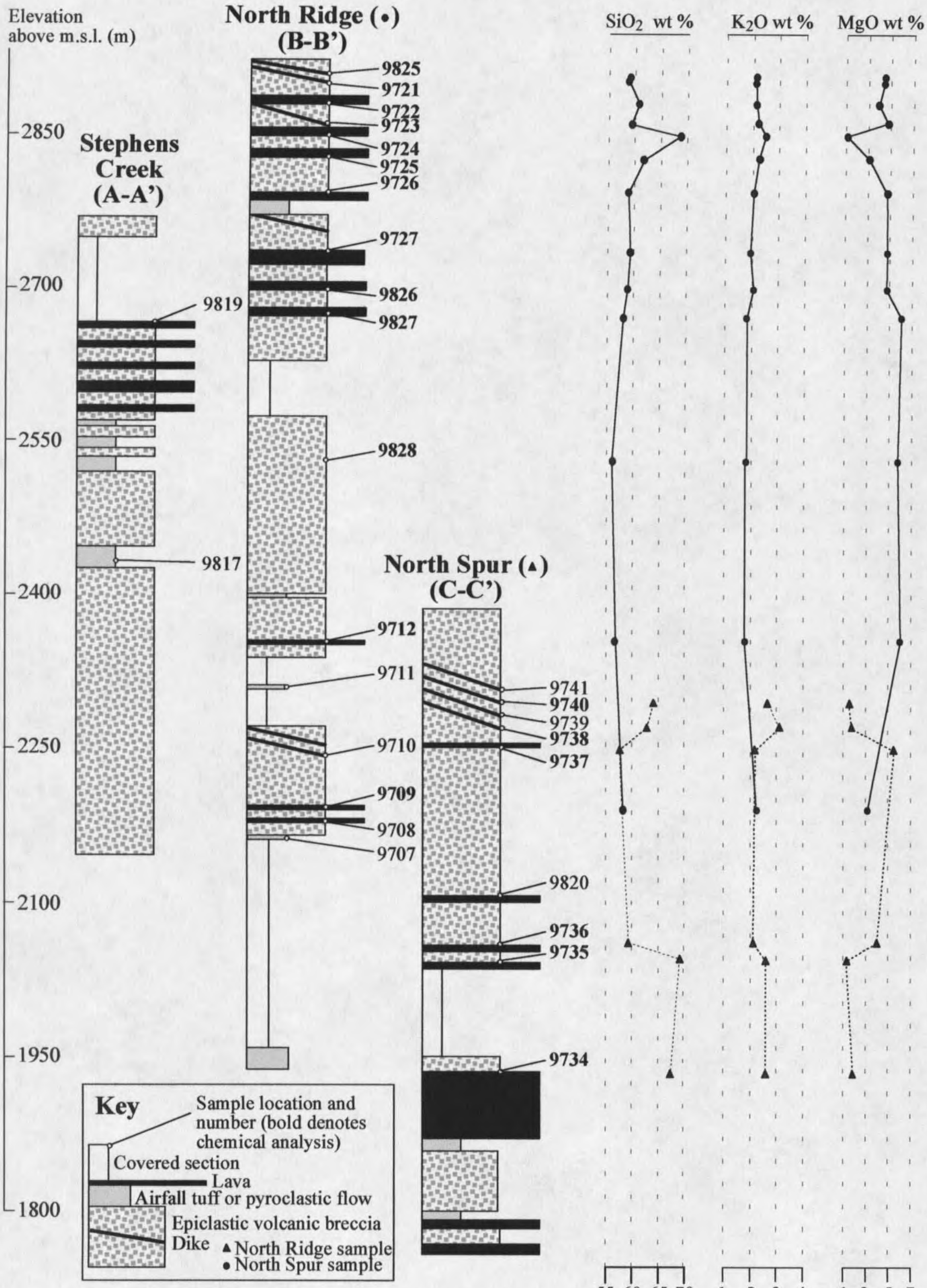

Figure 8. Generalized stratigraphic sections for volcanic sequences at Sepulcher Mountain. Major element oxide concentrations for analyzed rocks (bold labels) are plotted on the right. Circles represent data for rocks from the North Ridge, triangles represent data for rocks from the North Spur. Locations of stratigraphic sections are shown in Figure 3.

previously mapped extent of the prominent dike swarm (U.S. Geological Survey, 1972; Figure 3) was not recognized.

Geological Relationships Between Intrusive and Volcanic Rocks

Intrusive and volcanic rocks from Electric Peak and Sepulcher Mountain exist in close proximity (<5 km) to each other and exhibit broadly similar compositional ranges. The volcanic sequence at Sepulcher Mountain is separated from the Electric Peak stock by a normal fault that exhibits more than 600 m of stratigraphic offset. Together, features described above suggest that intrusive and extrusive rocks are related, and that the Electric Peak stock represents a shallow intrusion associated with the volcanic sequence preserved at Sepulcher Mountain. These interpretations are, however, not easily reconcilable with the age determinations of Hiza (1999).

Crosscutting field relationships indicate that the Electric Peak stock is younger than 50.0 Ma and the principle of superposition indicates that the volcanic Sequence at Sepulcher Mountain is younger than 53.4 Ma. Similar, intermediate-composition, moderate volume magmatism at a single eruptive center in the Andes spans approximately 1 m.y. (Signer et al., 1997). In this respect, more than 3 m.y. of magmatism at Electric Peak and Sepulcher Mountain is unlikely to be derived from a single, moderate volume magmatic system. Hiza's age determination for the Sepulcher block and ash-flow tuff is, however, an interpretation of a disturbed Ar spectrum. Moreover, it represents only a maximum age for the inception of volcanism at Sepulcher Mountain. The majority of primary volcanic rocks present at Sepulcher Mountain are stratigraphically separated from this block and ash-flow tuff by ~700 m of epiclastic breccias and covered sections (Section B-B', Figure 8). One or more unconformities representing depositional hiatuses may be present, but difficult to identify in these rocks. It is therefore likely that magmatism at Electric Peak and Sepulcher Mountain are roughly contemporaneous. Further geochronologic study would be required in order to better document the timing of this magmatism. In light of these field relationships and existing geochronologic data, intrusive rocks at Electric Peak and volcanic rocks at Sepulcher Mountain are interpreted as comagmatic, derived from similar magmatic systems. The intrusive rocks at Electric Peak are not, however, interpreted to represent subvolcanic magma chambers or crustal conduits for the volcanic rocks at Sepulcher Mountain. Instead, they simply represent small-volume, discrete magmatic injections into shallow crustal levels. Discussion of the petrography, chemistry, and petrogenesis of these rocks will further clarify the nature of this relationship.

CHAPTER 3

ANALYTICAL METHODS

Rock samples of one to two kg were collected from outcrops distributed across the entire field area. Sample locations are shown on Figure 3 and UTM coordinates are listed in Appendix A. The investigated suite consists of 41 volcanic and 17 intrusive samples. Volcanic samples were collected from 26 lava flows, nine dikes, three clasts from lava flow autobreccias, and two magmatic inclusions. Intrusive samples were collected from five different intrusive phases of the Electric Peak stock, three dikes, and two cumulate inclusions.

Major and trace element, isotopic, and modal analyses were conducted on select, fresh samples. Major element oxide compositions and concentrations of V, Cr, Ni, Zn, Rb, Sr, Y, Zr, Nb, Ba, Pb, and Th were determined by standard X-ray fluorescence (XRF) spectrometry. A minimum of 100 g of each sample (chipped at the outcrop) was shipped to Washington State University, Pullman, for sample preparation and analysis using an automated Rigaku 3370 XRF Spectrometer by the GeoAnalytical Laboratory following the protocol described by Johnson and others (1999). The oxidation state of iron was ignored during analyses and subsequently calculated and reported in this study as ferric (Fe_2O_3) based on the assumption that ferrous iron is oxidized during ignition at temperatures of ~1000° C prior to XRF analysis. Loss on ignition (LOI) was not determined.

Instrumental neutron activation analyses (INAA) were performed at the Oregon State University Triga Reactor facility following the procedure outlined by Laul (1979). Prior to irradiation at least 50 g of sample were powdered in an alumina shatterbox to avoid contamination by Co and W. Estimated precision on the INAA analyses is better than 3% (1σ S.D.) for Sc and La; 5% for Co, Cs, Hf, Ta, Th, Sm, Eu, Tb, Yb, and Lu; and 7-12% for U, Ce, and Nd. Trace element concentrations for two samples were determined through inductively coupled plasma mass spectroscopy (ICP-MS) at the GeoAnalytical Laboratory at Washington State University, Pullman. These two samples were analyzed using a Siex-Elan model 250 ICP-MS following the protocol described by Lichte et al. (1987).

Whole rock powders from select, fresh samples were shipped to the W.M. Keck Foundation National Center for Isotope Geochemistry, University of California, Los Angeles. Sr and Nd isotopic compositions of Sr and Nd were determined by thermal ionization mass spectrometry (TIMS), following the procedure described by Feeley and Davidson (1994). Prior to isotopic determinations, Sr and Nd separations were performed using the methods described by Halliday et al. (1989) and Richard et al. (1976). Precision on Sr and Nd isotopic determinations (2σ S.D.) is better than ±0.000013 and ±0.00009 respectively.

Chemical analyses of mineral phases from representative samples spanning the compositional range were performed at Oregon State University Electron Microprobe Laboratory and at the University of Lausanne, Switzerland using Cameca SX-50 electron microprobes. Both synthetic and natural phases close in composition to the unknowns were used as standards. Data were corrected for matrix interference using the ZAF method; a 15 kV accelerating voltage along with a 10 nA beam current were used for plagioclase analyses. A 20 nA current was used for analyses of all other phases.

Modal data were determined by point counting following the method described by Chayes (1956) and Hutchison (1974). Between 1200-1500 points per thin section were counted for the extrusive samples, with phenocrysts defined as ≥ 0.3 mm in the longest dimension. Approximately 1000 points were counted per thin section for the intrusive samples, with phenocrysts defined as ≥ 0.1 mm in the longest dimension. An attempt was made to identify and count only primary mineral phases if secondary alteration products including chlorite, iddingsite, and sericite were recognized. Vesicles and secondary, void-filling minerals such as silica and calcite were initially included in the modal analyses although their proportions were subsequently subtracted from the total number of counted points in order to acquire dense, unaltered rock equivalents.

CHAPTER 4

PETROGRAPHY, MINERAL COMPOSITIONS, AND MAGMATIC INTENSIVE PARAMETERS

Modal analyses of thin-sections and microprobe studies of common silicate and Fe-Ti oxide minerals were conducted for the purpose of characterizing the mineralogy of EPSM rocks, for estimating magmatic intensive parameters, and for use in quantitative petrologic modeling. Detailed petrographic descriptions of individual rocks are given in Appendix A.

Petrography

Sepulcher Mountain and Peripheral Volcanic Vents

Dikes and lava flows from Sepulcher Mountain and peripheral volcanic vents are typically hypocrystalline, fine-to medium-grained, porphyritic to glomeroporphyritic, seriate, and often sub-trachytic. Total phenocryst contents range from 8 to 43% (by volume) with the total increasing with increasing SiO_2 contents until 66 wt% SiO_2. Phenocryst contents decrease with increasing SiO_2 contents at compositions >66 wt% SiO_2.

Changes in phenocryst mode are fairly regular with respect to bulk composition (Figure 9). For example, modal proportions of olivine and clinopyroxene decrease with increasing SiO_2 and are essentially absent in rocks with >60 and >65 wt% SiO_2 respectively; whereas amphibole and biotite are essentially present only in rocks with

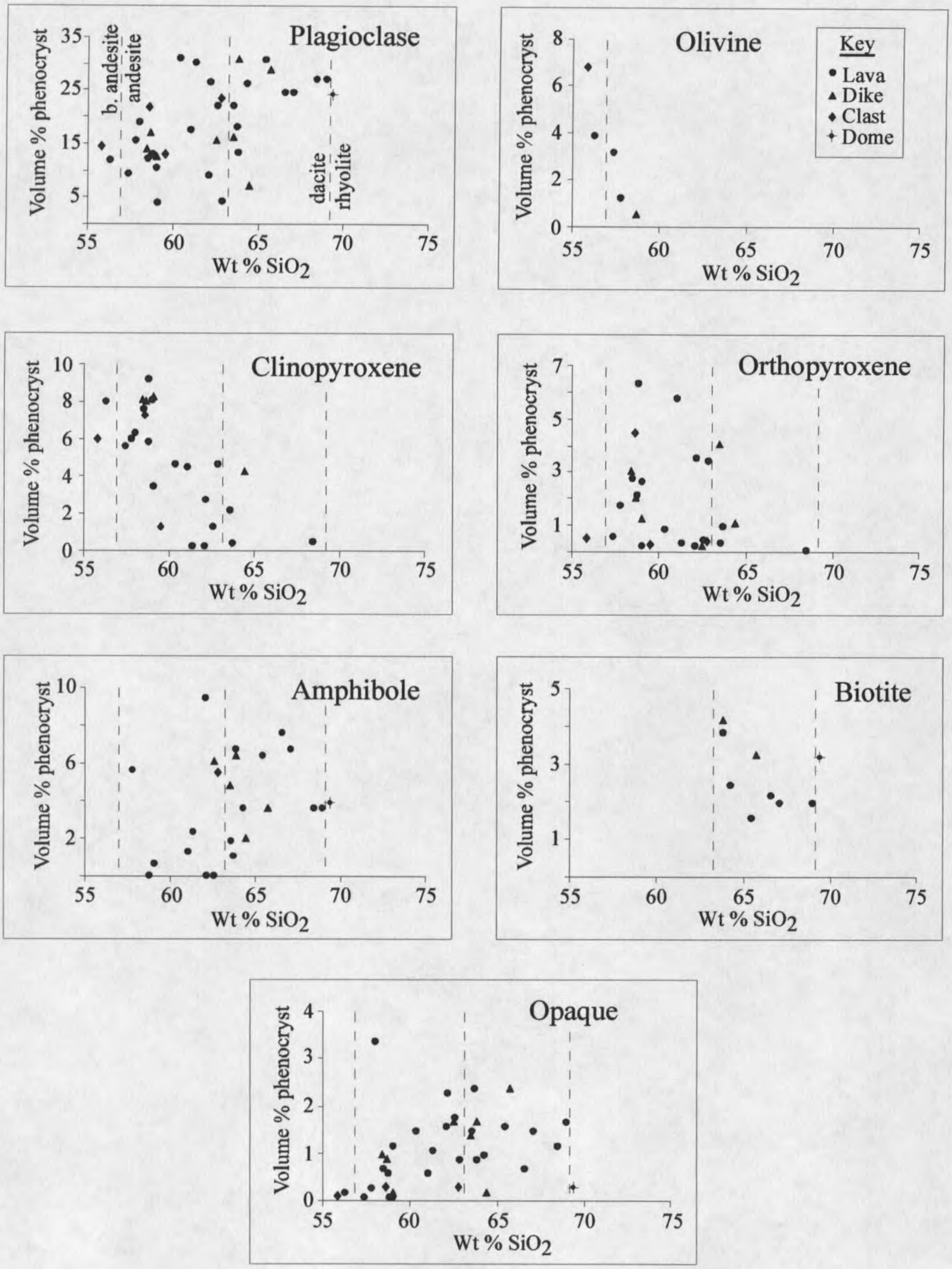

Figure 9. Variation of modal abundances of phenocryst phases in extrusive rocks from Sepulcher Mountain versus whole rock SiO_2 wt%.

>60 and >65 wt% SiO_2, respectively. Specifically, basaltic-andesitic rocks contain plagioclase > clinopyroxene > olivine > orthopyroxene; andesitic rocks contain plagioclase > clinopyroxene > orthopyroxene ± amphibole ± olivine; dacites contain plagioclase > amphibole > biotite ± clinopyroxene ± orthopyroxene; and rhyodacitic rocks contain plagioclase > amphibole > biotite > quartz.

Groundmass in rocks from dikes and lava flows at Sepulcher Mountain consists of microphenocrysts and partially-to-completely devitrified glass. Plagioclase microlites and Fe-Ti oxide microphenocrysts are present in all rocks. Modal proportions of Fe-Ti oxide phases roughly increase with increasing SiO_2 contents until about 66 wt% SiO_2. Glomerocrysts are common and typically contain solitary orothopyroxene, clinopyroxene > orthopyroxene ± Fe-Ti oxides, or clinopyroxene > orthopyroxene > plagioclase ± Fe-Ti oxides. Apatite is a common accessory mineral and is often included in plagioclase. Although rare, disequilibrium textures in amphibole, pyroxene, and plagioclase phehnocrysts are present in some rocks and were identified by the presence of magmatic reaction textures including coronae, mantling, and dissolution textures.

Magmatic inclusions (c.f. Bacon, 1986) are only recognized within the Rainbow Lakes rhyodacite dome (Figure 3). These inclusions include fine- to medium-grained, holocrystalline amphibole-trachyandesite and undercooled, fine-grained amphibole-andesite. The holocrystalline inclusions are mineralogically similar to the hornblende gabbro inclusions contained within the granodiorite phase of the Electric Peak stock.

Electric Peak Stock

Rocks from the Electric Peak stock exhibit significant textural diversity. Dikes are typically hypocrystalline, fine-to medium-grained, and porphyritic; they are texturally very similar to dikes from Sepulcher Mountain. Holocrystalline intrusive phases of the Electric Peak stock are fine- to medium-grained, seriate, and inequigranular (Figure 10). In light of these textural features, these rocks are herein referred to as micro-porphyries. Although these rocks appear medium- to coarse-grained in hand sample, petrographic inspection reveals that the exaggerated coarse-grained appearance is the result of mafic and felsic mineral glomerocrysts (i.e. numerous plagioclase laths or amphibole crystals lumped together).

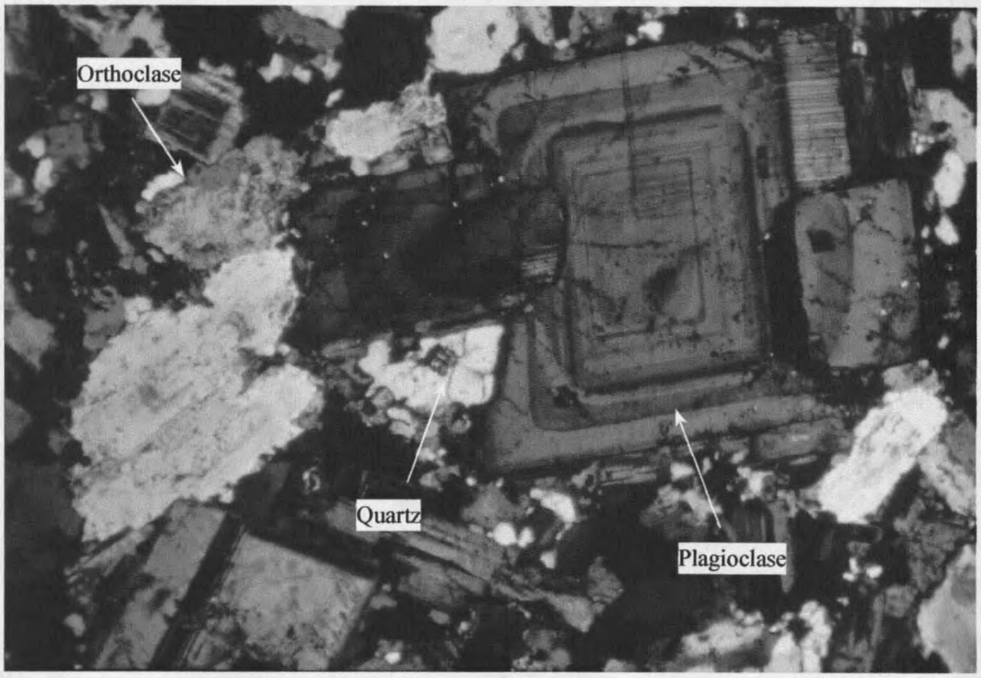

Figure 10. Medium-grained, holocrystalline, inequigranular texture representative of micro-porphyries from the Electric Peak stock (EP9718, crossed-polars, 45X magnification, field of view = 2.8 mm).

Changes in mode for dikes and micro-porphyries from Electric Peak are not as apparent with respect to bulk composition as they are for lavas and dikes from Sepulcher Mountain (Figure 11). Dioritic rocks (57-63 wt% SiO_2) contain plagioclase >> quartz > amphibole + biotite ± orthoclase. Granodioritic rocks (63-69 wt% SiO_2) contain plagioclase >> quartz > orthoclase > biotite + amphibole. Granitic rocks (69-73 wt% SiO_2) contain plagioclase >> orthoclase + quartz > biotite > amphibole. Pyroxene is only present in one sample from the quartz diorite phase of the stock. Modal proportions of plagioclase, amphibole, and biotite decrease with increasing SiO_2. Modal proportions of orthoclase and, to a lesser extent, quartz increase with increasing SiO_2. A marked inflection in modal trends is present at ~69 wt% SiO_2 for all mineral phases except quartz. Opaque minerals are present in all rocks from Electric Peak and include Fe-Ti oxides and Fe-Cu sulfides. Apatite, zircon, allanite, zoisite, and sphene are very rare accessory phases.

Inclusions are abundant in the granodiorite phase of the Electric Peak stock. These include sedimentary and metamorphic xenoliths, as well as hornblende gabbro magmatic inclusions. Sedimentary xenoliths include fragments of country rock (Cody Shale and Frontier Sandstone) that are abundant near intrusive contacts. Minor evidence for thermal or chemical interaction between xenoliths and intrusive host rock indicates incorporation at near solidus temperatures. Metamorphic xenoliths include gneissic granitoids and amphibolites, and are lithologically similar to Archean metamorphic rocks from the Beartooth Mountains. Hornblende gabbro inclusions (Figure 12) are abundant at the base of the granodiorite phase of the stock. They are holocrystalline, medium- to coarse-grained, inequigranular, and contain amphibole >> plagioclase >>> quartz + Fe-Ti

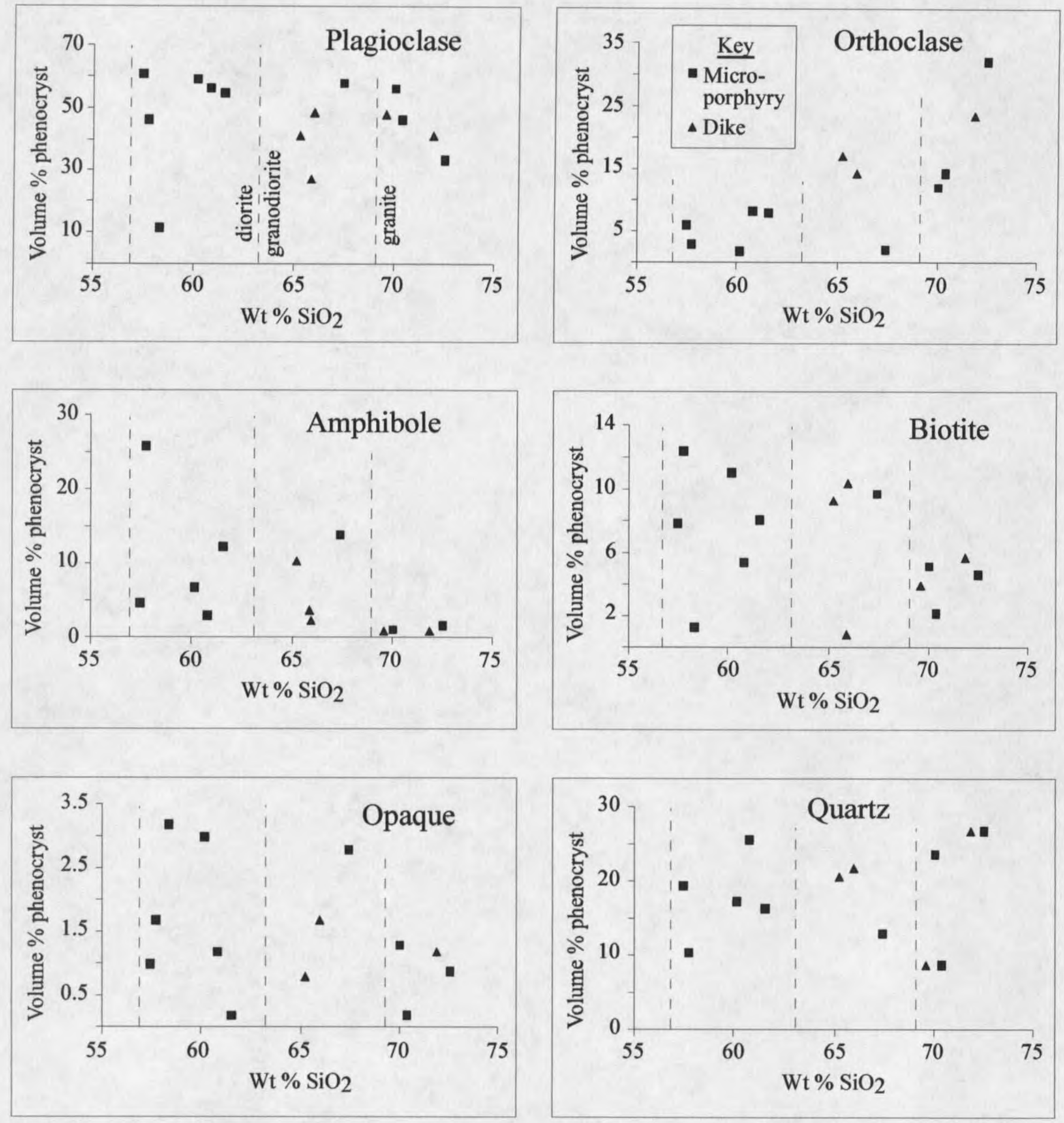

Figure 11. Variation of modal abundances of mineral phases in intrusive rocks from Electric Peak versus whole rock SiO_2.

oxides ± biotite. Amphibole in these inclusions is eustructural with medium integrity and is reacting to biotite + Fe-Ti oxides. Plagioclase is locally poikilitic around amphibole and exhibits both step and regular progressive zoning. Quartz appears to be interstitial and crystallized after amphibole and plagioclase.

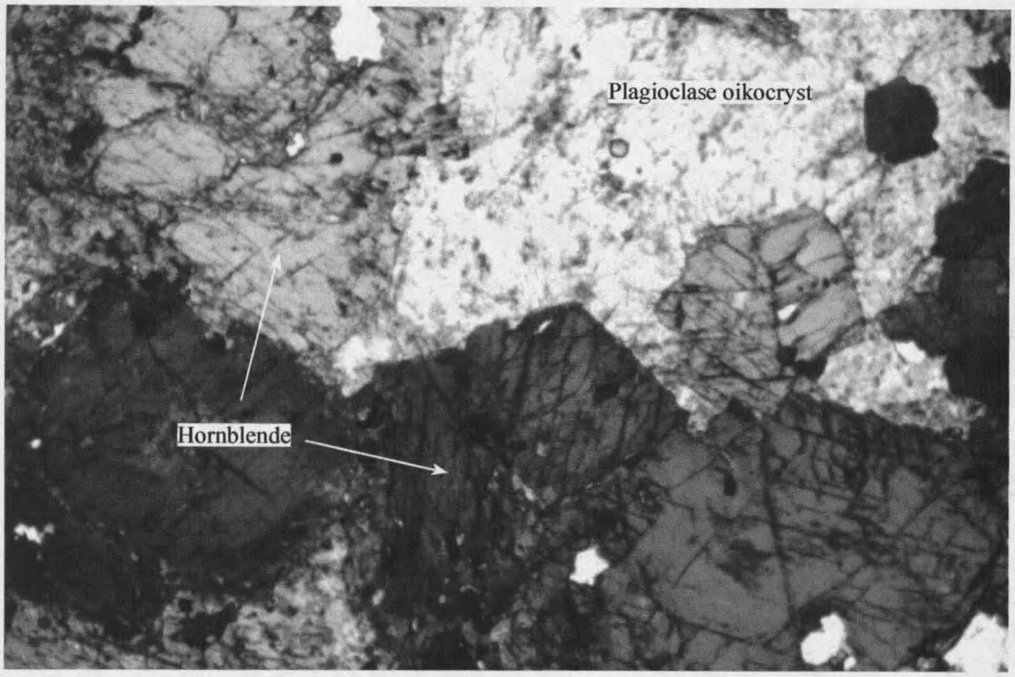

Figure 12 . Coarse-grained, holocrystalline hornblende gabbro inclusion from the base of the granodiorite phase (EP9714) of the Electric Peak stock (EP9847, plane light, 25X magnification, field of view = 2.8 mm).

Mineral Compositions

The compositions of eight mineral phases (clinopyroxene, orthopyroxene, plagioclase feldspar, orthoclase feldspar, amphibole, biotite, ilmenite, and magnetite) in eight rocks (six extrusive and two intrusive rocks) from the EPSM complex that collectively span the compositional range of the suite were determined by electron microprobe analysis. Major element compositions of mineral phases in EPSM rocks are reported in Appendices B-F. The representative chemical compositions and end-member proportions presented for these minerals in Tables 1-6 were calculated using the mean of compositional data acquired for a specific mineral phase within one rock.

Plagioclase Feldspar

Plagioclase is the most abundant mineral in rocks from the EPSM complex, with the exception of a few andesitic rocks in which clinopyroxene and amphibole are slightly more abundant. Plagioclase grains exhibit a wide range of textures. It is predominately the largest mineral phase in both extrusive and intrusive rocks, although it is occasionally subordinate to amphibole in size. Crystals are typically sub-to-euhedral, compositionaly zoned, and frequently exhibit textures caused by alternating periods of crystal growth and dissolution, perhaps induced by thermal or chemical disequilibrium (Figure 13). Plagioclase laths often exhibit mantling of resorbed crystal boundaries. Crystal cores occasionally exhibit a spongy, cellular texture. Although plagioclase is usually fresh in volcanic rocks, seriticized cores are common in intrusive samples. When present, directional fabrics such as trachytic texture, are most strongly developed among plagioclase grains.

Representative plagioclase core and rim compositions are presented in Table 1 and feldspar solid solution ternary end-member proportions are illustrated in Figure 14. Anorthite proportions range from An_{61} to An_{53} in low-silica (~58 wt%) andesitic rocks, from An_{64} to An_{27} in low-silica (~63 wt%) dacites, and from An_{49} to An_{31} in rhyodacites (~69 wt% SiO_2). Low-silica dacites exhibit the widest range of anorthite proportions, but this may reflect the larger number of analyses for this rock type. Feldspars were only analyzed in two intermediate-composition intrusive rocks and anorthite proportions in these rocks range from An_{49} to An_{12}, notably more sodic than plagioclase in extrusive samples. This may reflect lower crystallization temperatures for the intrusive rocks.

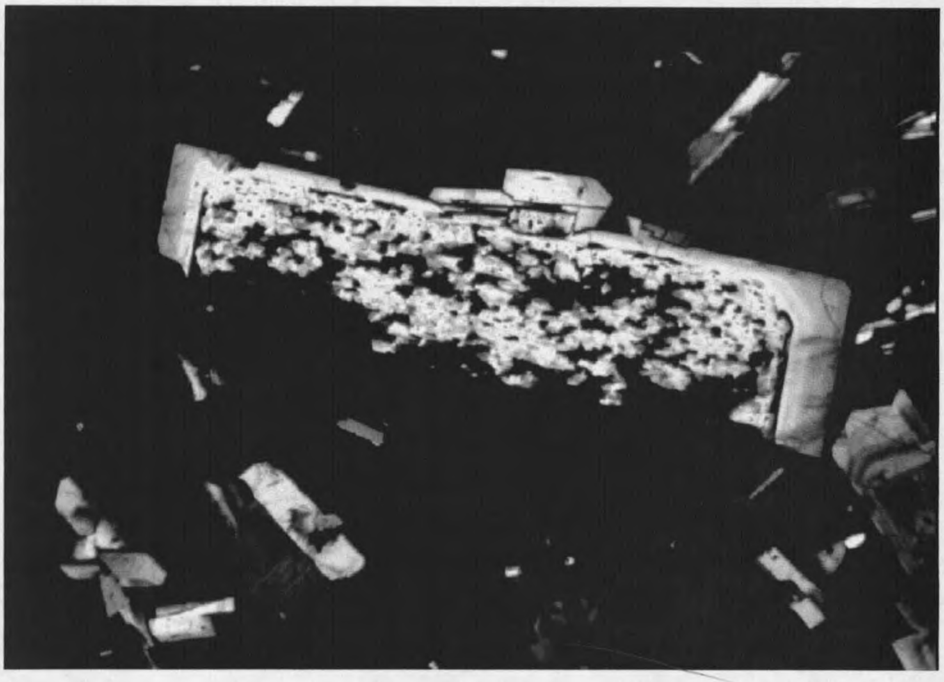

Figure 13. Plagioclase phenocryst exhibiting a euhedral rim mantling a spongy cellular core (SM9713, crossed-polars, 100X magnification, field of view = 1.05 mm).

The majority of plagioclase grains (90%) in andesitic rocks are reversely zoned (Figure 14a). However, the maximum extent of reverse zoning in plagioclase grains in andesitic rocks is 10 mol% An, and over half of the grains analyzed in these rocks exhibit reverse zoning of less than 7 mol% An. Low-silica dacites contain roughly equal proportions of normally and reversely zoned plagioclase (Figure 14b). The maximum

Table 1. Representative feldspar compositions.

Sample	(SiO_2)	Remark	n	SiO_2	Al_2O_3	FeO*	CaO	Na_2O	K_2O	An	Ab	Or	An range
SM9721	58.38	cores	7	52.28 (0.32)	28.97 (0.19)	0.63 (0.02)	11.77 (0.21)	4.59 (0.12)	0.30 (0.01)	57.6	40.64	1.75	53 to 61
SM9721	58.38	rims	6	51.75 (0.12)	29.73 (0.22)	0.72 (0.08)	12.84 (0.15)	3.95 (0.08)	0.23 (0.00)	63.37	35.27	1.35	61 to 65
SM9825	58.67	cores	5	52.85 (0.42)	29.60 (0.29)	0.62 (0.03)	12.14 (0.31)	4.26 (0.15)	0.28 (0.02)	60.16	38.19	1.65	57 to 64
SM9825	58.67	rims	3	51.88 (0.32)	30.34 (0.38)	0.71 (0.04)	12.77 (0.34)	4.03 (0.14)	0.24 (0.02)	62.76	35.84	1.4	60 to 64
SM9814	63.53	cores	14	56.69 (0.61)	27.01 (0.42)	0.27 (0.01)	8.85 (0.47)	6.10 (0.22)	0.36 (0.03)	43.56	54.33	2.11	27 to 55
SM9814	63.53	rims	18	56.84 (0.24)	26.73 (0.16)	0.32 (0.01)	8.49 (0.21)	6.22 (0.12)	0.38 (0.01)	42.04	55.72	2.24	33 to 51
SM9740	63.84	cores	11	55.37 (0.45)	27.75 (0.36)	0.21 (0.02)	9.78 (0.40)	5.56 (0.19)	0.29 (0.03)	48.45	49.84	1.71	41 to 64
SM9740	63.84	rims	10	57.08 (0.23)	26.76 (0.22)	0.22 (0.01)	8.61 (0.20)	6.13 (0.09)	0.35 (0.01)	42.8	55.13	2.07	38 to 48
SM9724	68.43	cores	9	56.97 (0.44)	27.07 (0.33)	0.32 (0.03)	8.74 (0.33)	6.21 (0.15)	0.32 (0.03)	42.93	55.19	1.87	35 to 49
SM9724	68.43	rims	6	58.27 (0.87)	25.82 (0.51)	0.29 (0.02)	7.51 (0.59)	6.76 (0.30)	0.45 (0.04)	37.04	60.32	2.64	31 to 46
SM9735	68.95	cores	11	56.33 (0.33)	26.47 (0.26)	0.32 (0.03)	8.23 (0.28)	6.49 (0.14)	0.38 (0.02)	40.29	57.49	2.22	31 to 48
SM9735	68.95	rims	9	57.48 (0.29)	25.63 (0.07)	0.25 (0.01)	7.29 (0.08)	7.03 (0.05)	0.40 (0.01)	35.59	62.09	2.32	34 to 37
EP9714	61.59	cores	3	57.31 (1.06)	27.06 (0.51)	0.23 (0.05)	8.79 (0.65)	6.22 (0.34)	0.39 (0.06)	42.86	54.88	2.26	37 to 49
EP9714	61.59	rims	3	64.33 (1.26)	22.79 (0.73)	0.16 (0.01)	3.75 (0.86)	9.0 (0.52)	0.59 (0.03)	18.08	78.53	3.33	12 to 26
EP9845	65.97	cores	4	57.67 (1.62)	26.51 (1.14)	0.23 (0.05)	8.17 (1.26)	6.58 (0.72)	0.37 (0.05)	39.02	8.03	2.15	22 to 48
EP9714	61.59	cores	5	64.69 (0.15)	18.45 (0.07)	0.10 (0.03)	0.01 (0.01)	1.05 (0.33)	15.24 (0.44)	0.05	9.47	90.48	-
EP9845	65.97	core	1	63.82	19.28	0.07	0.19	2.92	12.01	0.96	26.73	72.31	-

Note: (SiO_2) = whole rock silica content; n = number of analyses from which mean and standard deviation were calculated; An, Ab, and Or are calculated proportions of Anorthite, Albite, and Orthoclase respectively; An range = range of anorthite proportions observed in all anayses from which representative compositions were calculated; values in parentheses represent one standard deviation of the mean. All Fe as FeO*.

extent of normal zoning in plagioclase grains in low-silica dacitic rocks is 29 mol% An, and over half of these grains exhibit normal zoning of less than 7 mol% An. Alternately, the maximum extent of reverse zoning of plagioclase in low-silica dacitic rocks is 15 mol% An, and over half of these grains exhibit reverse zoning of less than 5 mol% An. Plagioclase grains in rhyodacitic samples are almost entirely (93%) normally zoned (Figure 14c). The maximum extent of normal zoning in plagioclase grains in rhyodacitic rocks is 15 mol% An, and over half of these grains exhibit normal zoning of less than 7 mol% An.

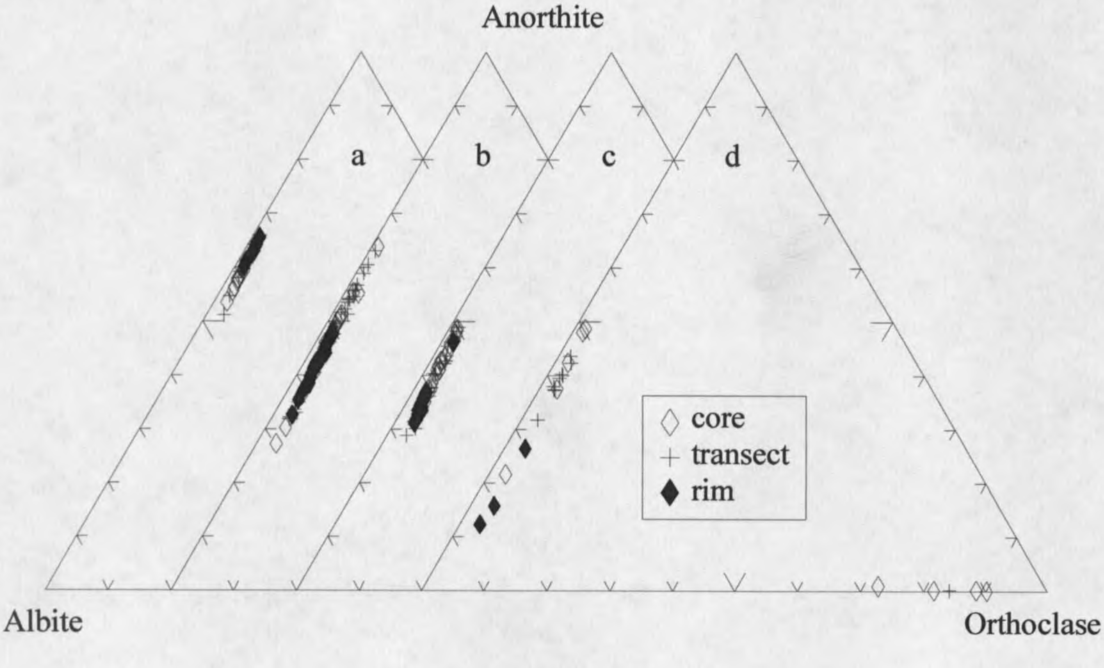

Figure 14. Ternary projections of feldspar compositions of extrusive rocks from Sepulcher Mountain and intrusive rocks from Electric Peak grouped by whole rock compositional series. Compositional series: (a) low-silica (58%) andesites, (b) low-silica (63%) dacites, (c) rhyodacites (69%), and (d) intermediate (65% SiO_2) intrusive rocks. Each point represents a single analysis.

Orthoclase Feldspar

Orthoclase is only present in holocrystalline rocks from Electric Peak. It is commonly fine-grained, uniquely associated with quartz, and interstitial to other mineral phases. Petrographically, orthoclase grains do not exhibit evidence for unmixing into Na- and K-rich phases. Due to its fine-grained, interstitial character orthoclase feldspar is extremely difficult to identify in unstained thin sections from these rocks. Therefore, modal abundances plotted in Figure 11 for unstained sections (7 of 15) are semi-qualitative.

Representative orthoclase compositions are presented in Table 1 and feldspar solid solution ternary end-member proportions are illustrated in Figure 14d. Orthoclase grains contain limited Na and almost no Ca. Orthoclase end-member proportions range from Or_{92} – Or_{72} in granodioritic rocks and Ba end-member Celsian components are less than 1 mol%.

Olivine

Olivine is present only in five lavas and dikes from Sepulcher Mountain and is restricted to those with <59 wt% SiO_2. As olivine is almost always completely altered to iddingsite and serpentine, no attempt was made to characterize olivine compositions optically or chemically.

Clinopyroxene

Clinopyroxene is the most dominant mafic mineral phase in basaltic-andesitic and andesitic lavas and dikes from Sepulcher Mountain. It is only present in one rock (a dike) from Electric Peak. Clinopyroxene occurs in volcanic rocks as isolated, euhedral to subhedral phenocrysts, and is often contained in glomerocrysts where it is typically associated with orthopyroxene. It is also present as a microphenocryst and groundmass phase.

Representative compositions of clinopyroxene are given in Table 2 and ternary end-member proportions are illustrated in Figure 15. Clinopyroxene in andesitic rocks ranges in composition from $Wo_{42}En_{44}Fs_{08}$ to $Wo_{43}En_{49}Fs_{14}$ (Table 2). Following the nomenclature of Morimoto et al. (1988), clinopyroxene compositions are predominately classified as augite, although a few rocks contain crystals with endiopside cores. Most clinopyroxene cores exhibit normal compositional zoning with rims becoming more Fe-rich than cores (Figure 15). Cores commonly exhibit more compositional variability than rims, which are dominantly $Wo_{43}En_{47}Fs_{10}$.

Orthopyroxene

Orthopyroxene is present in andesitic and a few low-silica dacitic lavas and dikes from Sepulcher Mountain and is also present in one quartz diorite dike from Electric Peak. It is almost always associated with clinopyroxene, although it is less abundant. Orthopyroxene is present both in glomerocrysts with clinopyroxene and opaque minerals and as solitary phenocrysts. It is almost always euhedral.

Table 2. Representative clinopyroxene compositions.

Sample	Remarks	(SiO_2)	n	SiO_2	TiO_2	Al_2O_3	Fe_2O_3*	FeO*	MnO	MgO	CaO	Wo*	En*	Fs*
SM9721	Cores	58.38	11	51.74 (0.18)	0.52 (0.39)	2.56 (0.23)	2.74 (0.10)	6.37 (0.42)	0.25 (0.01)	15.93 (0.26)	20.30 (0.17)	40~43	41~48	10~18
SM9721	Rims	58.38	3	52.00 (0.39)	0.50 (0.04)	2.11 (0.28)	2.83 (0.37)	6.36 (0.41)	0.26 (0.04)	16.13 (0.12)	20.48 (0.21)	40~41	44~45	14~15
SM9825	Cores	58.67	9	52.33 (0.26)	0.30 (0.05)	2.08 (0.16)	2.94 (0.23)	4.13 (0.37)	0.17 (0.01)	17.13 (0.29)	20.64 (0.14)	40~43	44~50	5~9
SM9825	Rims	58.67	1	51.14	0.51	2.08	3.46	5.52	0.22	15.72	20.55	-	-	-

Note: (SiO_2) = whole rock silica content; n = number of analyses from which mean and standard deviation were calculated; Fe_2O_3*, FeO* = Fe^{+3} and Fe^{+2} determined by charge balance; values in parentheses represent one standard deviation of the mean; Wo*, En*, Fs* are the range of observed ternary endmember proportions observed in all analyzed grains.

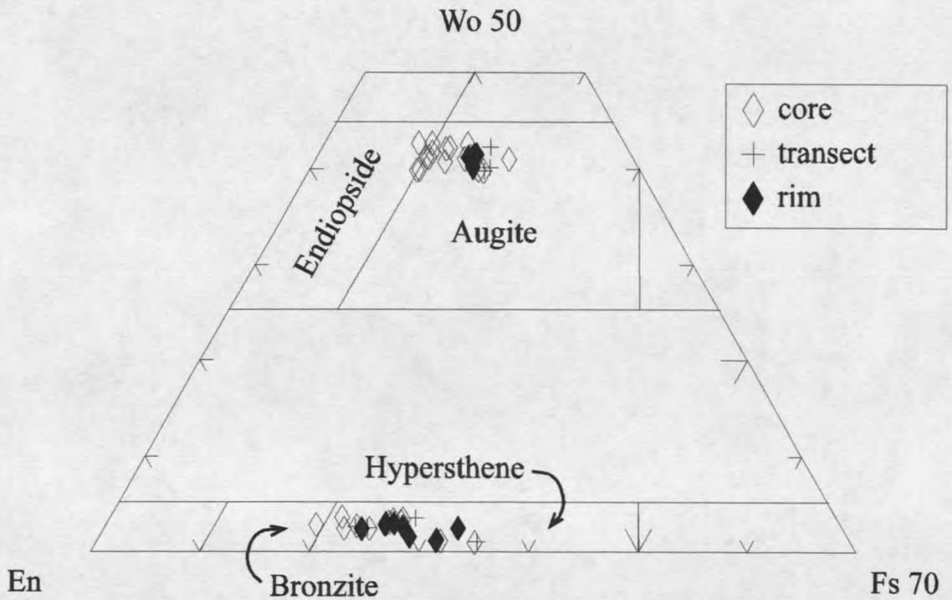

Figure 15. Ternary projection and classification of pyroxenes in extrusive rocks from Sepulcher Mountain (after Morimoto, et al., 1988). Each point represents one analysis.

Representative orthopyroxene compositions are presented in Table 3 and end-member proportions are illustrated in Figure 15. Compositions in andesitic rocks range from $Wo_{01}En_{68}Fs_{20}$ to $Wo_{03}En_{77}Fs_{31}$. Orthopyroxene are classified as hypersthene following the nomenclature of Morimoto and others (1988). Although core compositions are diverse, rim compositions are less variable and are predominately $Wo_{03}En_{72}Fs_{25}$.

Amphibole

Apart from plagioclase, amphibole is the most salient mineral phase in rocks from the EPSM complex. It is present in all lavas and dikes with >58 wt% SiO_2 and in all but two intrusive rocks from Electric Peak. Amphibole exhibits distinctive textures in both volcanic and intrusive rocks. In extrusive rocks it occurs as small (< 1.0 mm) euhedral crystals, often with oxidized rims, although it also occurs as larger (0.5 - 1.75 mm) predominately eustructural crystals with medium structural integrity. In these grains both the margins and the interior of these crystals exhibit a boxy cellular texture bounded by crystal faces. Amphibole in intrusive rocks typically has partially reacted to biotite and opaque minerals (Figure 16).

Amphibole phenocrysts in rocks from both the Electric Peak stock and Sepulcher Mountain lavas and dikes are calcic according to the nomenclature of the International Mineralogical Association Subcommittee (I.M.A.S.) on Amphiboles (Leake, 1978) because B-group cation occupancy (Ca + Na) is ≥ 1.34 and Na is ≤ 0.67. Representative compositions are given in Table 4. Compositions were calculated on the basis of the 24-oxygen hydrous formula with H_2O calculated by difference and assuming that $Fe^{3+}/(Fe^{2+} + Fe^{3+})$ is fixed and = 0.27, a reasonable estimate for hornblende in calc-alkaline

Table 3. Representative orthopyroxene compositions.

Sample	Remarks	(SiO_2)	n	SiO_2	TiO_2	Al_2O_3	Fe_2O_3*	FeO*	MnO	MgO	CaO	Wo*	En*	Fs*
SM9721	Cores	58.38	16	54.30 (0.24)	0.25 (0.03)	1.13 (0.19)	2.28 (0.27)	14.90 (0.68)	0.39 (0.02)	26.81 (0.41)	1.62 (0.08)	2~3	69~76	22~28
SM9721	Rim	58.38	1	54.48	0.23	0.83	1.68	15.64	0.4	26.54	1.56	-	-	-
SM9814	Cores	63.53	3	52.81 (0.27)	0.14 (0.05)	1.58 (0.28)	2.22 (0.31)	19.14 (0.40)	0.74 (0.02)	23.92 (0.42)	0.51 (0.26)	1	64~68	31~35
SM9814	Rims	63.53	4	53.52 (0.53)	0.13 (0.01)	1.00 (0.22)	1.25 (0.46)	18.14 (0.39)	0.70 (0.02)	24.75 (0.49)	0.81 (0.16)	1~3	65~70	28~32
SM9825	Cores	58.67	8	53.32 (0.26)	0.18 (0.01)	1.92 (0.22)	3.14 (0.39)	12.38 (0.58)	0.30 (0.02)	27.56 (0.39)	1.52 (0.08)	2~4	71~78	19~26
SM9825	Rims	58.67	4	52.96 (0.43)	0.22 (0.02)	1.76 (0.23)	3.25 (0.56)	13.58 (0.78)	0.35 (0.01)	26.72 (0.41)	1.39 (0.06)	2~3	70~74	24~27

Note: (SiO_2) = whole rock silica content; n = number of analyses from which mean and standard deviation were calculated; Fe_2O_3*, FeO* = Fe^{+3} and Fe^{+2} determined by charge balance; values in parentheses represent one standard deviation of the mean; Wo*, En*, Fs* refers to the range of observed ternary endmember proportions observed in all analyzed samples.

Table 4. Representative amphibole compositions from selected samples.

	SM9814	SM9740	SM9724	SM9735	EP9714
(SiO_2)	63.53	63.84	68.43	68.95	61.59
n	13	9	11	8	5
SiO_2	44.98 (0.51)	44.54 (0.38)	45.14 (0.39)	44.50 (0.76)	50.58 (0.35)
Al_2O_3	10.46 (0.43)	10.54 (0.51)	10.52 (0.19)	10.47 (0.74)	5.36 (0.26)
FeO	8.95 (0.18)	9.07 (0.31)	8.44 (0.35)	9.54 (0.39)	8.15 (0.09)
Fe_2O_3	3.68 (0.07)	3.73 (0.13)	3.47 (0.14)	3.92 (0.16)	3.35 (0.04)
MgO	14.70 (0.27)	14.55 (0.22)	15.09 (0.39)	14.21 (0.51)	16.62 (0.15)
CaO	10.86 (0.07)	10.93 (0.05)	10.89 (0.04)	10.85 (0.11)	11.09 (0.03)
Na2O	1.87 (0.07)	1.95 (0.08)	2.00 (0.02)	1.99 (0.09)	1.28 (0.05)
K2O	0.55 (0.03)	0.72 (0.04)	0.58 (0.07)	0.60 (0.05)	0.30 (0.02)
TiO2	1.69 (0.13)	1.84 (0.12)	1.73 (0.16)	1.90 (0.06)	0.87 (0.06)
Cr_2O_3	0.04 (0.01)	0.02 (0.01)	0.08 (0.04)	0.02 (0.01)	0.03 (0.02)
MnO	0.21 (0.02)	0.19 (0.02)	0.15 (0.12)	0.18 (0.02)	0.36 (0.02)
H_2O*	1.82 (0.05)	1.74 (0.05)	1.71 (0.07)	1.64 (0.05)	1.92 (0.08)
Name	edenitic hornblende	edenitic hornblende	edenitic hornblende	edenitic hornblende	actinolitic hornblende

Note: (SiO_2) = whole rock silica content; n = number of analyses from which mean and standard deviation were calculated; Fe^{2+} and Fe^{3+} were calculated on the assumption that $Fe^{3+}/(Fe^{2+} + Fe^{3+}) = 0.27$; H_2O* = water calculated by difference; values in parentheses represent one standard deviation of the mean.

intrusions (Dodge et al., 1968; Hammarstrom, 1982 and 1984). An attempt was made to screen out compositions representing late-stage alteration rather than primary magmatic crystallization in the intrusive rocks by imposing Leake's (1971) proposed limit of Si $\leq$ 7.5 for "igneous" amphiboles and by limiting the data set to analyses with Ca $\geq$ 1.6. Furthermore, compositions of amphibole rims exhibiting petrographic evidence for sub-solidus alteration were omitted. The range of amphibole compositions exhibited by the suite is illustrated in Figure 17, which is a plot of total Al (Al^T) versus tetrahedral Al (Al^{iv}). All compositions fall within Leake's (1971) proposed limits for Al^{vi} in igneous amphiboles. Figure 17 also illustrates the most pronounced compositional difference between amphiboles in the intrusive rocks and the extrusive rocks. Amphiboles contained within extrusive rocks consistently contain more total aluminum than those in intrusive rocks.

Amphibole classification is illustrated in Figure 18. Amphiboles range in composition from ferroan pargasite to actinolitic hornblende following the nomenclature recommended by the I.M.A.S. (Leake, 1978). Representative amphiboles from Electric Peak are predominately actinolitic-hornblende, while amphiboles from Sepulcher Mountain are predominately edenitic hornblende. In order to simplify this nomenclature, all amphiboles are considered "hornblendes" (Hawthorne, 1981) subsuming the appropriate names shown in Figure 18.

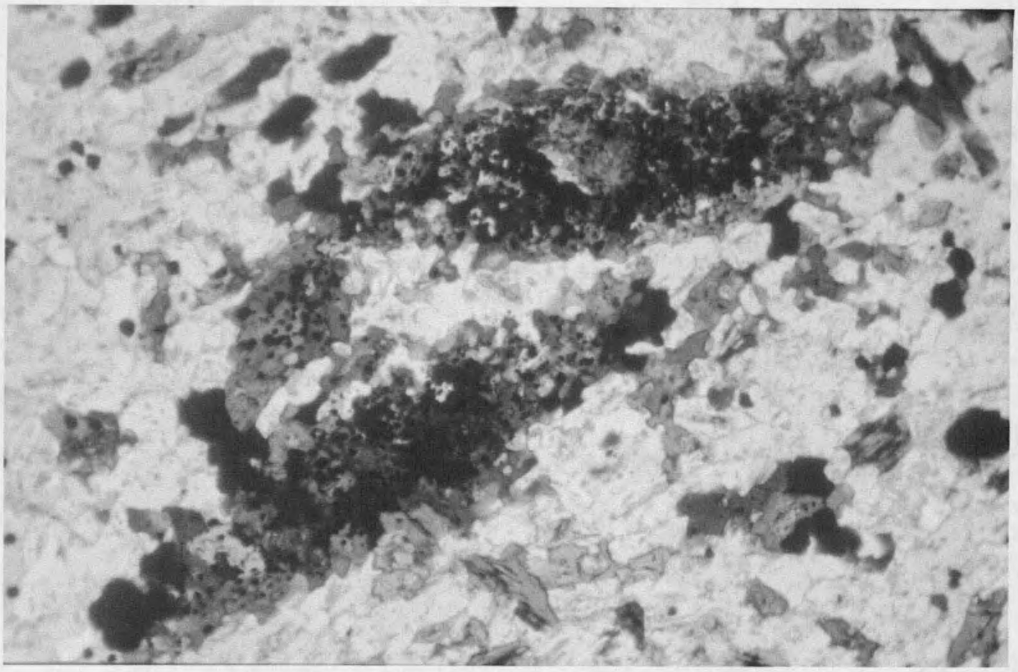

Figure 16. Eustructural amphibole with low structural integrity in a micro-porhyry from the Electric Peak stock. Amphibole has almost completely converted to biotite and Fe-Ti oxides (EP9715, plane light, 45X magnification, field of view = 2.8 mm).

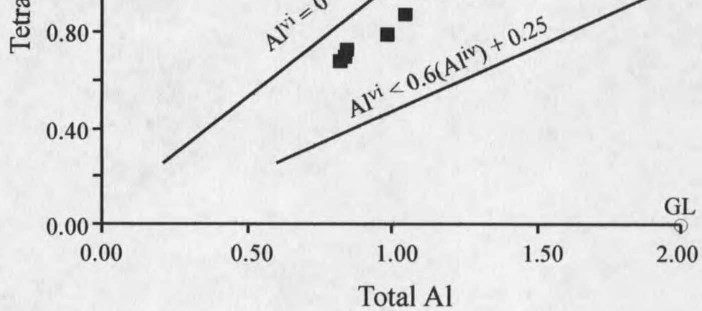

Figure 17. Plot of total Aluminum vs tetrahedral Aluminum in hornblende. Compositions from Electric Peak stock are shown as squares, compositions from Sepulcher Mountain lavas are shown as circles. The solid lines indicate the limiting condition for $Al^{vi} = 0$ and Leake's (1971) proposed limit for maximum possible Al^{vi} in calcic amphibole. Ideal endmember compositions are shown for edenite (ED), glaucophane (GL), and hastingite (HA). All analyses were recalculated using a 24-oxygen hydrous formula unit; $Fe^{+3}/(Fe^{+2}+Fe^{+3}) = 0.27$, except for ED and GL where total Fe=FeO.

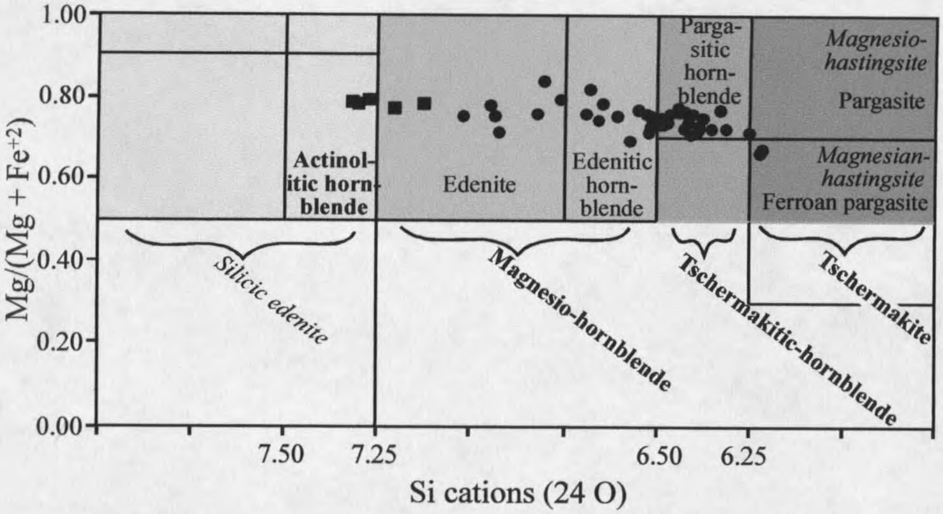

Figure 18. Classification of calcic-amphiboles (modified from Leake, 1978). Compositions from Electric Peak stock are shown as squares, compositions from Sepulcher Mountain lavas are shown as cirlces. Field names in diagonal orientation refer to shaded fields. Field names in bold type refer to nomenclature for A site (Na + K) < 0.50, Ti <0.50, those in plain type refer to nomenclature for A site (Na + K) > 0.50, Ti < 0.50, $Fe^{+3} < Al^{vi}$, whereas those in italic type refer to nomenclature for A site (Na + K) > 0.50, Ti < 0.50, Fe^{+3} > total Al.

Biotite

Biotite is exclusively found in dacitic and rhyolitic lavas and dikes from Sepulcher Mountain. It is present in all intrusive rocks from Electric Peak. Texturally, biotite occurs as anhedral shreds to euhedral sheets. In intrusive rocks biotite is often uniquely associated with opaque minerals in crystal clots and it often replaces amphibole. Biotite occasionally contains metamict zircon in silicic intrusive rocks.

Fe-Ti Oxides

Oxide minerals are present as microphenocrysts in all rocks from the EPSM complex. Analyses of opaque minerals in extrusive rocks with the electron microprobe suggest that the majority of these opaque minerals are magnetite and ilmenite. Hand sample inspection of intrusive rocks also identified pyrite and chalcopyrite. Opaque minerals occur both as disseminated grains and as crystals in glomerocrysts and amphibole-biotite-oxide clots.

Representative compositions of magnetite and ilmenite are given in Table 5 and Table 6 respectively. Magnetite in extrusive rocks is relatively homogenous with end-member proportions in the magnetite-ulvospinel solid solution series for all samples ranging from $Mt_{52}Ulv_{48}$ to $Mt_{57}Ulv_{43}$ (Table 5). Ilmenite compositions exhibit more compositional variability than magnetite with end-member proportions in the ilmenite-hematite solid solution series ranging from $Ilm_{54}Hm_{46}$ to $Ilm_{74}Hm_{26}$ for all analyses (Table 6). Ternary end-member proportions of Fe-Ti oxides are illustrated in Figure 19.

Quartz

Quartz is present only in two silicic volcanic rocks but is much more abundant in intrusive rocks. Textural varieties in extrusive rocks include quartz phenocrysts that are embayed or which exhibit non-taxial mantling by plagioclase microlites. Quartz crystals in extrusive rocks are predominately anhedral and interstitial to plagioclase, suggesting later crystallization. In a few instances, larger quartz grains exhibit poikilitic domains enclosing plagioclase and opaque minerals. Embayments into and non-taxial mantling of

Table 5. Representative magnetite compositions.

Sample	SiO_2	n	TiO_2	Fe_2O_3	FeO	MnO	MgO	Al_2O_3	V_2O_3	ZnO	Mt range	Mt	Ulv
SM9721	58.38	1	6.11 (-)	52.44 (-)	33.72 (-)	0.5 (-)	1.11 (-)	1.77 (-)	0.36 (-)	0.22 (-)	(-)	54	46
SM9814	63.53	9	6.27 (0.08)	52.90 (0.70)	33.97 (0.25)	0.34 (0.01)	1.63 (0.17)	2.21 (0.02)	0.29 (0.01)	0.11 (0.01)	52 to 55	54	46
SM9740	63.84	4	5.21 (0.10)	56.63 (0.12)	33.00 (0.08)	0.8 (0.02)	1.34 (0.02)	1.94 (0.02)	0.16 (0.01)	0.21 (0.02)	55 to 56	56	44
SM9724	68.43	12	6.19 (0.05)	51.23 (0.21)	34.35 (0.11)	0.44 (0.01)	0.75 (0.02)	1.67 (0.03)	0.31 (0.01)	0.16 (0.01)	53 to 54	53	47
SM9735	68.95	15	4.18 (0.24)	56.78 (0.25)	32.98 (0.17)	0.39 (0.03)	0.78 (0.05)	1.05 (0.05)	0.25 (0.01)	0.19 (0.01)	56 to 57	56	44

Note: (SiO_2) = whole rock silica content; n = number of analyses from which mean and standard deviation were calculated; ferric and ferrous iron calculated by charge balance; endmembers are normalized to 100%; Mt range = range of magnetite proportions observed in all analyses from which representative compositions were calculated; values in parentheses represent one standard deviation of the mean; (-) = not applicable.

Table 6. Representative ilmenite compositions.

Sample	(SiO_2)	n	TiO_2	Fe_2O_3	FeO	MnO	MgO	Ilm Range	% Ilm	% Hem
SM9721	58.38	3	32.17 (0.56)	37.30 (0.66)	25.89 (0.40)	0.82 (0.03)	0.82 (0.03)	60 to 62	61	39
SM9814	63.53	5	29.85 (0.43)	42.75 (0.65)	23.51 (0.29)	0.20 (0.02)	1.78 (0.08)	54 to 58	56	44
SM9740	63.84	4	32.28 (0.97)	39.29 (1.81)	25.70 (0.64)	0.56 (0.07)	1.54 (0.13)	56 to 64	60	40
SM9724	68.43	8	34.83 (0.45)	31.01 (0.97)	28.42 (0.97)	0.76 (0.08)	1.28 (0.09)	64 to 71	67	33
SM9735	68.95	16	36.10 (0.68)	32.03 (1.27)	28.33 (0.49)	0.79 (0.04)	1.86 (0.06)	56 to 74	67	33

Note: (SiO_2) = whole rock silica content; n = number of analyses from which mean and standard deviation were calculated; ferric and ferrous iron calculated by charge balance; endmembers are normalized to 100%; Ilm range = range of ilmenite proportions observed in all analyses from which representative compositions were calculated; values in parentheses represent one standard deviation of the mean.

quartz are also common in intrusive rocks from Electric Peak. In both extrusive and intrusive rocks quartz encloses opaque minerals.

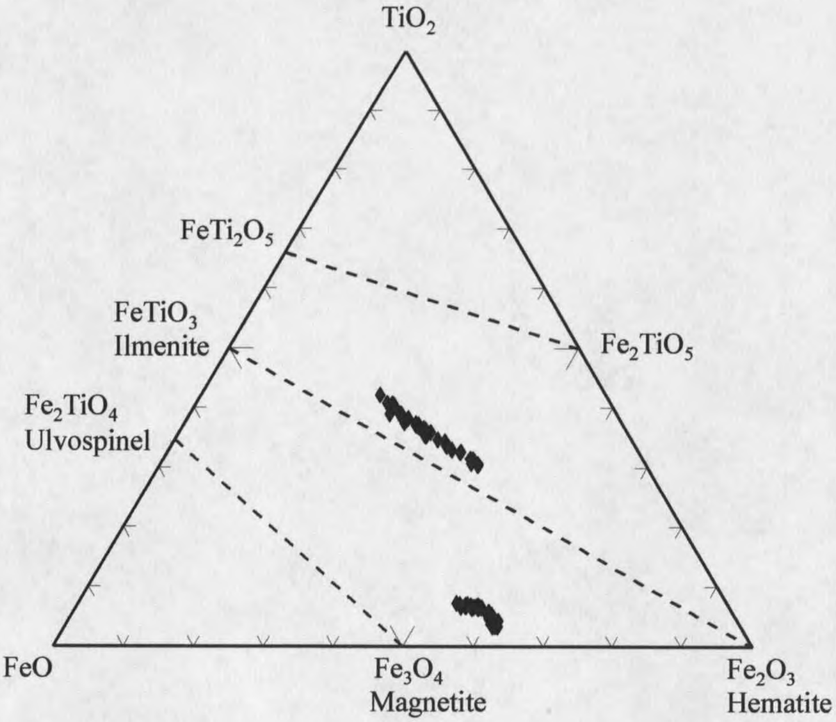

Figure 19. Ternary projection of Fe-Ti oxide compositions from representative extrusive rocks from Sepulcher Mountain. Solid solution series between end-member compositions are plotted with dashed lines.

Crystallization Sequences

Mineral inclusion patterns and the occurrence of minerals in the glomerocrysts, together with textural features and compositions of the phenocrysts described above indicate the following crystallization sequences. Basaltic-andesitic magmas crystallized olivine followed by Fe-Ti oxides, clinopyroxene + plagioclase, and orthopyroxene. Andesitic magmas crystallized plagioclase followed by clinopyroxene + orthopyroxene ±

amphibole, and Fe-Ti oxides. Dacitic magmas precipitated plagioclase followed by amphibole, Fe-Ti oxides, and then biotite. Rhyodacitic magmas share the same crystallization sequence with dacites although quartz was the last phase to precipitate. The crystallization sequence inferred from holocrystalline intermediate to silicic rocks and magmatic inclusions from Electric Peak is plagioclase, followed by Fe-Ti oxides, amphibole ± biotite, orthoclase, and finally quartz.

Disequilibria Textural Features

Petrographic evidence for chemical or thermal disequilibrium between phenocrysts and liquid is conspicuous but limited. Some low-silica (63-66 wt%) dacitic dikes and lava flows contain high modal proportions of clinopyroxene, orthopyroxene, and amphibole relative to other rocks with similar SiO_2 contents (e.g. SM904, SM9713, SM9810, SM9814). Amphibole grains in these rocks are typically anhedral and exhibit heavily oxidized rims (Figure 20). Additionally, larger plagioclase grains in these samples commonly exhibit spongy cellular cores and some contain thin, sieved margins (Figure 21). Sub- to euhedral, non-cellular rims occasionally mantle plagioclase grains that exhibit these textures. Clinopyroxene in SM9713 exhibit spongy cellular cores and are also mantled by sub-to-euhedral, non-cellular rims. Dacitic dike SM9814 contains fine-grained, holocrystalline inclusions of dacitic material (plagioclase and amphibole phenocrysts) within a vitric, andesitic-composition groundmass (plagioclase, orthopyroxene and amphibole phenocrysts). A thin layer of brown glass rims the contacts of dacitic inclusions in this sample (Figure 22), and some inclusions

Figure 20. Rounded anhedral amphibole phenocryst exhibiting a heavily oxidized rim and thin corona composed of plagioclase, clinopyroxene, and Fe-Ti oxides (SM9713, plane light, 45X magnification, field of view = 2.8 mm).

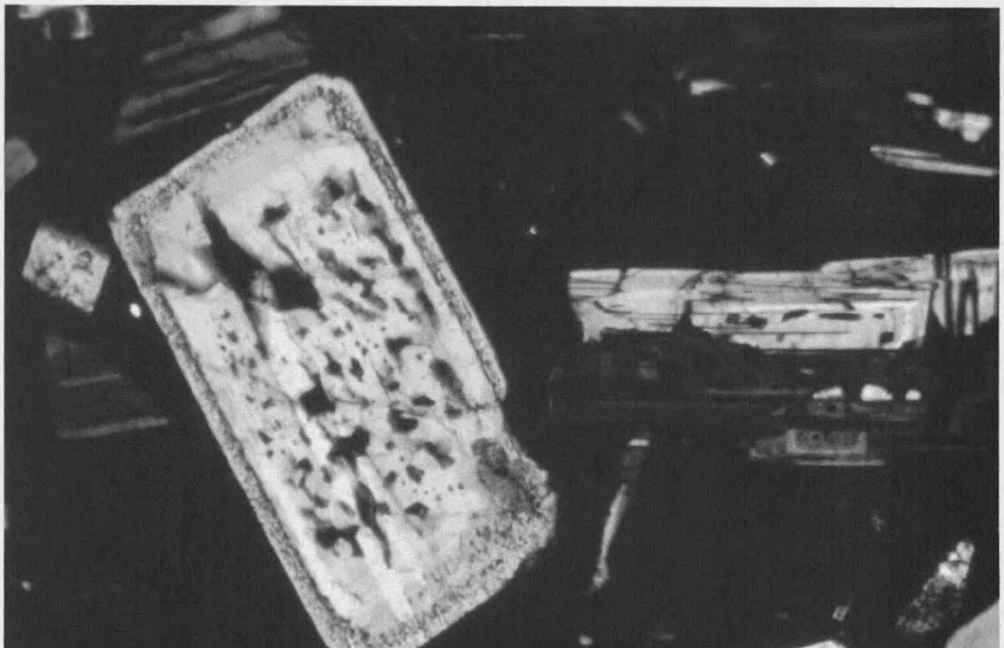

Figure 21. Euhedral plagioclase phenocryst exhibiting a thin, sieved margin and spongy cellular core (SM9713, crossed-polars, 100X magnification, field of view = 1.05 mm).

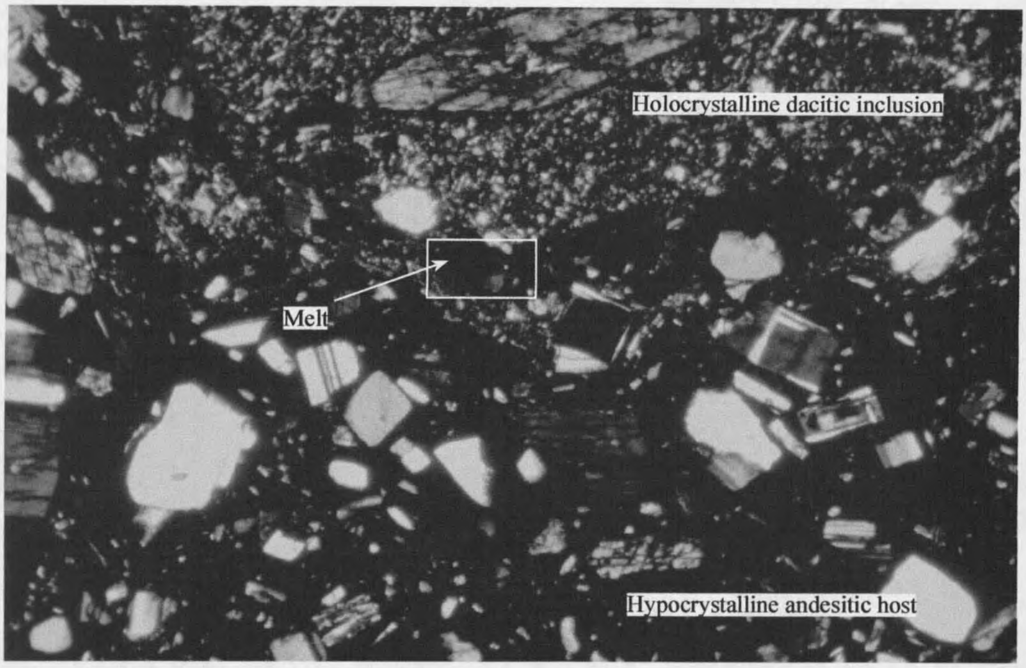

Figure 22. Holocrystalline dacitic inclusion within a fine-grained, hypocrystalline andesitic dike. Note the thin layer of brown glass that exists at the contact between the two (SM9814, crossed-polars, 45X magnification, field of view = 2.8 mm).

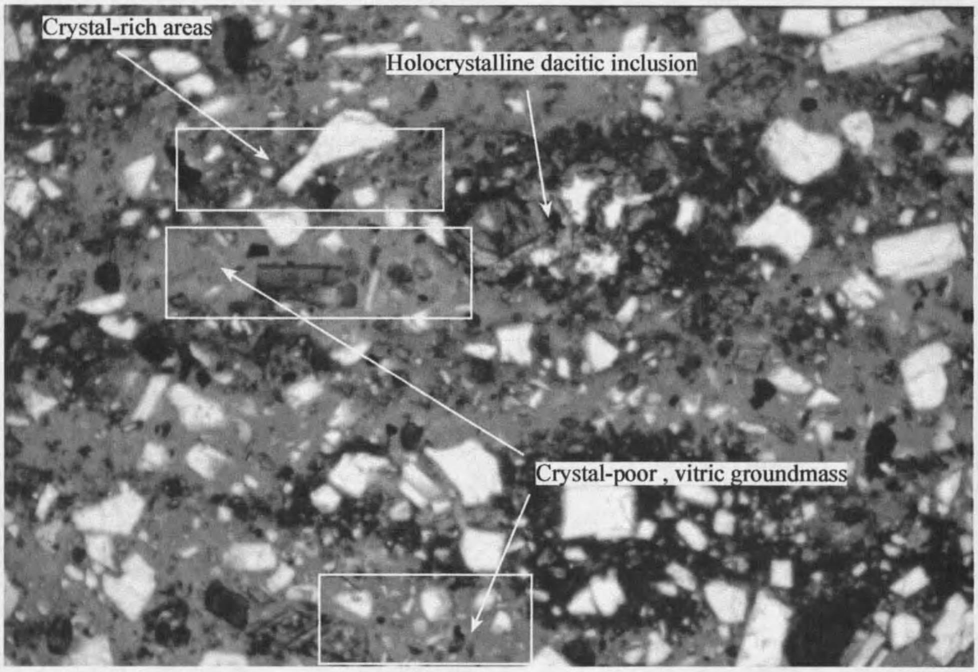

Figure 23. Disaggregating holocrystalline dacitic inclusions in dike SM9814. Note the vitric, crystal-poor nature of the host and the crystal-rich areas which are interpreted to have formed by mechanical disaggregation of the dacitic inclusions (SM9814, plane light, 25X magnification, field of view = 4.0 mm).

appear to be disaggregating, characterized by subtrachytic phenocrysts strung into the host glass (Figure 23).

The disequilibria textures recognized in some intermediate-composition EPSM rocks are compatible with a magma-mixing origin. Conversion of amphibole to biotite and Fe-Ti oxides (Figure 16) is a reaction texture that has been observed in magmatic systems capable of crystallizing "hybrogenic" biotite. Mixing of an aluminosilicate system rich in Mg and Fe with another rich in K can induce biotite crystallization at the expense of amphibole (Hibbard, 1995). It is therefore possible that the amphibole-biotite-oxide texture present in rocks from EPSM could be the result of mixing with a K-rich or hydrous magma containing pre-existing amphibole. However, this texture is by no means diagnostic of magma mixing because it has also been observed in fractionating systems due to amphibole breakdown with compositional shifts and is also observed to form during deuteric-hydrothermal alteration.

Spongy cellular plagioclase also occurs in rocks that exhibit other textures considered compatible with magma mixing. Spongy cellular plagioclase has been produced experimentally by Tsuchiyama (1985) and results from dissolution (and/or direct melting) attendant to reheating of plagioclase during magma mixing with a hotter, more mafic magma. Spongy celluar plagioclase is a texture commonly attributed to decompression of phyric magmas, although Vance (1965) suggests that decompression of water-saturated melts causes attendant crystallization, not dissolution. Therefore, spongy cellular plagioclase in amphibole-bearing EPSM rocks are interpreted to result from thermal dissolution, a texture compatible with a magma mixing origin.

Medium- to coarse-grained hornblende gabbro inclusions are interpreted as hornblende-plagioclase cumulates that were possibly entrained into the granodiorite phase of the Electric Peak stock during either initial emplacement or subsequent recharge. The presence of zoned plagioclase in these rocks suggests an igneous rather than metamorphic origin (Hibbard, 1995). Hornblende in these inclusions is petrographically identical, excepting grain-size, to hornblende in holocrystalline rocks from Electric Peak. The interstitial quartz and biotite are interpreted as intercumulate phases, and crystallized along grain boundaries and fractures during late stage solidification of the granodiorite phase. These inclusions are petrographically similar to clinopyroxenite and hornblendite cumulates from subalkalic and alkalic Eocene magmatism in the Crazy Mountains, Montana (Eggler, personal communication, 1999).

Magmatic Intensive Parameters

Aluminum-in-Hornblende Geobarometry of the Electric Peak Stock

Hammarstrom and Zen (1986) proposed that differences in Al content of calcic amphiboles are directly related to solidus pressure and developed an empirical Al-in-hornblende geobarometer. This barometer has since been verified on the basis of independently determined pressures from metamorphic aureoles in country rock (Hollister et al., 1987), and experimentally calibrated (Johnson and Rutherford, 1989; Schmidt, 1992). It has also been modified in order to account for variations in temperature and fO_2 (Anderson and Smith, 1995). Although the Al-in-hornblende barometer is not as refined as barometers calibrated for metamorphic rocks, it provides the only quantitative petrologic estimate of solidus pressure for calc-alkaline intrusive rocks.

In order to reliably apply an empirical geobarometer based on hornblende composition, Hollister et al. (1987) argue that the following conditions must be met: (1) the phases quartz, plagioclase, hornblende, biotite, orthoclase, sphene, illmentite, and magnetite must have crystallized together from a melt; (2) only hornblende rim compositions should be used; (3) crystallization pressures should be above ~2 kbar; and (4) coexisting plagioclase rim compostions should be ~An_{25}-to-An_{35}. In addition, Cawthorne (1976) emphasizes that (5) SiO_2 (α_{SiO2}) should = 1, and Anderson and Smith (1995) emphasize both the importance of (6) an independent estimate of temperature and (7) a reasonable estimate or quantitative determination of $Fe^{3+}/(Fe^{3+} + Fe^{2+})$. Five analyses of hornblende rims touching quartz grains in a granodiorite from the Electric peak stock (EP97-14) satisfy these conditions with the exceptions of conditions 3 and 7 which are discussed below.

Given the stratigraphic position of the stock and that its emplacement was intrusive and not tectonic, it is unlikely that the stock solidified at pressures >2 kbar. The problem with the application of the hornblende barometer to low-pressure intrusive rocks is that it is temperature dependent, a fact originally recognized by Hammarstrom and Zen (1986). Published phase diagrams for amphibole stability in calc-alkaline melts suggest that it can crystallize between ~950 and 650° C (Helz, 1982). Calculated pressures increase with increasing temperature, an effect that ranges from ~1.3 to >2 kbar per 100° C (Anderson and Smith, 1995). Above ~2 kbar the solidus curves for hornblende-bearing calc-alkaline melts are relatively insensitive to pressure and vary by less than

~100° C, whereas below ~2 kbar, the temperature of final crystallization increases rapidly with decreasing pressure based on the phase relations for calc-alkaline magmas of Clemens & Wall (1981) and Kenah & Hollister (1983). This phenomenon may explain why many shallow silicic intrusions (< 2kbar) yield crystallization temperatures higher than that predicted by the wet granite solidus. This introduces uncertainty regarding the behavior of temperature sensitive Al-bearing components in hornblende crystallizing below ~2 kbar. This problem, however, can be somewhat alleviated by introducing a term which corrects for temperature such as that found in the barometer calibrated by Anderson and Smith (1995).

Plagioclase-Hornblende Geothermometry
of the Electric Peak Stock

An equilibration temperature for coexisting pairs of plagioclase and hornblende in EP97-14 is calculated using the edenite-tremolite exchange thermometer (Holland and Blundy, 1994). The thermometer is designed for silica-saturated melts based on the equilibria: ednite + 4 quartz = tremolite + albite and works well over a wide range of temperatures (400-1000° C) and bulk composition. Rim compositions of coexisting oligoclase (An_{26}; analysis: EP97-14.B.1-5) and magnesio-hornblende (analysis: EP97-14.B.1-1) are used in the calculation. The calculated temperature of 715° ± 40 C provides both a crystallization temperature for the Electric Peak stock and allows for temperature correction in hornblende barometry if Anderson and Smith's (1995) barometer is used.

Electron Microprobes are not capable of distinguishing between ferric and ferrous iron, therefore total iron was initially all determined as FeO. Although Cosca et al.

(1991) demonstrated that only the 13-cation normalization procedure closely predicts site occupancies for amphiboles similar to those determined by wet chemical titration, amphiboles in this study were recalculated using a 24-oxygen hydrous formula. The chosen normalization scheme does not significantly affect calculated Al^T or pressure. It does, however, affect calculated Al^{iv} and Al^{vi} and this can change temperatures calculated using the amphibole thermometers. For the plagioclase-hornblende exchange thermometer used in this study (Holland and Blundy, 1994) the effect is minor (~15° C). $Fe^{3+}/(Fe^{2+} + Fe^{3+})$ for amphibole recalculation was fixed at 0.27, a reasonable value for calc-alkaline intrusive rocks (Dodge et al., 1968; Hammarstrom, 1982 and 1984).

Geobarometric Results

Figure 24 illustrates the range of calculated crystallization pressures for the Electric Peak stock using various published aluminum-in-hornblende barometers. Mean calculated pressures range from 0.35 ± 1.0 kbar (using Hollister et al., 1987) to 1.30 ± 0.60 kbar (using Schmidt, 1992). Anderson and Smith's (1995) barometer is the only one that takes temperature of crystallization into account and is the preferred Al-in-hornblende barometer yielding a mean crystallization pressure of 0.98 ± 0.60 kbar.

Assuming an average rock density of 2.7 g/cm^3 (Wilson, 1989) then: $P_{kbar} = 0.27(h_{km})$. Using 0.98 ± 0.60 kbar as the pressure of crystallization, an estimate based on Al-in-hornblende geobarometry suggests that the Electric Peak stock crystallized at an approximate depth of 3.6 ± 2.2 km. This pressure is consistent with the lack of a recognized metamorphic mineral assemblage in the locally hornfelsed Cretaceous sandstones and mudstones which surround the Electric Peak Stock. Moreover, this pressure is consistent with the estimated minimum thickness (2.7 km) of pre-erosional sedimentary and volcanic overburden based on stratigraphic sections constructed for the Southern Gallatin Range (Ruppel, 1972; Fraser et al., 1969; ~1.7 km of Cretaceous strata plus the thickness of erupted volcanic overburden which is ~1.0 km at adjacent Sepulcher Mountain). Higher Al^T contents in Sepulcher Mountain lavas (Figure 17) may be the result of: (1) much deeper amphibole crystallization, (2) a melt that is not saturated in the required chemical components and therefore not buffering Si-Al substitution in amphibole, or (3) much higher liquidus temperatures.

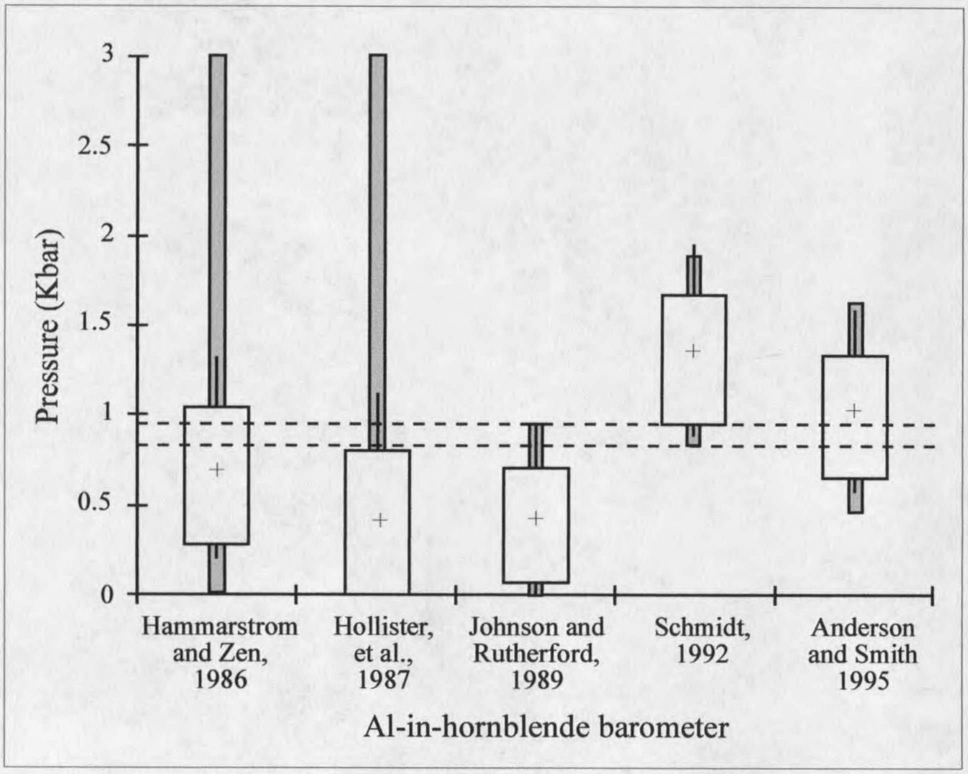

Figure 24. Calculated crystallization pressures for the Electric Peak stock using various Aluminum-in-hornblende barometers. Box-plots represent the range of pressures calculated for five different analyses of amphibole rims in EP97-14. Crosses represent median calculated pressures; the shaded bars represent each barometers uncertainty with respect to the mean. The dashed horizontal lines show the pressure range over which all barometers overlap.

Moderate-volume, calc-alkaline magmatism characteristically yields compositionally varied eruptive products in relatively short time scales (e.g. Paricutin volcano, Mexico; McBirney et al., 1987). This feature indicates that magma may be stored, and perhaps differentiated, in small, shallow reservoirs rather than in a single large magma chamber. Although shallow level storage and differentiation of calc-alkaline magmas is frequently proposed in petrogenetic models, documenting the size and shape, even presence, of these magma chambers is often overlooked.

The presence of small-volume, hypabyssal magma chambers at Electric Peak raises the question of whether or not these represent shallow magma chambers from which extrusive rocks at Sepulcher Mountain were erupted. Several observations lead to the conclusion that intrusive bodies at Electric Peak represent relatively rapidly crystallized intrusions and that differentiation of Sepulcher Mountain extrusive rocks did not likely occur in these intrusions. First, the small volume of individual intrusions (Figure 5) of the Electric Peak stock and the presence of chilled margins suggests that individual pulses of magma were very small volume (<0.25 km^3). Second, the micro-porphyry texture of holocrystalline Electric Peak intrusive rocks suggests that these magmas experienced polybaric crystallization and that physio-chemical magma chamber processes at the shallow (~3 km depth) emplacement level of final solidification were limited to interstitial crystallization and pre-existing phenocryst rim growth. Third, higher Al^T contents in Sepulcher Mountain lavas (Figure 17) likely resulted from much deeper amphibole crystallization than the solidus equilibration Al^T contents recorded by intrusive amphibole rims.

These interpretations are consistent with high-resolution (1km^3) seismic imaging of Quaternary stratovolcanoes in the Cascade and Aleutian Arcs. Lees and Crosson (1989) recognized a strong, low-velocity anomaly 9-16 km below Mt. St. Helens and suggest that this may be a zone of active magma accumulation. Benz and others (1996) did not recognize a large, low-velocity zone indicative of active magma chambers beneath Redoubt Volcano, Alaska. Power and others (1998) found no evidence of a large, low-velocity zone indicative of active magma chambers within 10 km beneath Mt. Spurr, Alaska. It is possible that subvolcanic magma chambers in intermediate-composition magmatic systems are restricted to depths >10 km, and these chambers may be smaller in volume than presently recognizable through current tomogprahic techniques due to limitations in resolution (<1 km^3).

Fe-Ti Exchange Geothermometry
<u>of Sepulcher Mountain Dacites</u>

Buddington and Lindsley (1964) proposed that the compositions of coexisting magnetite and ilmenite are dependent on temperature based on the following exchange reactions: (a) 3 Ulvospinel + 0.5 $O_2 \Leftrightarrow$ 3 Ilmenite + Magnetite and (b) 2 Magnetite + 0.5 $O_2 \Leftrightarrow$ 3 Hematite. Compositions of coexisting magnetite and ilmenite from two dacites (SM9735 and SM9724) were analyzed and average compositions of these pairs are reported in Table 7. Pre-eruptive temperatures and oxygen fugacity were determined following the method Ghiorso and Sack (1991). Calculated pre-eruptive temperatures are 800 °C (SM9735) and 900 °C (SM9724). Calculated oxygen fugacities (-log fO_2) are

−10.1 and −11.7 respectively and plot between the experimentally calibrated hematite-magnetite and nickel-nickle oxide buffers. Calculated pre-eruptive temperatures are reasonable for dacitic magmas and suggest viscosities of log 8-10 poises (McBirney, 1993). Calculated oxygen fugacities are lower than those observed for most igneous rocks (Carmichael and Ghiorso, 1986). However, this generalization may not be representative of the oxygen fugacity of other EPSM magmas. In light of the exchange reactions previously discussed, the presence of magnetite-rich spinel and roughly equal proportions of ilmenite and hematite (Figure 19) suggest that oxygen fugacity for most magmas is higher than those calculated for these two dacites. Together these features indicate variable oxygen fugacity in EPSM magmas.

Table 7. Average compositions of coexisting Fe-Ti oxides and calculated pre-eruptive temperatures and oxygen fugacity for two Sepulcher Mountain dacites.

Magnetite-Ulvospinel				Ilmenite-Hematite		
Sample	SM97-24	SM97-35		Sample	SM97-24	SM97-35
SiO_2	0.43	0.41		TiO_2	35.25	36.10
TiO_2	6.16	4.20		SiO_2	0.22	0.03
Al_2O_3	1.69	1.07		Cr_2O_3	0.06	0.03
Cr_2O_3	0.12	0.06		FeO*	55.94	57.13
FeO*	80.38	84.00		Al_2O_3	0.26	0.14
MnO	0.44	0.39		V_2O_3	0.05	0.00
MgO	0.85	0.78		MnO	0.77	0.80
ZnO	0.15	0.19		MgO	1.32	1.86
V_2O_3	0.33	0.25		ZnO	0.04	0.07
Fe_20_3 #	50.53	56.27		Fe_2O_3 #	30.08	32.03
FeO #	34.91	33.37		FeO #	28.87	28.31
Total	95.60	96.97		Total	96.91	99.38
T (C)	900	800				
Log fO_2 (bars)	-10.1	-11.7				

Note: *Total Fe reported as FeO; # Fe^{+3} and Fe^{+2} calculated by charge balance
Each analysis represents an average of at least 4 coexisting Fe-Ti oxide pairs per sample with 3-8 anlyzed per pair. Temperature and oxygen fugacity calculated by the method of Ghiorso and Sack (1991).

Aluminum-in-Hornblende Geobarometry of
Sepulcher Mountain Lavas

Al contents in calcic amphibole from Sepulcher Mountain lavas were used to calculate crystallization pressures for amphibole phenocrysts. Calculated crystallization pressures were determined for two dacitic rocks using the experimentally calibrated Al-in-hornblende barometer of Johnson and Rutherford (1989). These calculated pressures are, however, only qualitative because the Al-in-hornblende was developed for intrusive rocks whose composition satisfy the seven conditions previously discussed (e.g. Hollister et al., 1987; Cawthorne, 1976; Anderson and Smith, 1995). Because the bulk chemical composition of volcanic rocks from Sepulcher Mountain are essentially identical to those from Electric Peak application of the geobarometer is considered reasonable. Calculated crystallization pressures (based on average Al^T composition of ~7 cores) amphibole from SM9724 and SM9735 are 5.1 ± 1.65 kbar and 5.4 ± 1.65 kbar respectively.

Assuming an average rock density of 2.7 g/cm^3, then $P_{kbar} = 0.27(h_{km})$. Using an average pressure of crystallization of 5.25 ± 1.65 kbar, a qualitative estimate based on Al-in-hornblende geobarometry suggests that amphibole phenocrysts in Sepulcher Mountain lavas crystallized at a depth of approximately 19 ± 6.1 km. This suggests that phenocryst crystallization in EPSM magmas occurred at mid-crustal levels.

Pressure-Temperature Conditions

Figure 25 illustrates the pressure and temperature conditions of initial phenocryst crystallization of magmas and of final solidification of the Electric Peak stock.

Calculated P-T conditions for solidification of granodiorite (EP9714) plot on the granite water-saturated solidus of Harris et al. (1970) and Huang and Wyllie (1973) and suggest that ~ 40 mol% (~ 4 wt%) H_2O is dissolved in the magma (Burnham, 1979). Calculated pre-eruptive P-T conditions for dacites SM9724 and SM9735 plot well above the granite water-saturated solidus, indicating that ascent without attendant adiabatic cooling-related solidification is physically possible.

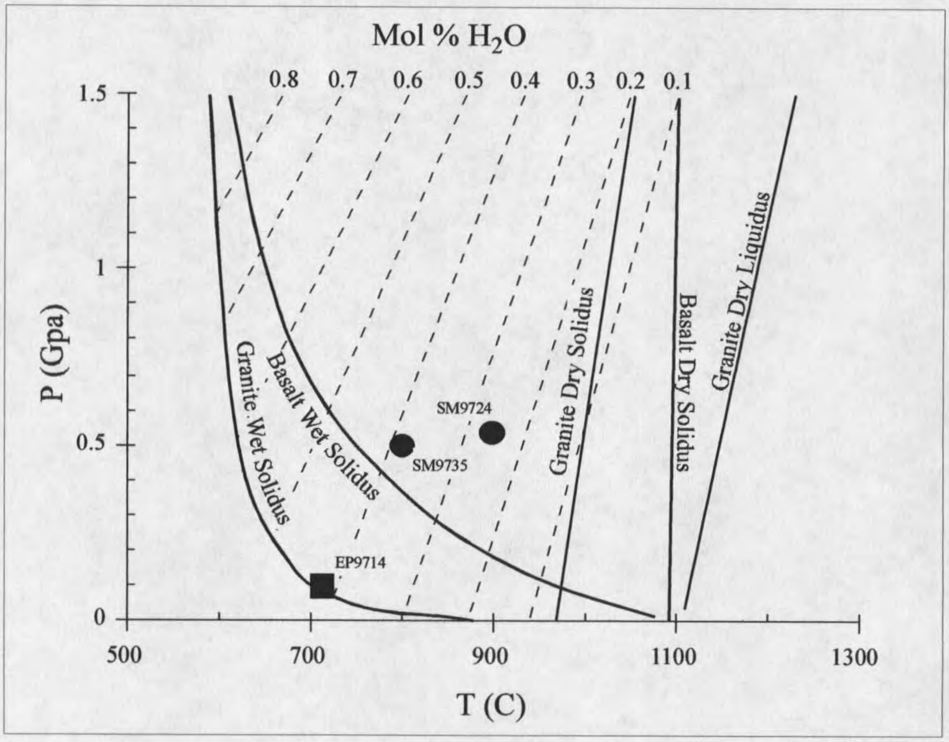

Figure 25. Pressure - temperature diagram showing some of the anhydrous and water-saturated solidus and liquidus curves for granite and basalt (after Harris et al., 1970 and Huang and Wyllie, 1973). Dashed isopleths represent the amount of H_2O (mol %) disolved in H_2O-undersaturated "granitic" melts (after Burnham, 1979). Square represents calculated T and P for solidification of granodiorite EP9714. Circles represent calculated T and P for crystallization of phenocrysts in dacites SM9724 and SM9735. Solidification temperature for EP9714 calculated using the plagioclase-amphibole thermometer of Holland and Blundy (1990) and pressure calculated using the Al-in-hornblende barometer of Anderson and Smith (1995). Phenocryst crystallization temperatures for SM9724 and SM9735 calculated using the magnetite-ilmenite thermometer of Ghiorso and Sack (1991) and qualitatitve crystallization pressures calculated using the Al-in-hornblende barometer of Johnson and Rutherford (1989).

CHAPTER 5

WHOLE ROCK COMPOSITIONS

Major and trace element abundances were determined for 41 rocks from Sepulcher Mountain and 17 rocks from Electric Peak by X-ray fluorescence spectrometry. On the basis of these analyses, a representative set of 16 rocks was selected for additional determination of rare earth element (REE) and other trace element concentrations by instrumental neutron activation analyses (INAA) and a further subset of these (n = 12) was selected for determination of Sr and Nd isotopic ratios by thermal ionization mass spectrometry (TIMS). Major and trace element compositions for representative EPSM samples are reported in Table 8 and data for all EPSM rocks are presented in Appendix G. For clarity, in the following discussion all EPSM rocks are classified using nomenclature from the total alkalies versus silica chemical classification scheme of LeMaitre et al. (1989).

Major Elements

Variations in major element compositions for EPSM rocks are illustrated with respect to SiO_2 in Figure 26. According to the classification scheme of Peacock (1931), Irving and Baranger (1971), and LeMaitre et al. (1989) EPSM rocks represent a subalkaline, medium-to high-K, calc-alkaline (alkali-lime index = 59) suite ranging continuously in composition from basaltic-andesite to rhyolite. The suite forms a calc-

Table 8. Major and trace element concentrations for representative EPSM rocks.

	SM9712	SM9709	SM9721	SM9716	SM9725	SM9704	SM9740	SM9732	SM9724	SM9706	EP9847	EP9716	EP9715	EP9717	EP9718	EP9832
Type	One	One	One	One	One	Two	Two	Two	Three	Three	Cumulate	One	One	Three	Three	Three
Major-oxide wt % (XRF)																
SiO_2	56.27	58.01	58.38	58.80	61.34	62.85	63.84	65.70	68.43	69.35	48.19	57.77	60.85	67.48	70.07	72.59
TiO_2	0.84	0.87	0.71	0.77	0.60	0.58	0.46	0.46	0.34	0.32	1.97	0.67	0.60	0.38	0.29	0.29
Al_2O_3	16.22	17.31	15.92	15.58	16.45	14.65	16.58	16.49	16.03	15.39	12.56	15.09	17.15	16.66	15.74	13.96
Fe_2O_3	8.46	7.61	7.50	7.76	6.13	5.50	3.97	4.00	2.89	2.92	12.78	7.57	6.75	3.73	2.57	2.18
MnO	0.13	0.18	0.10	0.11	0.09	0.05	0.07	0.05	0.05	0.04	0.13	0.12	0.10	0.05	0.04	0.03
MgO	6.00	3.17	4.37	5.72	3.08	4.57	1.51	1.54	1.12	2.06	10.98	6.55	3.21	1.56	1.29	0.89
CaO	7.48	6.73	6.54	6.31	5.50	4.96	4.04	3.81	3.30	2.15	9.28	6.64	5.70	3.64	2.77	2.07
Na_2O	3.26	3.94	3.33	3.58	3.88	4.01	4.29	4.17	4.66	5.38	2.74	3.74	3.94	4.65	4.66	3.74
K_2O	1.87	2.33	2.17	1.98	2.32	2.78	2.72	3.10	2.56	2.58	1.15	1.93	2.15	2.42	2.75	3.99
P_2O_5	0.25	0.37	0.24	0.23	0.22	0.28	0.25	0.24	0.13	0.11	0.08	0.25	0.24	0.17	0.11	0.07
Total	100.78	100.52	99.26	100.84	99.61	100.23	97.73	99.56	99.51	100.30	99.86	100.33	100.69	100.74	100.29	99.81
Trace element ppm (XRF)																
Ni	77	14	48	127	25	121	13	13	25	38	130	108	30	18	22	10
Cr	187	49	146	262	46	169	15	20	29	81	285	305	65	25	40	16
V	173	156	142	140	136	83	58	64	60	53	484	123	103	52	37	36
Ba	1348	1955	1383	1291	1549	2779	2475	2432	1742	1751	904	1462	1314	1894	1835	1780
Rb	36	45	37	37	35	42	48	46	48	48	16	38	41	45	49	70
Sr	647	1016	775	718	837	1410	1295	1179	711	631	388	805	764	833	763	333
Zr	150	210	149	150	152	187	198	192	137	127	82	131	164	156	138	128
Y	16	19	15	15	13	12	11	11	8	7	26	15	16	9	6	7
Nb	9.3	15.8	7.2	7.7	7.4	5.7	7.1	7.3	6.5	4.7	7.2	7.7	8.1	6.9	5.5	6.9
Pb	11	18	17	17	26	39	35	33	26	19	6	21	16	19	17	24
Trace element ppm (INAA; ICP-MS italicized)																
Sc	19.89	*18.29*	19.37	18.85	*14.55*	9.73	6.55	6.45	6.18	4.93	67	19.78	11.92	6.2	4.49	*4.55*
Hf	3.50	*4.45*	3.68	3.95	*3.45*	3.87	4.97	4.90	3.63	3.04	2.63	3.10	4.7	4.02	3.75	*3.71*
Ta	0.41	*0.61*	0.33	0.40	*0.33*	0.31	0.37	0.36	0.27	0.23	0.25	0.27	-	0.32	0.32	*0.47*
Th	5.39	*8.68*	4.54	5.35	*0.51*	15.76	10.49	9.08	4.89	4.80	1.98	1.75	6.53	5.53	5.48	*11.10*
U	0.68	*1.41*	1.04	1.05	*1.14*	2.34	1.99	1.87	1.07	1.14	0.47	0.43	1.41	1.00	1.23	*1.48*
La	34.38	*65.61*	31.33	34.57	*37.37*	108.47	76.19	72.23	27.25	26.01	16.73	30.82	34.05	33.95	29.08	*35.92*
Ce	62.09	*109.23*	63.86	72.26	*63.49*	209.04	153.98	152.44	55.19	45.22	38.97	66.78	60	66	58.30	*49.72*
Nd	26.97	*43.27*	21	26	*24.34*	78.71	52	41	15	18.16	25.70	24	28	20	15	*13.20*
Sm	4.72	*7.63*	4.29	4.35	*4.55*	10.56	6.15	5.57	2.59	2.38	6.93	4.29	4.39	3.12	2.41	*2.02*
Eu	1.33	*2.22*	1.33	1.40	*1.36*	2.13	1.65	1.67	0.83	0.67	2.10	1.57	1.19	1.01	0.80	*0.63*
Tb	0.52	*0.76*	0.50	0.53	*0.49*	0.49	0.42	0.40	0.26	0.19	1.02	0.54	0.49	0.34	0.23	*0.21*
Yb	1.44	*1.75*	1.30	1.40	*1.15*	1.50	1.41	1.40	0.75	0.63	2.16	1.37	1.62	0.88	0.70	*0.77*
Lu	0.22	*0.29*	0.18	0.20	*0.19*	0.25	0.17	0.18	0.10	0.09	0.33	0.19	0.26	0.14	0.09	*0.14*

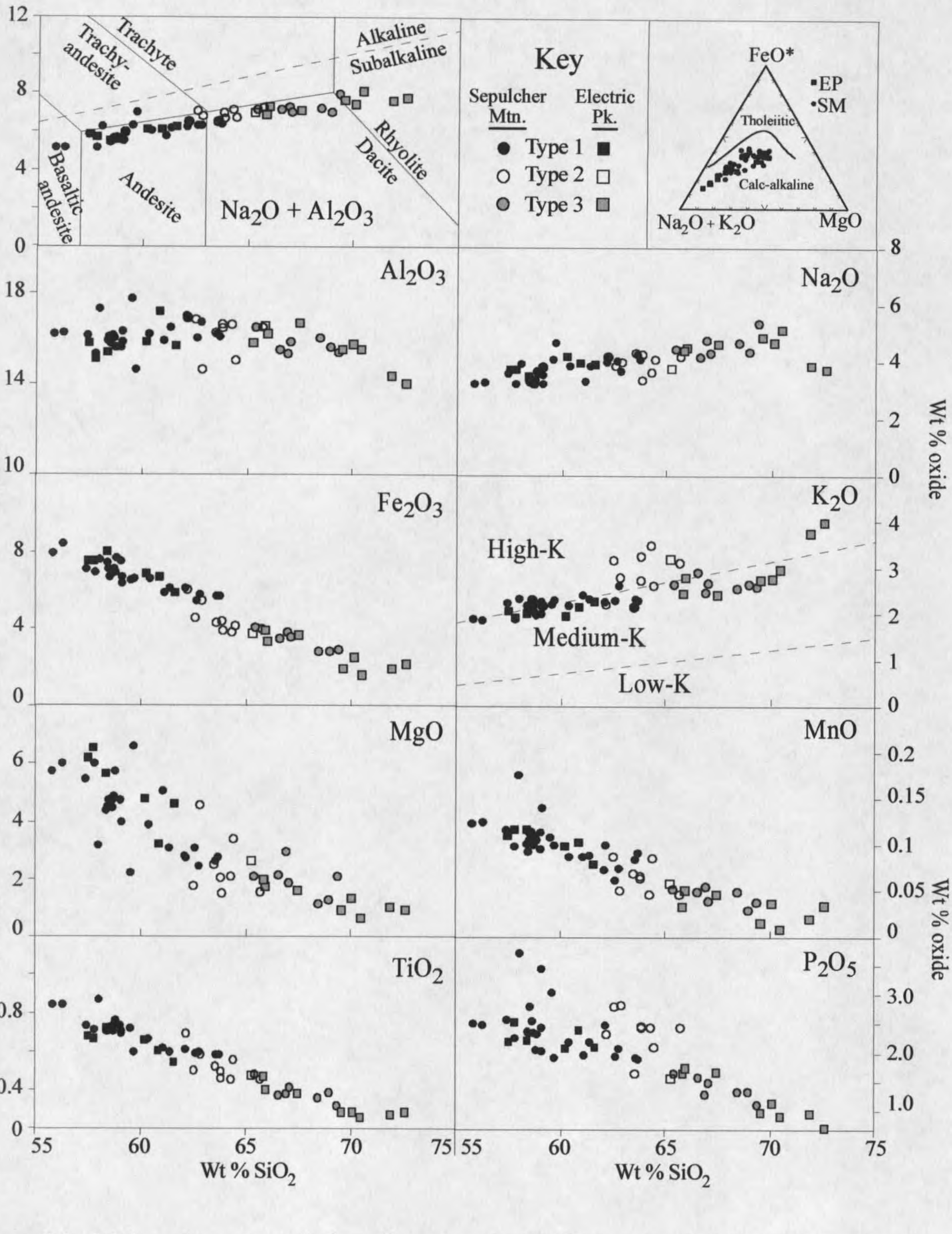

Figure 26. Major element variation diagrams for EPSM rocks. TAS classification from LeMaitre et al. (1989). Alkaline/subalkaline fields from Irving and Baranger (1971). Inset shows AFM diagram for EPSM rocks with divisions from Kuno (1968).

alkaline magmatic trend when plotted on the AFM diagram of Kuno (1968). In light of these chemical features, EPSM rocks are compositionally similar to other Eocene calc-alkaline rocks in the AVP (e.g. Mt. Washburn, Figure 1; Feeley et al., *in press*) and the Eocene magmatic belt (e.g. Norman and Mertzman, 1991; Hooper et al., 1995; Morris et al., 2000).

With respect to the identification of differentiation processes and possible magmatic sources the important major element characteristics of the EPSM suite are as follows. First, trends of major element concentrations are similar for rocks from both Electric Peak and Sepulcher Mountain. Second, major element trends with respect to SiO_2 for many elements (e.g. Na_2O, Fe_2O_3, K_2O, MnO, TiO_2) are narrow and roughly linear except for MgO, Al_2O_3, and P_2O_5, which exhibit more diffuse, wedge-shaped distributions. Third, a marked compositional gap between 62-65 wt% SiO_2 is present for rocks from Electric Peak. Fourth, silicic compositions ($\geq$ 69 wt% SiO_2) are only represented by rocks from Electric Peak. Fifth, sharp inflections are present at ~69 wt% SiO_2 for all elements except P_2O_5.

Trace Elements

Variations in trace element concentrations for EPSM rocks with respect to SiO_2 are illustrated in Figure 27. The salient trace element characteristics of the EPSM suite are as follows. First, concentrations of trace elements highly compatible in mafic minerals (Ni and Cr) scatter widely so that some andesitic and dacitic rocks have relatively high abundances of these elements (e.g. ~100 ppm Ni and ~160 ppm Cr at 64 wt% SiO_2). Second, EPSM rocks are characterized by extremely high abundances of

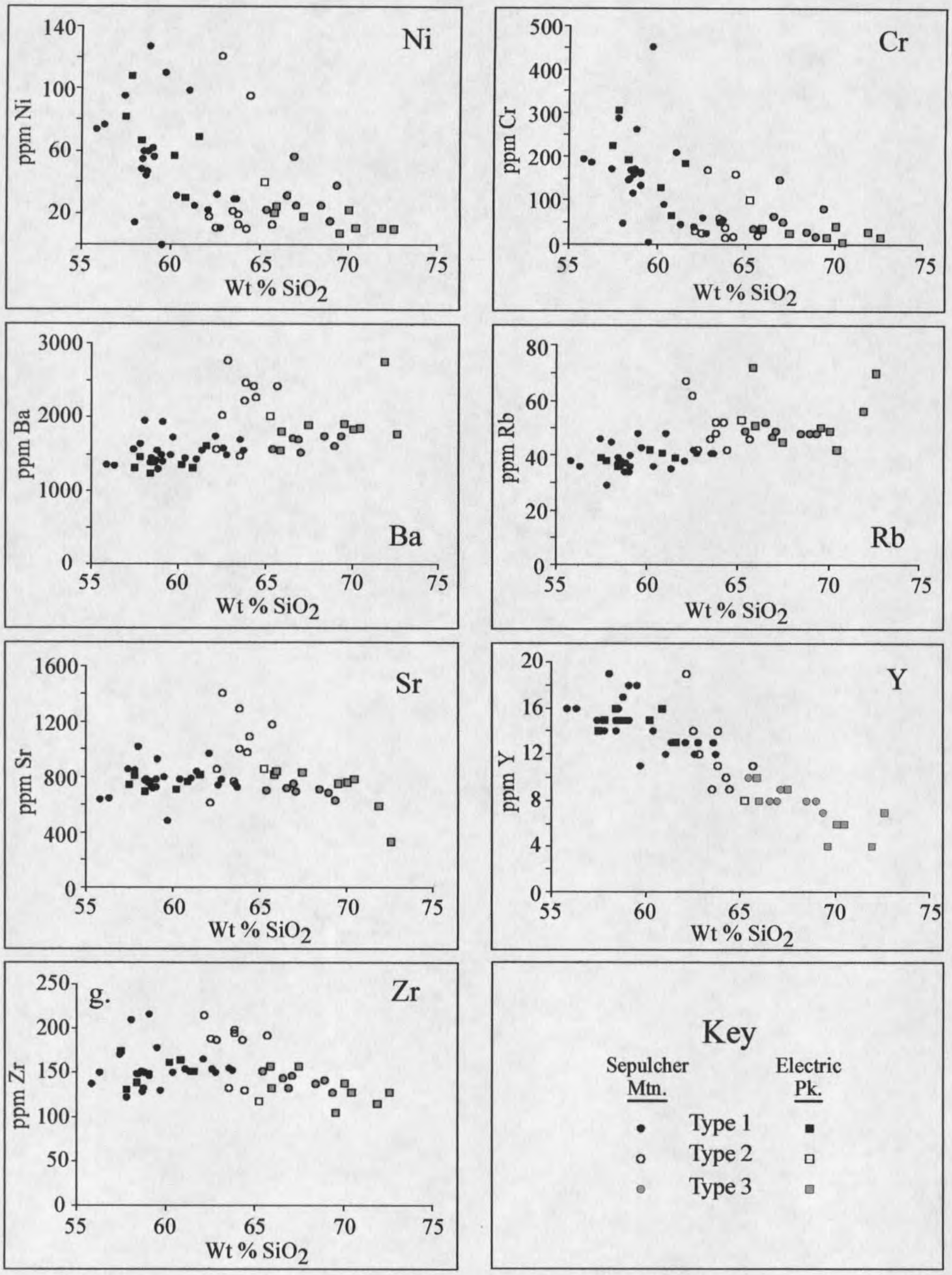

Figure 27. Trace element variation diagrams for EPSM rocks.

large ion lithophile elements (LILE) (e.g. Ba ≈ 1200-2800 ppm, Sr ≈ 400-1400 ppm) in comparison to calc-alkaline rocks in other localities with similar major element compositions (e.g. Cascades; Leeman et al., 1990). Third, concentrations of some trace elements (e.g. Ba, Sr, Zr, Y) exhibit significant scatter in low silica dacites (63-66 wt% SiO_2) and the highest concentrations of these elements occurs at these compositions. Fourth, Sr and Zr contents exhibit little variation with respect to increasing SiO_2 contents in all but the most evolved compositions. In contrast, Y concentrations decrease with increasing SiO_2 contents. Fifth, on the basis of trace element concentrations and geographic location, three groups of rocks can be distinguished.

Type 1 rocks range from basaltic-andesitic to andesitic in composition and are the most abundant rock type volumetrically. Type 1 rocks are predominately from Sepulcher Mountain and Glen Creek (Figure 3). Type 2 rocks are low-silica dacites (63-66 wt% SiO_2) distinguished by an almost two-fold increase in LILE (e.g. Ba and Sr) and elevated Zr concentrations relative to other EPSM rocks. Type 3 rocks are dacitic to rhyolitic in composition (66-73 wt% SiO_2) and are predominately from the north spur of Sepulcher Mountain, the Electric Peak stock, and the peripheral Rainbow Lakes rhyodacite dome (Figure 3). Less-evolved type 1 rocks are therefore central to the eruptive center, whereas more silicic type 2 and 3 rocks are peripheral.

Chondrite-normalized (Thompson, 1982) trace element plots for EPSM rocks are illustrated in Figure 28. All rocks exhibit similar shaped patterns with strong relative depletions in some high field strength elements (HFSE; e.g. Nb, Ta, and Ti) relative to the LILE Ba, Rb and K and the light REE La, Ce, and Nd. The HFSE Zr and Hf, however, do not exhibit negative anomalies. The patterns illustrated in Figure 28 are

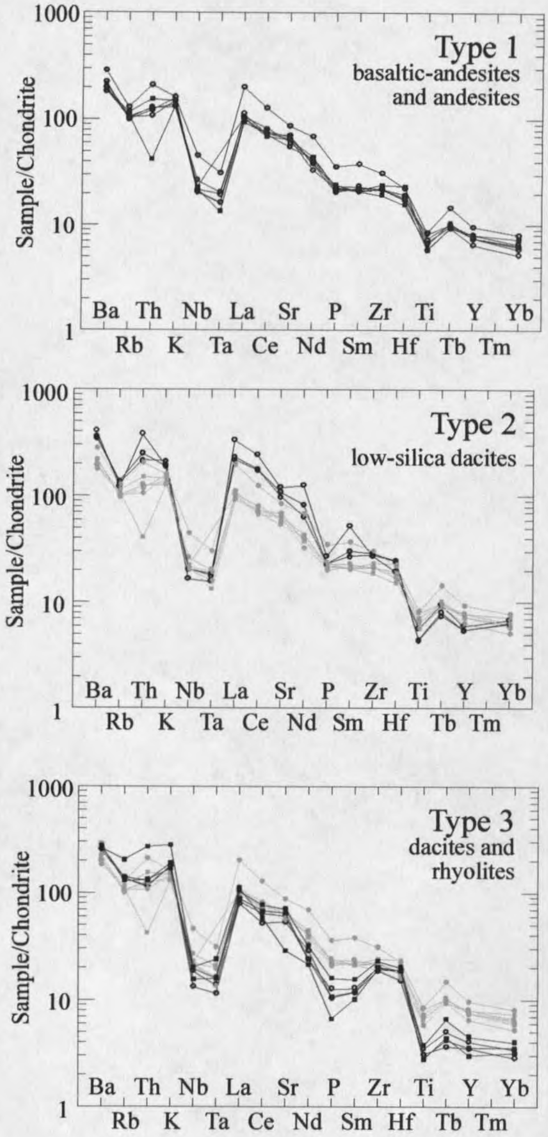

Figure 28. Trace element concentrations of EPSM rocks normalized to the composition of chondritic meteorites and plotted from left to right in order of increasing compatibility in a small fraction melt of the mantle. Normalizing values used are from Thompson (1982). Normalized concentrations of type 1 EPSM rocks are plotted in grey for comparison. Normalized trace element concentrations of rocks from Electric Peak are plotted with squares and concentrations of rocks from Sepulcher Mountain are plotted with circles.

characterized to some extent by features considered diagnostic of subduction-related magmas (e.g. Nb-Ta depletion, Ba/Ta >450, Ba/Nb >25; Gill, 1981). In light of these criteria, EPSM rocks (average Ba/Ta ≅ 5150, average Ba/Nb ≅ 238) exhibit extreme subduction-related geochemical "signatures" in comparison to rocks from known and postulated volcanic arc settings (c.f. Gill, 1981; Perfit et al., 1981; Tatsumi and Eggins, 1995).

All rocks from EPSM have light REE enriched, concave-up, chondrite-normalized REE patterns (Figure 29; Nakamura, 1974). Light REE values range from 80-300 times chondritic values and REE patterns are moderately to extremely steep ($La/Sm_n \cong 2.3$-17.0). Rocks from Electric Peak and Sepulcher Mountain with similar bulk composition exhibit identical REE patterns. EPSM rocks exhibit either no Eu anomaly or small positive Eu anomalies that are more pronounced in evolved type 3 rocks (Eu* was not quantified because Gd was not analyzed).

Absent or small positive Eu anomalies are inconsistent with the constant Sr concentrations relative to SiO_2 observed in less evolved type 1 rocks and decreasing Sr concentrations relative to SiO_2 observed in the most evolved type 3 rocks. These features indicate that fractionation of large amounts of plagioclase was not a major process during the differentiation. Slight to moderate depletion in middle to heavy REE is also apparent in all rock types but is more pronounced in evolved (SiO_2 >63 wt%) compositions (Figure 29). Decreasing middle- to heavy-REE and Y concentrations with evolution indicate that differentiation of the EPSM suite involved fractionation of substantial amounts of amphibole and clinopyroxene, or crustal melting with these phases residual. The extreme light REE enriched patterns (100-300 times chondritic values) of type 2

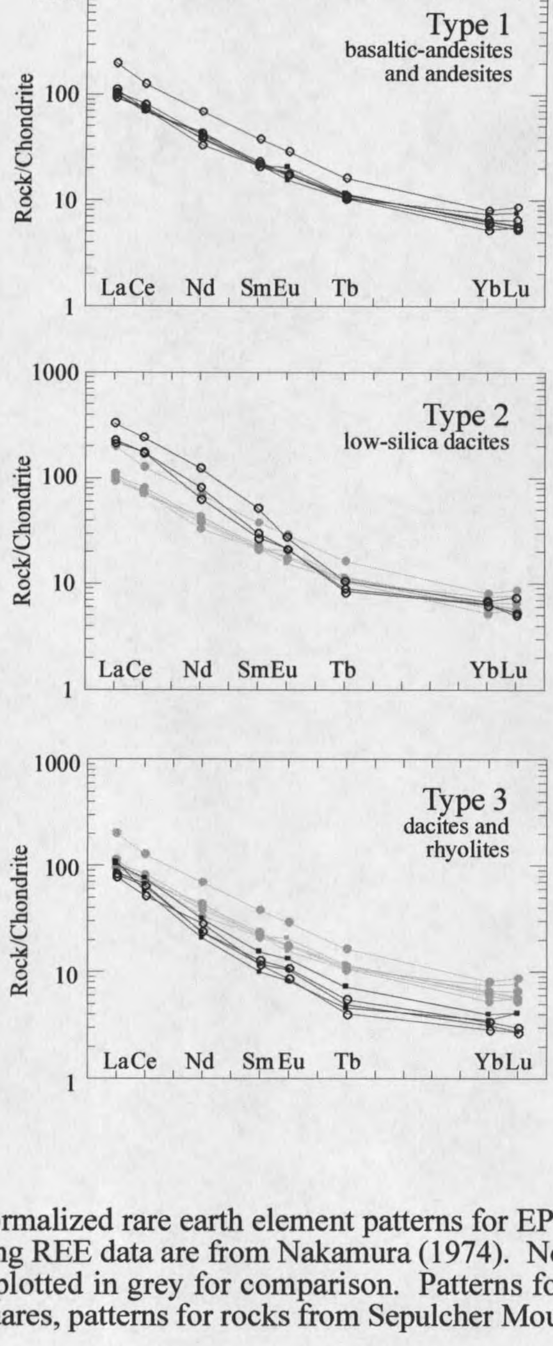

Figure 29. Chondrite-normalized rare earth element patterns for EPSM rocks. Chondrite values used in normalizing REE data are from Nakamura (1974). Normalized patterns for type 1 EPSM rocks are plotted in grey for comparison. Patterns for rocks from Electric Peak are plotted with squares, patterns for rocks from Sepulcher Mountain are plotted with circles.

rocks are anomalous in respect to rest of the EPSM suite but are consistent with the elevated LILE concentrations of these rocks.

Sr and Nd Isotopes

Measured and initial (corrected for 53 m.y. of *in situ* growth of radiogenic Sr and Nd) $^{87}Sr/^{86}Sr$ and $^{143}Nd/^{144}Nd$ isotopic ratios for twelve representative EPSM rocks are reported in Table 9 and illustrated in Figure 30. Relative to "bulk Earth" EPSM rocks have low Nd and high Sr isotopic ratios and plot within the "enriched quadrant" on Figure 30a. Although EPSM rocks have chondrite-normalized trace element patterns that display strong depletions in some HFSE relative to LILE (Figure 28), and can therefore be considered to exhibit a subduction-related geochemical "signature", they plot far from the field defined by modern subduction-related basalts (Figure 30a). Sr and Nd isotopic ratios of EPSM rocks instead project toward or plot within fields defined by deep-crustal xenoliths hosted within Eocene alkalic igneous rocks from central Montana (Joswiak, 1992) and both meta-sedimentary and meta-igneous rocks that dominate the exposed Archean basement adjacent to the AVP (Wooden et al., 1982; Meen, 1987b; Wooden and Mueller, 1988; Figure 30a). The enriched Sr and Nd isotopic compositions of EPSM rocks is characteristic of many early- to late-Cenozoic magmatic rocks emplaced within the Wyoming Province (Hearn et al., 1989) and reflects derivation from, or interaction with, ancient subcontinental lithospheric mantle (e.g., Fraser et al., 1985; Dudás et al., 1987; Dudás, 1991; MacDonald et al., 1992).

Table 9. Sr and Nd isotopic compositions of representative EPSM rocks.

	SM97-12	SM97-09	SM97-16	SM97-25	SM97-04	SM98-14	SM97-06	EP98-47	EP97-16	EP97-15	EP97-18	EP98-32
Type	One	One	One	One	Two	Two	Three	Cumulate	One	One	Three	Three
SiO_2	56.27	58.01	58.8	61.34	62.85	63.53	69.35	48.19	57.77	60.85	70.07	72.59
Rb (ppm)	36	45	37	35	42	46	48	16	38	41	49	70
Sr (ppm)	647	1016	718	837	410	768	631	388	805	764	763	333
$^{87}Sr/^{86}Sr_m$	0.706650	0.707283	0.707131	0.707017	0.707217	0.707568	0.707673	0.707405	0.706915	0.707177	0.707574	0.707710
$^{87}Sr/^{86}Sr_i$	0.706529	0.707187	0.707019	0.706926	0.707152	0.707438	0.707507	0.707315	0.706812	0.707060	0.707434	0.707253
Sm (ppm)	4.73	7.63	4.35	4.55	10.56	3.53	2.38	6.93	4.29	4.39	2.41	2.02
Nd (ppm)	27	43.3	26	24.3	78.7	20.35	18.2	25.7	24	28	15	13.2
$^{143}Nd/^{144}Nd_m$	0.511564	0.511512	0.511550	0.511858	0.511238	0.511425	0.511208	0.511561	0.511541	0.511507	0.511324	0.511485
$^{143}Nd/^{144}Nd_i$	0.511527	0.511475	0.511515	0.511819	0.511210	0.511389	0.511181	0.511504	0.511504	0.511474	0.511290	0.511453
εNd_m	-21.0	-22.0	-21.2	-15.2	-23.7	-23.7	-27.9	-21.0	-21.4	-22.1	-25.6	-22.5
εNd_i	-20.3	-21.4	-20.6	-14.7	-26.5	-23.0	-27.1	-20.8	-20.8	-21.4	-25.0	-21.8

Note: Initital Sr and Nd isotopic ratios and ε Nd values calculated using an age of 53 Ma.

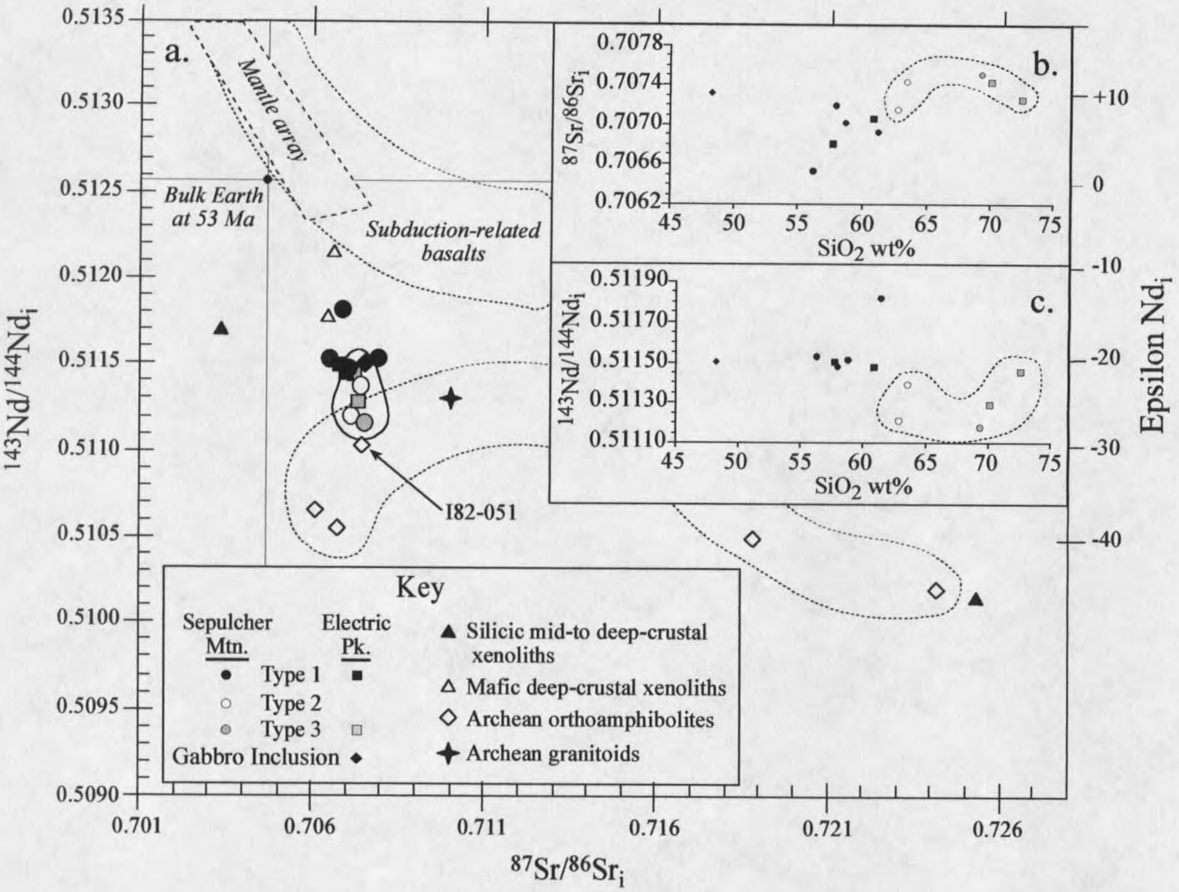

Figure 30. a. Comparison of $^{143}Nd/^{144}Nd_i$ and $^{87}Sr/^{86}Sr_i$ compositions of EPSM rocks with: modern subduction-related basalts, the mantle array, mafic to silicic lower-crustal xenoliths from the Highwood Mountains, Montana (Joswiak, 1992), Archean granitoids (Meen, 1987b) and orthoamphibolites (Meen, 1987b; Wooden and Mueller, 1988) from the Beartooth Mountains, Montana. Compositional fields for EPSM dacites and rhyolites and Archean orthoamphibolites are circled with solid and dashed lines respectively. b. $^{87}Sr/^{86}Sr_i$ vs SiO_2 for EPSM rocks. c. $^{143}Nd/^{144}Nd_i$ vs SiO_2 for EPSM rocks. EPSM dacites and rhyolites are circled with a dashed line. All initial isotopic data are calculated for an age of 53 Ma.

Non-uniform Sr and Nd isotopic compositions of EPSM rocks that vary regularly with SiO_2 abundance indicate that open-system magmatic differentiation occurred. $^{87}Sr/^{86}Sr_i$ ratios range from 0.706529-0.707507 and $^{143}Nd/^{144}Nd_i$ ratios range from 0.511181-0.511819 (Table 9). Additionally, variations in $^{87}Sr/^{86}Sr_i$ and $^{143}Nd/^{144}Nd_i$ ratios exhibit opposite trends with respect to SiO_2 (Figures 30b and 30c). The positive correlation between Sr isotopic ratios and SiO_2 abundance for less evolved type 1 rocks (Figure 30b) contrasts uniform Nd isotopic ratios (excepting one rock) over the same compositional range (Figure 30c). This feature likely reflects contamination of type 1 rocks by a crustal source with higher $^{87}Sr/^{86}Sr$ but similar $^{143}Nd/^{144}Nd$. Elevated $^{87}Sr/^{86}Sr_i$ and lower $^{143}Nd/^{144}Nd_i$ ratios observed in type 2 and type 3 rocks (relative to type 1 rocks) reflect contamination by a crustal source with higher $^{87}Sr/^{86}Sr$ and lower $^{143}Nd/^{144}Nd$. Together, these features imply that the crust beneath the EPSM eruptive center is isotopically heterogeneous.

The Sr and Nd isotopic composition of the hornblende gabbro inclusion is intermediate to those of host rocks from the Electric Peak stock (Figures 30b and 30c). This relationship is consistent with the petrographic characteristics of these abundant inclusions that indicate a cumulate origin. Together these features suggest that these inclusions are not lower-crustal mafic xenoliths such as those hosted within Eocene alkalic magmas from the Montana alkalic province (Joswiak, 1992).

CHAPTER 6

PETROGENESIS

Within the compositional diversity of extrusive and intrusive rocks from the EPSM eruptive center and on the basis of the preceding geochemical description, a number of petrogenetic processes can be recognized:

(1) Magma mixing in EPSM rocks is indicated by whole-rock chemical data and additionally supported by textural evidence. Ni-SiO_2 and Cr-SiO_2 relations (Figure 27) indicate that many intermediate composition EPSM rocks have Ni and Cr contents that are too high for their parental magmas to have fractionated large amounts of olivine. Instead, these elevated compatible-element concentrations suggest that these rocks formed through mixing between variably fractionated mafic magmas and diverse composition silicic melts.

(2) A substantial mantle component is recognized in EPSM rocks as evidenced by high MgO, Ni, and Cr contents in basaltic-andesites and elevated contents of these elements in some andesites and dacites (Figures 26 and 27). Moreover, the unique Sr and Nd isotopic compositions (Figure 30a) and elevated LILE concentrations (Figure 28) of EPMS rocks suggest that parental magmas were derived from, or interacted with, ancient subcontinental lithospheric mantle.

(3) Generation of diverse silicic crustal melts is required to explain the trace element concentrations and Sr and Nd isotopic compositions of EPSM dacites and rhyodacites. For example, REE patterns of EPSM rhyodacites (Figure 29) do not support

their derivation from magmas that produced less-evolved EPSM basaltic andesites and andesites. Additionally, evolved EPSM rocks are isotopically distinct when compared to basaltic-andesites and andesites (Figure 30b and 30c).

Evidence for Magma Mixing

Mixing between intermediate- to silicic-composition magmas and relatively mafic magmas is widely recognized. The presence of phenocryst reaction textures (Tsuchiyama, 1985; Hibbard, 1995) and elevated compatible-element contents (Novak and Bacon, 1986) provide evidence of complete magma mixing, whereas the presence of fine-grained magmatic inclusions (Bacon, 1986) indicates less-complete mixing.

Magma mixing in EPSM rocks is supported by conspicuous, although limited, textural evidence (Chapter 4). The presence of undercooled andesitic magmatic inclusions in the Rainbow Lakes rhyodacite dome indicates the injection of hotter, less-evolved magma into larger volumes of cooler, silicic magma. Additionally, the presence of disaggregating dacitic inclusions in andesitic magma provides evidence for liquid-solid magma mixing or “comingling”. Phenocryst textures, including spongy cellular and sieved plagioclase and both pervasive replacement of amphibole and mantling by thick coronae, are indicative of both thermal and chemical disequilibria in intermediate composition magmas.

A magma mixing origin for intermediate composition EPSM rocks is indicated by the high Ni and Cr concentrations in many andesitic and dacitic rocks (e.g. ~100 ppm Ni and ~175 ppm Cr at 57-64 wt% SiO_2). Fractionation of olivine, clinopyroxene, and orthopyroxene from a basaltic magma would result in rapidly decreasing concentrations of Ni and Cr with increasing SiO_2 because mineral/melt partition coefficients for these elements in mafic and intermediate composition silicate melts are significantly greater than one (Rollinson, 1993). High Ni and Cr concentrations in intermediate composition rocks are therefore difficult to explain through closed-system fractional crystallization of observed, mafic mineral phases, but would be expected to result from magma mixing between Ni- and Cr-rich mafic magmas and Ni- and Cr-poor silicic magmas

REE concentrations also point toward a magma mixing origin for intermediate composition EPSM rocks. Decreasing middle to heavy REE concentrations with evolution (Figure 29) cannot be attributed to modal phenocryst fractionation because bulk partition coefficients for the REE (excepting Eu) in modal assemblages of less evolved EPSM rocks are <1.0. Therefore, modal fractionation of the least-evolved EPSM rocks would result in increasing REE concentrations. Non-modal fractional crystallization of amphibole and plagioclase together could produce derivative magmas with concave upward REE patterns and no Eu anomaly, but this is considered an unlikely explanation because it fails to account for both the elevated Ni and Cr contents and non-uniform Sr and Nd isotopic compositions of EPSM dacites and rhyodacites.

The high Ni and Cr concentrations of some andesitic and dacitic rocks, lower REE concentrations of rhyodacitic rocks, and non-uniform isotopic ratios of EPSM rocks are attributed to mixing between variably fractionated and contaminated mafic magmas and diverse composition, silcic crustal melts. A mixing model for the origin of intermediate composition EPSM magmas is depicted in Figure 31 and provides the basis for the forthcoming discussion.

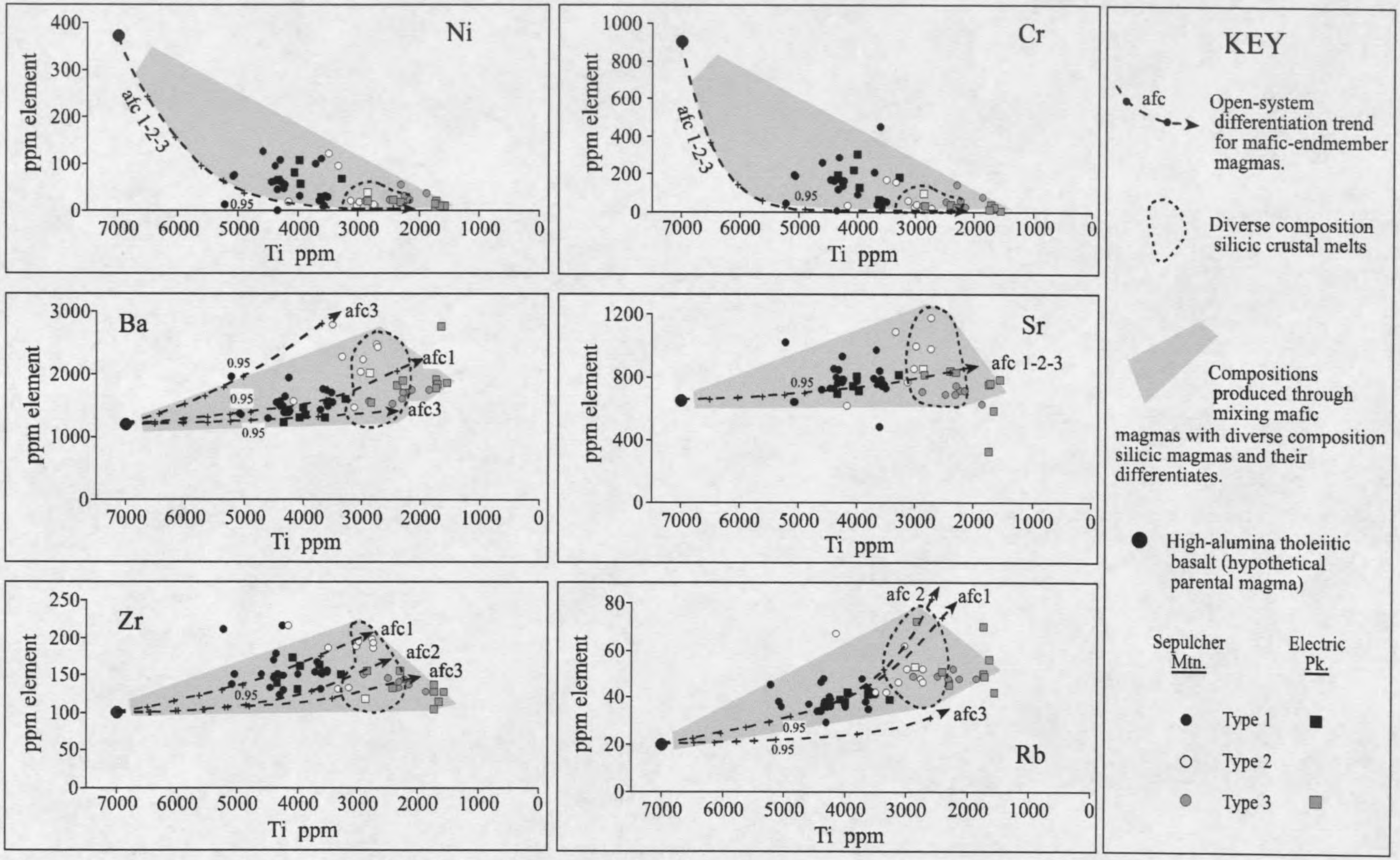

Figure 31. Petrogenetic model for the origin of compositional diversity at EPSM. The shaded field represents hybrid compositions produced through magma mixing of variably fractionated and contaminated mafic magmas with diverse composition silicic crustal melts and their differentiates. Three AFC differentiation trends (see text for discussion) for endmember mafic liquids are plotted with dashed lines (tick marks represent intervals of differentiation (F = 0.99, 0.98, 0.97, 0.96, 0.95, 0.90, and 0.80). Ti is used as an index of differentiation (decreasing Ti represents increasing differentiation of EPSM rocks).

Constraints on Primary Magma Composition

Although the least evolved EPSM rocks are not particularly mafic, general constraints may be placed on the compositions of potentially primary magmas for the purpose of petrologic modeling. Extensive laboratory experiments conducted during the past two decades on lherzolite bulk compositions under mantle pressure and temperature conditions document the wide range of silcate melts that can be produced through partial melting of the mantle. In general, primary magmas are in equilibrium with typical upper mantle mineralogies (olivine + orthopyroxene + clinopyroxene ± garnet ± spinel) and have high Ni (>400-500 ppm), high Cr (>1000 ppm), and less than 50 wt% SiO_2 (Wilson, 1989). In light of these criteria, the composition of a hypothetical primary basaltic magma (parental to mafic EPSM mixing endmembers) was calculated to reflect the average major and trace element composition of the least evolved mafic volcanic rocks from the AVP (Meen, 1987a; Hiza, 1999; Feeley, *in press*) and Montana Alkalic Province (O'Brien et al., 1991). For reference, the calculated major element composition of this hypothetical high-alumina tholeiitic basalt (HATB) is: 50.0 wt% SiO_2, 1.17 wt% TiO_2, 14.0 wt% Al_2O_3, 11.5 wt% Fe_2O_3, 0.2 wt% MnO, 10.0 wt% MgO, 10.5 wt% CaO, 2.0 wt% Na_2O, 0.7 wt% K_2O, and 0.2 wt% P_2O_5. The calculated trace element composition of HATB is: 375 ppm Ni, 900 ppm Cr, 1200 ppm Ba, 650 ppm Sr, 100 ppm Zr, and 20 ppm Rb. High Ba and Sr concentrations were selected because geochemical characteristics of other Eocene igneous centers in the AVP (Meen and Eggler, 1987), Montana Alkalic Province (Dudás et al., 1987; McCallum et al., 1989) and Challis volcanic field (Norman, 1988) indicate the participation of LILE-enriched, mid-Proterozoic, lithospheric, sub-continental mantle in the generation of primary magmas.

<u>Origin of Intermediate Composition Magmas</u>

The range of trace element concentrations displayed by EPSM basaltic-andesites and andesites indicates that mafic endmember magmas involved in mixing exhibited significant compositional diversity. In order to better characterize potential mafic endmember magmas for use in mixing models, eleven combined assimilation and fractional crystallization (AFC) models were attempted using different assimilants and fractionating assemblages. Fractional crystallization is not considered a suitable process because the positive correlation between Sr isotopic ratios and SiO_2 in less-evolved rocks indicates that open-system differentiation occurred.

Following the methodology of DePaolo (1981), AFC models were calculated to simulate open-system differentiation under lower-crustal conditions. High-pressure conditions are indicated because uniform Sr contents, increasingly positive Eu anomalies, and decreasing REE contents relative to increasing SiO_2 are inconsistent with low-pressure fractionation of plagioclase-rich mineral assemblages. Successful models involve Raleigh fractionation (Rollinson, 1993) of 40% clinopyroxene, 30% olivine, 27% plagioclase, and 3% Fe-Ti oxides, and use intermediate values for the range of mineral/melt partition coefficients reported in the GERM database (Appendix H). This plagioclase-poor assemblage is expected to crystallize from basaltic magma under conditions of high pressure following the experimental work of Sisson and Grove (1993). AFC models were calculated using a high (0.8) rate of assimilation relative to fractionation. This value is considered to reasonably approximate lower crustal conditions where wallrock is at elevated ambient temperatures (Reiners et al., 1995). In AFC modeling Ti is used as an index of differentiation because it exhibits strong correlation with SiO_2.

The three most successful AFC models are illustrated in Figure 31. Calculated trends involve fractionation of the crystallizing assemblage discussed above and crustal assimilants comparable in composition to the average of granulite-facies, Archean, basement orthoamphibolites (trend "afc1") from the Beartooth Mountains, Montana (data in Wooden et al., 1982; Meen, 1987b; Mueller et al., 1988) and both pyroxene-granulite (trend "afc2") and charnockite (trend "afc3") lower-crustal xenoliths from the Highwood Mountains, Montana (data in Joswiak, 1992).

AFC of lower-crustal compositions is successful in accounting for the contrasting wedge-shaped fields in Figure 31 defined by large variations in Ni and Cr for basaltic andesites and Ba, Sr, Zr, and Rb for andesites. The most important difference between the three AFC models illustrated in Figure 31 is that Ba contents are elevated more rapidly whereas Rb contents are elevated less rapidly during assimilation of silicic xenoliths (trend "afc3"). AFC of potentially primary magmas cannot explain all the compositional variability observed in EPSM rocks, particularly the elevated compatible-element concentrations (Ni and Cr) in andesitic and dacitic rocks and wide range of LILE concentrations in dacitic rocks. However, the model AFC trends suggest that only small amounts ($F > 0.90$) of open-system differentiation of a potentially primary magma (HATB) are necessary to produce the range of Ni and Cr contents in endmember mafic liquids required for two-component magma mixing with diverse composition dacitic magmas.

In order to better distinguish between these lower-crustal assimilants, AFC models were also calculated using Sr and Nd isotopic data. The published isotopic ratios for crustal assimilants used in AFC modeling are corrected for 53 m.y. of *in situ* growth of radiogenic Sr and Nd. The starting Sr and Nd isotopic composition (C_o) used in AFC models is that of a basalt from the Independence Volcano in the Absaroka volcanic province (Sample 2080; Meen, 1987a). The relative enrichment or depletion in $^{87}Sr/^{86}Sr_i$ and $^{143}Nd/^{144}Nd_i$ ratios predicted by AFC modeling is, however, relatively independent of the starting composition. The AFC trends illustrated in Figure 32 represent differentiation of a potentially primary magma contaminated by basement orthoamphibolites (trend "afc1") from the Beartooth Mountains (data from Wooden and Mueller, 1988) and both pyroxene-granulite (trend "afc2") and charnockite (trend "afc3") xenoliths from the Highwood Mountains, Montana (data from Joswiak, 1992). The large range in $^{143}Nd/^{144}Nd$ relative to $^{87}Sr/^{86}Sr$ for EPSM rocks (Figure 30) indicates that differentiating mafic magmas assimilated crustal rocks with low $^{87}Sr/^{86}Sr$ and $^{143}Nd/^{144}Nd$ ratios. Low-$^{87}Sr/^{86}Sr$ orthoamphibolites from the Beartooth Mountains exhibit these features (Figure 30a). Assimilation of these rocks (trend "afc1") radically decreases Nd isotopic ratios relative to corresponding Sr isotopic ratios (Figure 32). In contrast, assimilation of two-pyroxene granulites increases $^{143}Nd/^{144}Nd$, and assimilation of charnockites drastically increases $^{87}Sr/^{86}Sr$. Therefore, AFC modeling of Sr and Nd isotopic data refines the results of trace element AFC models and suggests that differentiation of mafic magmas (EPSM mixing endmembers) involved assimilation of rocks similar in composition to Archean orthoamphibolites exposed in the Beartooth Mountains.

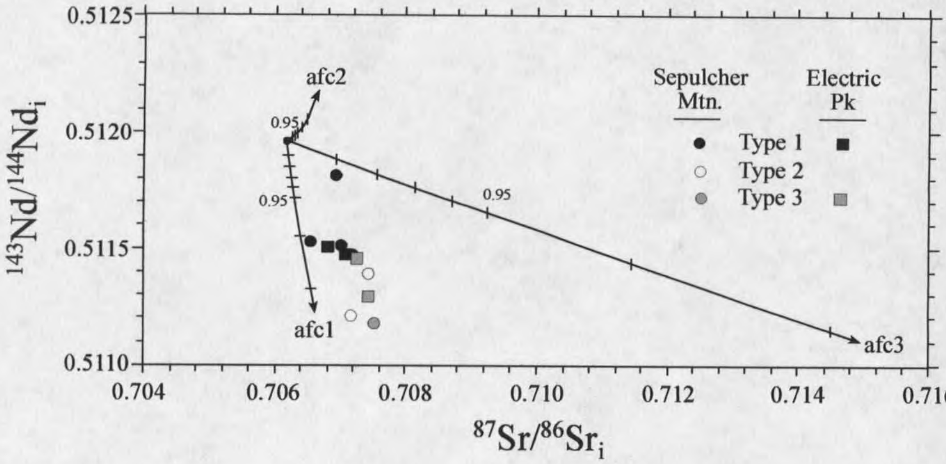

Figure 32. Calculated assimilation-fractional crystallization models for $^{87}Sr/^{86}Sr_i$ and $^{143}Nd/^{144}Nd_i$. Illustrated trends represent differentiation of a potentially primary magma contaminated by basement orthoamphibolites from the Beartooth Mountains, Montana (afc1) and both pyroxene granulite (afc2) and charnockite (afc3) deep-crustal xenoliths from the Highwood Mountains, Montana. Tick marks represent fraction of original magma remaining.

Origin of Silicic Magmas

In this section the derivation of dacitic EPSM magmas by partial melting of lower-crustal rocks is evaluated. This is accomplished by (1) inferring the trace element chemistry of possible source regions, (2) addressing the potential for melt production or "fertility" of these sources, and (3) employing trace element partial melting models of crustal rocks.

Trace element compositions of silicic EPSM rocks are characterized by significant diversity in Ba and Sr concentrations (e.g. 400-1400 ppm Sr), low Rb/Sr ratios

(< 0.1), and strong enrichments in light REE relative to middle and heavy REE (Ce/Yb_n = 16-36). Together, these features indicate a heterogeneous, LREE-rich, Rb-poor source region. Basement orthoamphibolites and lower-crustal granulite xenoliths from the Wyoming Province both possess these features and therefore represent possible magmatic source regions.

Archean basement orthoamphibolites from the Beartooth Mountains are described in detail by Wooden et al.(1982), Meen (1987b), and Mueller et al. (1988). These rocks exhibit a wide range of LILE concentrations (e.g. Ba ≅ 200-2500 ppm, Sr ≅ 200-1000 ppm) and low Rb concentrations (17-79 ppm). Although, these amphibolites possess enrichments in light REE relative to heavy REE (Ce/Yb_n = 8-10; Meen, 1987b), they are not as greatly enriched as those observed in silicic EPSM rocks. The strong enrichment in LILE relative to HFSE exhibited by silicic EPSM rocks is also typical of Archean orthoamphibolites (Mueller et al., 1983).

Mafic and silicic granulite xenoliths from the Highwood Mountains are described by Joswiak (1992) and exhibit contrasting trace element chemistry. Ba contents of mafic two-pyroxene granulites (~300-600 ppm) are much lower than those observed in charnockites (~400-7000 ppm), whereas Sr contents display a more restricted range (200-700 ppm) in both mafic and silicic compositions (Joswiak, 1992). Rb contents are < 16 ppm for the two-pyroxene granulites and 14-130 ppm for charnockites. Although silicic xenoliths exhibit strong light REE enrichment (Ce/Yb_n ≅ 40), mafic xenoliths typically display relatively flat REE patterns (Ce/Yb_n ≅ 2.0).

Crustal rocks vary widely in their "fertility" as magma sources. Intermediate composition amphibole-rich rocks are potentially highly fertile magma sources provided the high temperatures (~850-900° C) necessary for amphibole breakdown are realized. In contrast, pyroxene-rich mafic rocks and quartzofeldspathic rocks are much less potentially fertile unless extreme temperature conditions are reached (Clemens and Vielzeuf, 1987). Experiments in the system $CaO-MgO-Al_2O_3-SiO_2-H_2O$ and on natural rock compositions (Naney, 1983; Rutter and Wyllie, 1987) indicate that major amphibole dehydration-partial melting reactions occur at 900° and 920° C at 5 and 10 kbar, respectively. The generalized reaction involves the breakdown of amphibole yielding a melt that coexists with plagioclase, quartz, and two pyroxenes (the typical assemblage of mafic granulites). For these reasons, rocks similar in composition to the two-pyroxene granulite and charnockite xenoliths from the Highwood Mountains are considered relatively unfertile sources. Instead, source regions for silicic EPSM magmas likely consisted of more fertile amphibole-bearing rocks, similar in composition to Archean basement orthoamphibolites exposed in the Beartooth Mountains.

Amphibole-rich lower crust derived from granulite-facies metamorphism (3,000 – 2,800 Ma) of older mafic and intermediate composition magmatic rocks is postulated to exist beneath the AVP (Mueller et al., 1983; Meen and Eggler, 1989). Trace element models are consistent with the generation of EPSM dacites by small, but variable, degrees of partial melting of this crust. Incremental batch melting equations were used to calculate trace element abundances in derivative silicic melts. Partition coefficients for the REE represent average values reported in the GERM database. P-T parameters were chosen to represent melting under fluid-absent middle- to lower-crustal conditions (865-950° C, 7kbar, $P_{H2O}<P_{Total}$). The modes for source residuum were estimated from the experimental data of Beard and Lofgren (1991) as a function of melt fraction. As an

approximation, the composition of lower crustal amphibolites used in modeling is based on the published analysis of an Archean intermediate-composition (56 wt% SiO_2) basement orthoamphibolite from the Beartooth Mountains (Sample I-82-051; Meen, 1987b).

Crustal melting models reproduce the compositions of EPSM dacites (Figure 33) and demonstrate the plausibility of generating felsic EPSM magmas by partial melting of amphibolitic lower crust. The composition of type 2 EPSM dacites is best modeled by 20% partial melting of amphibolitic rocks leaving an anhydrous residuum. The absence of amphibole and abundance of plagioclase in the residuum results in compositions that exhibit pronounced negative Eu anomalies that are not observed in EPSM rocks (Figure 33). This feature may indicate oxidizing magmatic conditions with a resulting low Eu^{2+}/Eu^{3+} ratio (McKay, 1989). Melting models also predict slightly higher heavy REE element concentrations than those observed in type 2 dacites. This attribute probably represents slight differences between the modeled residua and actual source mineralogy. It may indicate the presence of small amounts of residual garnet or zircon, minerals with high partition coeffients for the heavy REE. Deviations in the REE contents of type 2 dacites from calculated melts therefore most likely reflect slight differences in restite mineralogy and melt fO_2.

The compositions of type 3 dacites are approximated by 15% partial melting of amphibolitic crust leaving a hydrous, amphibole-bearing residuum. The presence of residual amphibole yields melts with lower middle- and heavy-REE contents similar to those of type 3 dacites. However, smaller degrees of partial melting do not reproduce the slightly lower light REE contents exhibited by type 3 dacites. This feature most likely indicates compositional variability in the source region of EPSM dacites. Thus, the differences in trace element chemistry between type 2 and 3 EPSM rocks most likely represent the effects of the degree of melting and consequent presence or absence of amphibole in the residuum and source compositional heterogeneity.

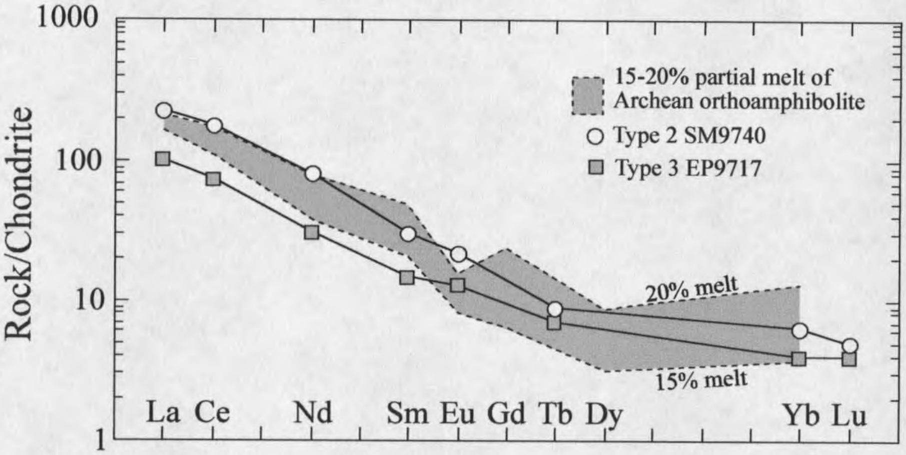

Figure 33. Results of crustal melting models for type 2 and type 3 dacitic rocks. Chondrite-normalized (Nakamura, 1974) REE concentrations are modeled by partial melting of amphibolitic lower crust approximated by the composition of Archean basement orthoamphibolites from the Beartooth Mountains, Montana (data in Meen, 1987b). Darkened field is the REE pattern calculated for 15-20% dehydration partial melting leaving restites with Plag:Amph:Cpx:Opx = 45:45:7:3 and 52:0:32:16, respectively. Representative REE patterns for both type 2 and type 3 EPSM dacites are illustrated for reference.

The compositional range observed in EPSM dacites can be accurately modeled to reflect 15-20% partial melting of an amphibolititc source leaving restite with variable plagioclase/amphibole ratios. The modeled residual mineralogy for type 2 dacites is: 48% plagioclase, 30% clinopyroxene, 15% orthopyroxene, 5% ilmenite, and 2% magnetite; whereas the modeled residual mineralogy for type 3 dacites is: 39% plagioclase, 39% amphibole, 6% quartz, 6% clinopyroxne, 3% orthopyroxene, 4% ilmenite, and 3% magnetite.

Some of the compositional variation exhibited by more silicic (> 68 wt% SiO_2) type 3 rocks may reflect limited fractional crystallization of crustal melts prior to mixing with intermediate-composition magmas. It is not possible to uniquely model these processes because the composition of undifferentiated dacitic magma is itself model dependent. However, simple Rayleigh fractionation models indicate that dacitic magmas must undergo ~10-20% fractional crystallization of a plagioclase and amphibole-rich mineral assemblage to produce the trends in Ba and Sr concentrations observed in type 3 rocks. Least-squares mass balance calculations (Table 10) allow such a process because they predict small sums of the squared residuals for major elements and plagioclase-dominated fractionating assemblages similar to those observed in type 3 rocks. The plagioclase and amphibole-rich fractionating assemblage predicted by models is consistent with the mineralogy of abundant hornblende gabbro cumulates present in silicic intrusive rocks from the Electric Peak stock. Fractionation of small amounts (<0.05 wt%) of trace phases including allanite, zircon, and apatite may also explain the decreasing REE, Zr, and P_2O_5 contents relative to increasing SiO_2 observed in type 3 rocks.

Table 10. Fractional crystallization model for dacitic and rhyolitic rocks.

Wt%	Parent SM9733	Daughter EP9718	Calculated daughter	Residual solution difference	Phases	Wt%
SiO_2	65.85	70.05	70.01	0.05	Plagioclase (An_{40})	57.4
TiO_2	0.49	0.29	0.25	0.04	Edenitic Hornblende	27.6
Al_2O_3	16.56	15.74	15.68	0.06	Biotite	10.3
FeO	3.72	2.31	2.27	0.04	Magnetite (Mt_{56})	4
MnO	0.05	0.04	0.04	-0.01	Ilmenite (Ilm_{67})	0.6
MgO	2.08	1.29	1.14	0.15	F	0.83
CaO	3.94	2.77	2.94	-0.17	Σr^2	0.172
Na_2O	4.48	4.66	4.49	0.17		
K_2O	2.67	2.75	3.02	-0.27		
P_2O_5	0.17	0.11	0.21	-0.1		

Note: Mineral compositions are those given for SM9735 in Tables 1-7; F = fraction of magma remaining
Σr^2 = sum of the squares of residuals.

Summary

The proposed model for the origin of compositional diversity is constrained by the geochemistry and isotopic compositions of EPSM rocks and is illustrated in Figure 31. In this model the majority of andesitic rocks, and high-Ni and-Cr dacites and rhyolites, are produced through mixing of variably fractionated and contaminated mafic magmas with diverse composition silicic crustal melts and their differentiates. Mafic mixing endmembers are derived through fractionation ($F > 0.9$) of a clinopyroxene-rich, plagioclase-poor mineral assemblage from primary mantle-derived melts that have been contaminated by Archean crust. Silicic mixing endmembers are derived by partial melting of amphibolitic lower-crust leaving restites with variable proportions of plagioclase, amphibole, and pyroxene. The lower-crustal source consists of LILE-enriched amphibolites similar in composition to Archean basement orthoamphibolites exposed in the Beartooth Mountains, Montana. Limited fractional crystallization ($F > 0.8$) of these crustal melts produced rhyolitic magmas also involved in mixing.

CHAPTER 7

DISCUSSION

Petrogenetic Model

Integration of the petrologic and geochemical data described in this study can be used to construct a generalized model for the magmatic evolution of the EPSM eruptive center. A schematic cross-section illustrating the main features of this petrogenetic model is illustrated in Figure 34. The key components of this model are as follows. 1) Primary mantle-derived magmas intrude the crust as a plexus of overlapping basaltic dikes fractionating clinopyroxene-rich mineral assemblages and assimilating conduit wallrock at lower-crustal levels. 2) The time-integrated effect of repeated dike intrusion is escalating crustal temperatures. Consequent dehydration partial melting of amphibolitic crust yields diverse composition dacitic magmas. An integral component of this model is that intrusion of basalt, crustal melting, and magma mixing are intimately associated within this dike network. This process is analogous to that described by Hopson and Mattinson (1994) for the origin of the Chelan migmatite complex in the North Cascades and it produced the bulk of andesitic magmas at EPSM. 3) Magmas ascend to upper-crustal magma chambers where they crystallize equilibrium mineral assemblages and in some cases fractionate plagioclase and amphibole-rich mineral assemblages. Hybrid andesitic magmas yield the dominant volume of rocks at Sepulcher Mountain, whereas less-hybridized dacitic and rhyolitic magmas erupt at small-volume peripheral vents. Some of these magmas stall and solidify at shallow crustal depths (~3 km) producing the various intrusive phases of the Electric Peak stock.

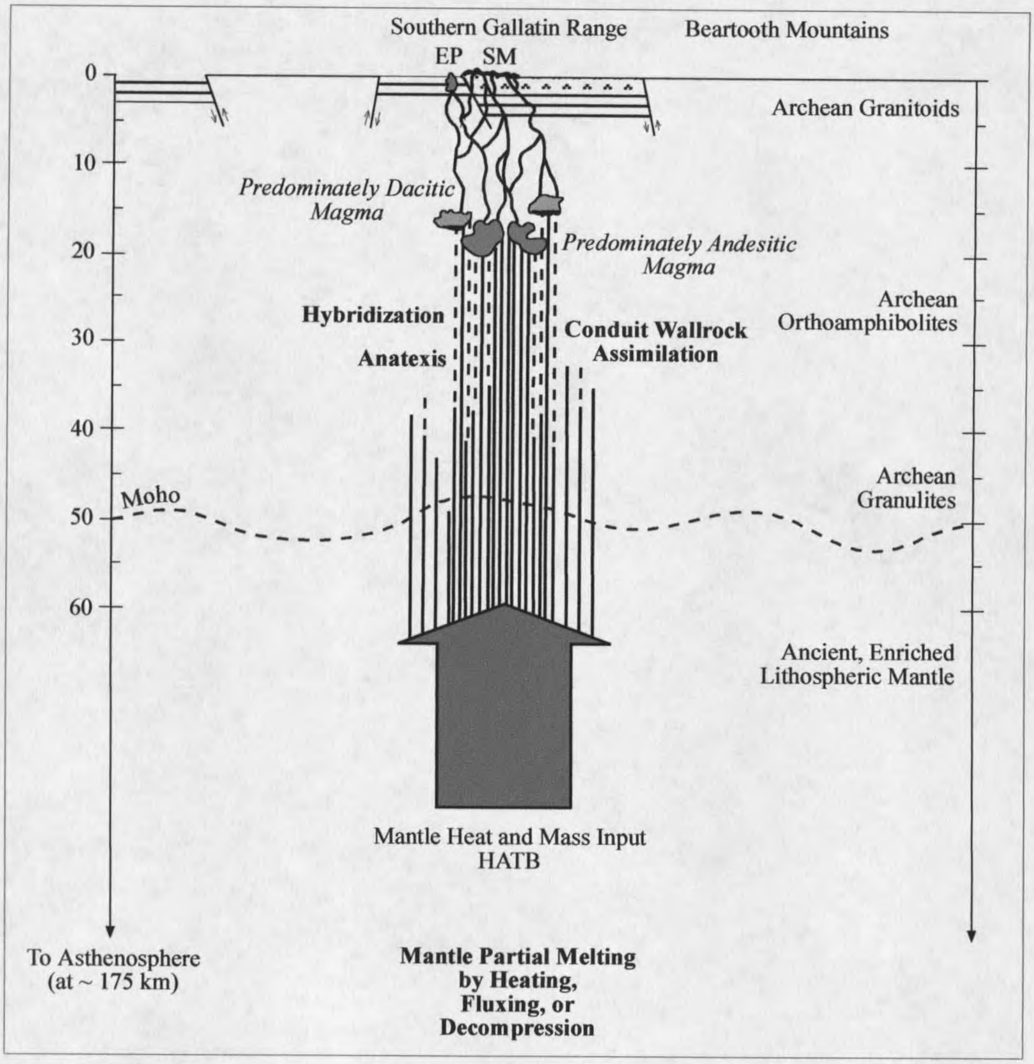

Figure 34. Schematic petrogenetic model for the orign of compositional diversity of calc-alkaline magmas at Electric Peak and Sepulcher Mountain. Solid lines represent ascending basaltic and hybrid andesitic magmas; dashed lines represent ascending less-hybridized dacitic magmas. Horizonally-ruled pattern represent Phanerozoic sedimentary rocks, inverted "v" pattern represents Eocene volcanic and volcaniclastic rocks.

Implications for the Origin of Magmas in the AVP

The results of this study are significant because they indicate that a considerable crustal component was involved in generating calc-alkaline magmas in the Absaroka volcanic province. Prior to this study, a simple closed-system magmatic differentiation history was assumed for calc-alkaline rocks in the AVP. Simple phenocryst assemblages of these rocks and smooth linear trends of major element compositions were cited as evidence for differentiation through closed-system fractional crystallization. Iddings (1891) recognized a regular change in phenocryst assemblage with whole-rock composition at the Electric Peak-Sepulcher Mountain eruptive center and suggested that compositional variation was the result of "chemical differentiation of a general magma." Schultz (1967) interpreted calc-alkaline rocks at Mt. Washburn (Figure 2) to have formed by "fractional crystallization…in a relatively shallow magma chamber." LaPointe (1977) concluded that volcanic and intrusive rocks at the Sylvan Pass area (Figure 2) are "probably cogenetic, resulting from successive tapping of a single parent magma at various stages in its magmatic differentiation."

The petrogenetic model proposed for the origin of calc-alkaline magmas at the EPSM eruptive center also has implications for the origin of across-strike geochemical variations in the AVP. The wide range of K_2O contents at constant SiO_2 content (~0.9 to 5.0 wt % at 55 wt % SiO_2; Chadwick, 1970; Meen, 1987a; Hiza, 1999) exhibited by rocks across the AVP are similar to those observed at many subduction-related volcanic arcs (e.g. Gill, 1981; Tatsumi and Eggins, 1995) although the origin of these variations is unclear.

The results of petrologic research on the shoshonititc Independence Volcano (Meen, 1987a; Meen and Eggler, 1987; Figure 2) are provocative in regards to the origin of K_2O variations across the AVP. Meen (1987a) concludes that major and trace element, Sr and Nd isotopic, and experimental data are consistent with formation of shoshonitic magmas from calc-alkaline basaltic andesitic magma by fractionation of phenocryst phases without interaction of crustal rocks. His experimental studies indicate that high-pressure (~10 kbar) fractional crystallization of plagioclase, hypersthene, augite, and magnetite from an anhydrous, mantle-derived, low-K (K_2O ≤0.3%) mafic magma produces derivative liquids enriched in K_2O with respect to SiO_2 (shoshonitic trend). Fractional crystallization of olivine, plagioclase, and clinopyroxene from the same parental magma at low pressures (1 atm) or under hydrous conditions produces derivative liquids only moderately enriched in K_2O with respect to SiO_2 (calc-alkaline trend). Meen's results therefore imply that "K-poor" calc-alkaline magmas from the western AVP reflect low-pressure fractional crystallization in shallow magma chambers of the same parental magmas that produce "K-rich" shoshonitic magmas by high-pressure fractional crystallization in the eastern AVP (e.g. Independence Volcano).

The compositional diversity of EPSM rocks instead indicates that calc-alkaline magmas evolved primarily through open-system magmatic processes. This origin suggests that a simple increasing depth to magma chamber relationship cannot explain variations in K_2O contents across the AVP. Given these results, interactions between mantle-derived magmas and continental crust must also be considered in the genesis of diverse composition magmas across the AVP.

CHAPTER 8

CONCLUSIONS

The results obtained by this study through field observations, petrographic and geochemical characterization, and petrogenetic modeling of igneous rocks from Electric Peak and Sepulcher Mountain are permissive of the following conclusions.

(1) Igneous rocks at Electric Peak and Sepulcher Mountain form a subalkaline, medium- to high-K, calc-alkaline suite ranging in composition from basaltic-andesitic through rhyolitic.

(2) Major and trace element concentrations and Sr and Nd isotopic compositions of hypabyssal intrusive rocks from the Electric Peak stock and extrusive rocks and dikes from Sepulcher Mountain are very similar. These rocks are therefore interpreted to be comagmatic. Intrusive rocks from Electric Peak should formally be included in the Absaroka Volcanic Supergroup.

(3) The Electric peak stock exhibits sharp compositional zoning that is attributed to the stalling and solidification of multiple, small-volume magmatic injections into shallow crustal levels (~3 km depth) and does not represent the *in situ* differentiation of a single subvolcanic magma chamber.

(4) The major and trace element and Sr and Nd isotopic geochemistry of igneous rocks from Electric peak and Sepulcher Mountain cannot be explained through a closed-system, fractionation-dominated origin, as has been previously proposed.

(5) The compositional diversity of igneous rocks from Electric Peak and Sepulcher Mountain was produced through mixing of variably fractionated and contaminated mafic magmas with diverse composition silicic crustal melts and their differentiates.

(6) Mafic magmas are produced through the fractionation of clinopyroxene-rich, plagioclase-poor mineral assemblages from primary mantle-derived melts that have been contaminated by Archean crust.

(7) Silicic magmas are derived by partial melting of amphibolitic lower-crust leaving restites with variable proportions of plagioclase, amphibole, and pyroxene.

REFERENCES CITED

Anderson, J.L., and Smith, D.R., 1995, The effects of temperature and fO_2 on the Al-in-hornblende barometer: American Mineralogist, v. 80, p. 549-559.

Armstrong, R.J., 1988, Mesozoic and Early Cenozoic magmatic evolution of the Canadian Cordillera, *in* Clark, S.P., Burchfiel, B.C., and Suppe, J., eds., Processes in Continental Lithospheric Deformation: Boulder, Colorado Geological Society of America Special Paper 218, p. 55-91.

Beard, J.S., and Lofgren, G.E., 1991, Dehydration melting and water-saturated melting of basaltic and andesitic greenstones and amphibolites at 1, 3, and 6.9 kb: Journal of Petrology, v. 32, p. 365-401.

Bacon, C.R., 1986, Magmatic inclusions in silicic and intermediate volcanic rocks: Journal of Geophysical Research, v. 91, p. 6091-6112.

Benz, H.M., Chouet, B.A., Dawson, P.B., Lahr, J.C., Page, R.A., and Hole, J.A., 1996, Three-dimensional P and S wave velocity structure of Redoubt Volcano, Alaska: Journal of Geophysical Research, v. 99, p. 8111-8128.

Bird, P., 1984, Laramide crustal thickening event in the Rocky Mountain foreland and Great Plains: Tectonics, v. 3, p. 741-758.

Buddington, A.F., and Lindsley, D.H., 1964, Iron-titanium oxide minerals and synthetic equivalents: Journal of Petrology, v. 5, p. 310-357.

Burchfiel, B.C., Cowan, D.S., and Davis, G.A., 1992, Tectonic overview of the Cordilleran orogen in the western United States, *in* Burchfiel, B.C., Lipman, P.W., and Zoback, M.L., eds., The Cordilleran Orogen: conterminous U.S.: Boulder, Colorado, Geological Society of America, The Geology of North America, v. G-3, p. 407-480.

Burnham, C.W., 1979, Magmas and hydrothermal fluids, *in* Barnes, H.L., ed., Geochemistry of hydrothermal ore deposits, 2nd ed.: New York, Holt, Reinhart, and Winston, p. 71-136.

Cawthorne, R.G., 1976, Some chemical controls on igneous amphibole composition: Geochimica et Cosmochimica Acta, v. 40, p. 1319-1328.

Chadwick, R.A., 1970, Belts of eruptive centers in the Absaroka-Gallatin volcanic province, Wyoming-Montana: Geological Society of America Bulletin, v. 81, p. 267-274.

Chadwick, R.A., 1985, Overview of Cenozoic volcanism in the west-cetnral United States, *in* Kaplan, S.S., and Flores, R.M., eds., Rocky Mountain SEPM Cenozoic Paleogeography of the western United States Symposium III, p. 359-381.

Charmichael, I.S.E., and Ghiorso, M.S., 1986, Oxidation-reduction relations in basic magma: a case for homogenous equilibria: Earth and Planetary Science Letters, v. 78, p. 200-210.

Chayes, F., 1956, Petrographic modal analyses: New York, Wiley.

Clemens, J.D., and Vielzeuf, D., 1987, Constraints on melting and magma production in the crust: Earth and Planetary Science Letters, v. 86, p. 287-306.

Clemens, J.D., and Wall, V.J., 1981, Origin and crystallization of some peraluminous (S-type) granitic magmas: Canadian Mineralogist, v. 19, p. 111-132.

Coney, P.J., and Reynolds, S.R., 1977, Cordilleran Benioff Zones: Nature, v. 270, p. 403-406.

Cosca, M.A., Essene, E.J., and Bowman, J.R., 1991, Complete chemical analyses of metamorphic hornblendes: implications for normalizations, calculated H_2O activities, and thermobarometry: Contributions to Mineralogy and Petrology, v. 108, p. 316-328.

DePaolo, D.J., 1981, Trace element and isotopic effects of combined wallrock assimilation and fractional crystallization: Earth and Planetary Sciences, v. 53, p. 189-202.

Dickinson, W.R., and Hatherton, T., 1967, Andesitic volcanism and seismicity around the Pacific: Science, v. 157, p. 801-803.

Dodge, F.C.W., Papike, J.A., and Mays, R.E., 1968, Hornblendes from granitic rocks of the central Sierra Nevada Batholith, California: Journal of Petrology, v. 9, p. 378-410.

du Bray, E.A., and Harlan, S.S., 1996, The Eocene Big Timber stock, south-central Montana: Development of extensive compositional variation in an arc-related intrusion by side-wall crystallization and cumulate glomerocryst remixing: Geological Society of America Bulletin, v. 108, p. 1404-1424.

Dudás, F.O., 1991, Geochemistry of igneous rocks from the Crazy Mountains, Montana, and tectonic models for the Montana alkalic province: Journal of Geopyhsical Research, v. 96, p. 13261-13277.

Dudás, F.O., Carlson, R.W., and Eggler, D.H., 1987, Regional middle Proterozoic enrichment of the subcontinental mantle source of igneous rocks from central Montana: Journal of Geophysical Research, v. 96, p. 13261-13277.

Feeley, T.C., Cosca, M.A., and Lindsay, C.R., 2001, Petrogenesis and implications of cyptic hybrid magmas from Washburn Volcano, Absaroka Volcanic Province, U.S.A.: Journal of Petrology, *in press*.

Feeley, T.C., and Davidson, J.P., 1994, Petrology of calc-alkaline lavas at Volcán Ollagüe and the origin of compositional diversity at Central Andean stratovolcanoes: Journal of Petrology, v. 35, p. 1295-1340.

Foster, D.A., and Fanning, C.M., 1997, Geochronology of the northern Idaho Batholith and Bitterroot metamorphic core complex: magmatism preceding and contemporaneous with extension: Geological Society of America Bulletin, v. 109, p. 379-394.

Fraser, K.J., Hawkesworth, C.J., Erlank, A.J., Mitchell, R.H., Scott-Smith, B.H., 1985, Sr, Nd, and Pb isotope and minor element geochemistry of lamproites and kimberlites: Earth and Planetary Science Letters, v. 76, p. 57-70.

Fraser, G.D., Waldrop, H.A., and Hyden, H.J., 1969, Geology of the Gardiner area, Park ounty, Montana: U.S. Geological Survey Bulletin 1277, 118 p.

Fritz, W.J., 1982, Geology of the Lamar River Formation, northeastern Yellowstone National Park: Wyoming Geological Association 33rd Annual Field Conference Guidebook, p. 73-101.

Ghiorso, M.S., and Sack, R.O., 1991, Fe-Ti oxide geothermometry: thermodynamic formulation and the estimation of intensive variables in silicic magmas: Contributions to Mineralogy and Petrology, v. 108, p. 485-510.

Gill, J.B., 1981, Orogenic andesites and plate tectonics: New York, Springer, 390 p.

Hague, T.A., 1985, Gravity-spreading origin of the Heart Mountain allochthon, northwestern Wyoming: Geological Society of America Bulletin 96, p. 1440-1456.

Hague, T.A., 1993, The Heart Mountain detachment, northwestern Wyoming: 100 years of controversy, *in* Snoke A.W., Steidtmann, J.R., and Roberts, S.M., eds., Geology of Wyoming: Geological Survey of Wyoming Memoir v. 5, p. 530-571.

Halliday, A.N., Mahood, G.A., Holden, P., Metz, J.M., Dempster, T.J., and Davidson, J.P., 1989, Evidence for long residence times of rhyolitic magma in the Long Valley magmatic system: The isotopic record in precaldera lavas of Glass Mountain: Earth and Planetary Science Letters, v. 94, p. 274-290.

Hammarstrom, J.M., 1982, Chemical and mineralogical variability in the Pioneer batholith, southwest Montana: U.S. Geological Survey Open-File Report 82-148.

Hammarstrom, J.M., 1984, Microprobe analyses of hornblendes from 5 calc-alkalic intrusive complexes, with data tables for other calcic amphiboles and BASIC computer programs for data manipulation: U.S. Geological Survey Open-File Report 82-148.

Hammarstrom, J.M., Zen, E., 1986, Aluminum in hornblende: an empirical igneous geobarometer: American Mineralogist, v. 71, p. 1297-1313.

Harris, P.G., Kennedy, W.Q., and Scarfe, C.M., 1970, Volcanism versus plutonism – the effect of chemical composition, *in* Newall, G., and Rast, N., eds., Mechanism of Igneous Intrusions: Geological Journal, p. 187-200.

Hawthorne, F.C., 1981, Crystal chemistry of the amphiboles: Mineralogical Society of America Reviews in Mineralogy, v. 9A, p. 1-102.

Hearn, Jr., B.C., Dudâs, F.O., Eggler, D.H., Hyndman, D.W., O'Brien, H.E., McCallum, I.S., Irving, A.J., and Berg, R.B., 1989, Introduction: Montana high-potassium igneous province, *in* Hearn, Jr., B.C., ed., Montana high-potassium igneous province guidebook T346, 28th International Geological Congress: American Geophysical Union, p. 1-5.

Helz, R.T., 1982, Phase relations and compositions of amphiboles produced in studies of the melting behavior of rocks: Mineralogical Society of America Reviews in Mineralogy, v. 9B, p. 279-346.

Hibbard, M.J., 1995, Petrography to petrogenesis: Englewood Cliffs, New Jersey, Prentice Hall, 587 p.

Hiza, M.M., 1999, The geochemistry and geochronology of the Eocene Absaroka volcanic province, northern Wyoming and southwest Montana, U.S.A.: Ph.D. Thesis, Oregon State University, Corvallis, 243 p.

Holland, T., and Blundy, J., 1994, Non-ideal interactions in calcic amphiboles and their bearing on amphibole-plagioclase thermometry: Contributions to Mineralogy and Petrology, v. 116, p. 433-447.

Hollister, L.S., Grissom, G.C., Peters, E.K., Stowell, H.H., and Sisson, V.B., 1987, Confirmation of the empirical correlation of Al in hornblende with pressure of solidification of calc-alkaline plutons: American Mineralogist, v. 72, p. 231-239.

Hooper, P.R., Bailey, D.G., and McCarley Holder, G.A., 1995, Tertiary calc-alkaline magmatism associated with lithospheric extension in the Pacific Northwest: Journal of Geophysical Research, v. 100, p. 10303-10319.

Hopson, C.A., and Mattinson, J.M., 1994, Chelan migmatite complex, Washington: Field evidence for mafic magmatism, crustal anatexis, mixing and protodiapiric emplacement, *in* Geologic Field Trips of the Pacific Northwest, Chapter 2K: Boulder, Colorado, Geological Society of America.

Huang, W.L., and Wyllie, P.J., 1973, melting relation of muscovite-granite to 35 kbar as model for fusion of metamorphosed subducted oceanic sediments: Contributions to Mineralogy and Petrology, v. 42, p. 1-14.

Hutchinson, C.S., 1974, Laboratory handbook of petrographic techniques: New York, Wiley.

Iddings, J.P., 1891, The eruptive rocks of Electric Peak and Sepulcher Mountain, Yellowstone National Park: U.S. Geological Survey 12th Annual Report, Part 1, p. 569-664.

Iddings, J.P., 1899. The intrusive rocks of the Gallatin Mountains, Bunsen Peak, and Mount Everts, *in* The Geology of Yellowstone National park: U.S. Geological Survey Monograph 32, pt. 2. p.

Irving, A.J., and O'Brien, H.E., 1991, Isotopic and trace-element characteristics of late Cretaceous to Oligocene mafic volcanics from west-central Montana: Implications for Tertiary tectonics and magma genesis, *in* Baker, D.W., and Berg, R.B., eds., Guidebook of the central Montana alkalic province: geology, ore deposits and origin: Montana Bureau of Mines and Geology Special Publication 100, p. 140-142.

Irvine, T.N., and Baranger, W.R.A., 1971, A guide to the chemical classification of the common volcanic rocks: Canadian Journal of Earth Sciences, v. 8, p. 523-548.

Iyer, H.M., and Hitchcock, T., 1989, Upper mantle velocity structure in continental U.S. and Canada, *in* Pakiser, L.C., and Mooney, W.D., eds., Geophysical framework of the continetal United States: Boulder, Colorado, Geological Society of America Memoir 172, p. 249-284.

Janecke, S.U., 1992, Kinematics and timing of three superimposed extensional systems, east central Idaho: evidence for an Eocene tectonic transition: Tectonics, v. 11, p. 1121-1138.

Janecke, S.U., and Snee, L.W., 1993, Timing and episodicity of middle Eocene volcanism and onset of conglomerate deposition, Idaho: Journal of Geology, v. 101, p. 603-621.

Jenner, G.A., 1989, Eocene igneous activity and related metasomatic and hydrothermal events, Bear Lodge Mountains, Crook County, Wyoming, *in* Devils Tower-Black Hills Alkalic Igneous Rocks and General Geology; Field Trip Guidebook T131: Washington D.C., American Geophysical Union, p. 50-66.

Johnson, D.M., Hooper, P.R., and Conrey, R.M., 1999, XRF analysis of rocks and minerals for major and trace elements on a single low dilution Li-tetraborate fused bead: Advances in XRF Analysis, v. 41, p. 843-867.

Johnson, M.C., and Rutherford, M.J., 1989, Experimental calibration of the aluminum-in-hornblende geobarometer with application to Long Valley caldera (California) volcanic rocks: Geology, v. 17, p. 837-841.

Joswiak, D., 1992, Composition and evolution of the lower crust, central Montana: evidence from granulite facies xenoliths: M.S. Thesis, University of Washington, Seattle, 166 p.

Kenah, C., and Hollister, L.S., 1980, Anatexis in the Central Gneiss Complex, British Coloumbia, *in* M.P. Atherton, and C.D. Gribble, eds., Migmatitites, melting, and metamorphism: Nantwich, Shiva, p. 142-162.

Kuno, H., 1968, Differentiation of basalt magmas, *in* Hess, H.H., and Poldervaart, A., eds., Basalts: the Poldervaart treatise on rocks of basaltic composition, v. 2: New York, Interscience, p. 623-688.

LaPointe, D.D., 1977, Geology of a portion of the Eocene Sylvan Pass volcanic center, Absaroka Volcanic Range, Wyoming: M.S. Thesis, University of Montana, Missoula, 60 p.

Laul, J.C., 1979, Neutron activation analysis of geologic materials: Atomic Energy Reviews, v. 17, p. 603-695.

Leake, B.E., 1971, On aluminous and edenitic hornblendes: Mineralogical Magazine, v. 38, p. 389-407.

Leake, B.E., 1978, Nomenclature of amphiboles: Canadian Mineralogist, v. 16, p. 501-520.

Leeman, W.P., Smith, D.R., Hildreth, W., Palacz, Z., and Rogers, N., 1990, Compositional diversity of late Cenozoic basalts in a transect across the southern Washington Cascades: implications for subduction zone magmatism: Journal of Geophysical Research, v. 95, p. 19561-19582.

Lees, J.M., and Crosson, R.S., 1989, Tomographic inversion for three-dimensional velocity structure at Mount St. Helens using earthquake data: Journal of Geophysical Research, v. 94, p. 5715-5728.

Le Maitre, R.W., Bateman, P., Dudek, A., Keller, J., Lameyre Le Bas M.J., Sabine, P.A., Schmid, R., Sorensen, H., Streckeisen, A., Wooley, A.R., and Zanettin, B., 1989, A classification of igneous rocks and glossary of terms: Oxford, Blackwell.

Lichte, F.E., Meier, A.L., Crock, J.G., 1987, Determination of rare earth elements in geological materials by inductively coupled mass spectrometry: Analytical Chemistry, v. 59, p. 1150-1157.

Lindsay, C.R., Feeley, T.C., and Cosca, M.A., 2000, $^{40}Ar/^{39}Ar$ geochronology of Bunsen Peak, Yellowstone National Park: The last gasp of magmatism in the Absaroka volcanic province?: Geological Society of America Abstracts with Programs, v. 32, p. 30.

Lipman, P.W., 1992, Magmatism in the Cordilleran United States; Progress and problems, *in* Burchfiel, B.C., Lipman, P.W., and Zoback, M.L., eds., The Cordilleran Orogen: Conterminous U.S.: Boulder, Colorado, Geological Society of America, The Geology of North America, v. G-3, p. 481-514.

Lipman, P.W., and Glazner, A.F., 1991, Introduction to Middle Tertiary Cordilleran volcanism; Magma sources and relations to regional tectonics: Journal of Geophysical Research, v. 96, p. 13193-13199.

Lipman, P.W., Prostka, H.J., and Christiansen, R.L., 1972, Cenozoic volcanism and plate-tectonic evolution of the western United States; I. Early and middle Cenozoic: Philosophical Transactions of the Royal Society of London, v. 271, p. 217-248.

Love, J.D., Tschudy, R.H., and Obradovich, J.D., 1975, Dating a Laramide orogeny, northwestern Wyoming: U.S. Geological Society of America Professional Paper 975, 51 p.

Luedke, R.G., 1994, Map showing the distribution, composition, and age of early and middle Cenozoic volcanic centers in Idaho, Montana, west-central South Dakota, and Wyoming: United States Geological Survey Map I-2291-C.

MacDonald, R., Upton, B.G., Collerson, K.D., Hearn, B.C., and James, D., 1992, Potassic mafic lavas of the Bearpaw Mountains, Montana: Mineralogy, chemistry, and origin: Journal of Petrology, v. 33, p. 305-346.

McBirney, A.R., 1993. Igneous Petrology: Boston, Jones & Bartlett, 508 p.

McBirney, A.R., Taylor, H.P., and Armstrong, R.L., 1987, Paricutin re-examined: a classic example of crustal assimilation in calc-alkaline magma: Contributions to Mineralogy and Petrology, v. 95, p. 4-20.

McCallum, I.S., O'Brien, H.E., and Irving, A.J., 1989, Geology of the Highwood Mountains, Montana: a survey of magma types and sources, *in* Hearn, Jr., B.C., ed., Montana high-potassium igneous province guidebook T346, 28th International Geological Congress: American Geophysical Union, p. 23-35.

McKay, G.A., 1989, Partitioning of rare earth elements between major silicate minerals and basaltic melts, *in* Lipin, B.R., and McKay, G.A., eds., Geochemistry and Mineralogy of the Rare Earth Elements: Reviews in Mineralogy, v. 21, p. 45-78.

Meen, J.K., 1987a, Formation of shoshonites from calcalkaline basalt magmas: geochemical and experimental constraints from the type locality: Contributions to Mineralogy and Petrology, v. 97, p. 333-351.

Meen, J.K., 1987b, Sr, Nd, Pb isotopic compositions of Archean basement rocks, Boulder River region, Beartooth Mountains, Montana: Isochron West, v. 50, p. 13-24.

Meen, J.K., and Eggler, D.H., 1987, Petrology and geochemistry of the Cretaceous Independence volcanic suite, Absaroka Mountains, Montana: Clues to the composition of the Archean sub-Montanan mantle: Geological Society of America Bulletin, v. 98, p. 237-247.

Meen, J.K., and Eggler, D.H., 1989, Chemical and isotopic compositions of Absaroka granitoids, Southwestern Montana: evidence for deep-seated Archean amphibolite basement in the Beartooth Region: Contributions to Mineralogy and Petrology, v. 102, p. 462-477.

Montagne, J., and Chadwick, R.A., 1982, Cenozoic history of the Yellowstone Valley between Yellowstone Park and Livingston, Montana, *in* 33rd Annual Field Conference: Wyoming Geological Association, p. 31-51.

Morimoto, N., Fabries, J., Ferguson, A.k., Ginzburg, I.V., Ross, M., Seiefert, F.A., Zussman, J., Aoki, K., and Gottardi, G., 1988, Nomenclature of pyroxenes: American Mineralogist, v. 73, p. 1123-1133.

Morris, G.A., and Hooper, P.R., 1997, Petrogenesis of the Colville Igneous Complex, northeast Washington: Implications for Eocene tectonics in the northern U.S. Cordillera: Geology, v. 25, p. 831-834.

Morris, G.A., Larson, P.B., and Hooper, P.R., 2000, "Subduction style" magmatism in a non-subduction setting: The Colville igneous complex, NE Washington state, U.S.A.: Journal of Petrology, v. 41, n. 1, p. 43-67.

Mueller, P.A., Shuster, R.D., Graves, M.A., Wooden, J.L., and Bowes, D.R., 1988. Age and composition of a late Archean magmatic complex, Beartooth Mountains, Montana-Wyoming, *in* Lewis, S.E., and Berg, R.B., eds., Precambrian and Mesozoic plate margins: Montana, Idaho, and Wyoming, with field guides, for the 8th International Conference on Basement Tectonics: Montana Bureau of Mines and Geology Special Publication 96, p. 7-22.

Mueller, P.A., Wooden, J.L., and Bowes, D.R., 1983, Archean crustal evolution of the eastern Beartooth Mountains, Montana-Wyoming: Montana Bureau of Mines and Geology Special Publication 92, p. 9-21.

Mueller, P.A., Wooden, J.L., Schulz, K., and Bowes, D.R., 1983, Incompatible element rich andesitic amphibolites from the Archean of Montana and Wyoming: evidence for mantle metasomatism: Geology: v. 11, p. 203-206.

Nakamura, N., 1974, Determination of REE, Ba, Fe, Mg, Na and K in carbonaceous and ordinary chondrites: Geochimica et Cosmochima Acta v. 38, p. 757-775.

Naney, M.T., 1983, Phase equilibria of rock-forming ferromagnesian silicates in granitic systems: American Journal of Science v. 283, p. 993-1033.

Nelson, W.H., and Pierce, W.G., 1968, Wapiti Formation and Trout Peak Trachyandesite, northwestern Wyoming: U.S. Geological Society Bulletin 1254-H, 11 p.

Nelson, W.H., Prostka, H.J., Williams, F.E., Elliott, J.E., and Peterson, D.L., 1980, Geology and mineral resources of the North Absaroka Wilderness and vicinity, Park County, Wyoming: U.S. Geological Survey Bulletin 1447, 101 p.

Norman, M.C., 1988, Challis volcanics from subcontinental lithospheric mantle? Geological Society of America Abstracts with Programs, v. 20, p. 460.

Norman, M.C., and Mertzman, S.A., 1991, Petrogenesis of the Challis volcanics from central and southwestern Idaho: Trace element and isotopic evidence: Journal of Geophysical Research, v. 96, p. 13279-13293.

Novak, S.W., and Bacon, C.R., 1986, Pliocene volcanic rocks of the Coso Range, Inyo County, California: U.S. Geological Survey Professional Paper 1383.

O'Brien, H.E., Irving, A.J., and McCallum, S., 1991, Eocene potassic magmatism in the Highwood Mountains, Montana: Petrology, geochemistry, and tectonic implications: Journal of Geophysical Research, v. 96, p. 13237-13260.

Parsons, W.H., 1969, Types of intrusives in the Absaroka volcanic province: Geological Society of America Special Paper 121, p. 619-620.

Peacock, M.A., 1931, A classification of igneous rocks: Journal of Geology, v. 39, p. 54-67.

Pearce, J.A., and Norry, M.J., 1979, Petrogenetic implications of Ti, Zr, Y, and Nb variations in volcanic rocks: Contributions to Mineralogy and Petrology, v. 69, p. 33-47.

Perfit, M.R., Gust, D.A., Bence, A.E., Arculus, R.J., and Taylor, S.R., 1981, Chemical characteristics of island-arc basalts: implications for their mantle sources: Chemical Geology, v. 30, p. 227-256.

Pierce, K.L., Adams, K.D., and Sturchio, N.C, 1991, Geologic setting of the Corwin Springs known geothermal resources area-Mammoth Hot Springs area in and adjacent to Yellowstone National Park, *in* Sorey, M.L., ed., Effects of potential geothermal development in the Corwin Springs known geothermal resources area, Montana, on the thermal features of Yellowstone National Park: U.S. Geological Survey Water-Resources Investigations Report 91-4052, p. C1-C35.

Power, J.A., Villaseñor, A., and Benz, H.M., 1998, Seismic image of the Mount Spur Magmatic system: Bulletin of Volcanology, v. 60, p. 27-37.

Prodehl, C., and Lipman, P.W., 1989, Crustal structure of the Rocky Mountain Region, *in* Pakiser, L.C., and Mooney, W.D., eds., Geophysical framework of the continental United States: Boulder, Colorado, Geological Society of America Memoir 172, p. 249-284.

Reiners, P.W., Nelson, B.K., and Ghiorso, M.S., 1995, Assimilation of felsic crust by basaltic magmas: thermal limits and extents of crustal contamination of mantle-derived magmas: Geology, v. 23, p. 563-566.

Rollinson, H.R., 1993, Using geochemical data: evaluation, presentations, and interpretation: London, Longman Group, 352 p.

Rubel, D.H., 1971, Independence volcano: a major Eocene eruptive center, northern Absaroka volcanic province: Geological Society of America Bulletin, v. 82, p. 2473-2494.

Ruppel, E.T., 1972, Geology of pre-Tertiary rocks in the northern part of Yellowstone National Park, Wyoming: U.S. Geological Survey Professional Paper 729-A, 66 p.

Rutter, M.J., and Wyllie, P.J., 1987, Melting of tonalite and the origin of crustal granites: EOS Transactions of the American Geophysical Union v. 68, p. 441.

Schmidt, C.J., and Garihan, J.M., 1983, Laramide tectonic development of the Rocky Mountain foreland of southwestern Montana, *in* Lowell, J.D., ed., Rocky Mountain foreland basins and uplifts: Denver, Colorado, Rocky Mountain Association of Geologists, p. 271-294.

Schmidt, M.W., 1992, Amphibole composition in tonalite as a function of pressure: an experimental calibration of the Al-in-hornblende barometer: Contributions to Mineralogy and Petrology, v. 110, p. 204-310.

Schultz, C.H., 1962, Petrology of Mt. Washburn, Yellowstone National Park, Wyoming: Ph.D. Thesis, Ohio State University, Columbus, p. 266.

Singer, B.S., Thompson, R.A., Dungan, M.A., Feeley, T.C., Nelson, S.T., Pickens, J.C., Brown, L.L., Wulff, A.W., Davidson, J.P., and Metzger, J., 1997, Volcanism and erosion during the past 930 k.y. at the Tatara-San Pedro complex, Chilean Andes: Geological Society of America Bulletin, v. 109, p. 127-142.

Sisson, T.W., and Grove, T.L., 1993, Experimental investigations of the role of H_2O in calc-alkaline differentiation and subduction zone magmatism: Contributions to Mineralogy and Petrology, v. 113, p. 143-166.

Smedes, H.W., and Prostka, H.J., 1972, Stratigraphic framework of the Absaroka Volcanic Supergroup in the Yellowstone National Park region: U.S. Geological Survey Professional Paper 729-C, 33 p.

Steven, T.A., Smedes, H.W., Prostka, H.J., Lipman, P.W., and Cristiansen, R.L., 1972, Upper Cretaceous and Cenozoic igneous rocks in the Rocky Mountain region, *in* Geologic atlas of the Rocky Mountain region: Rocky Mountain Asssociation of Geologists, p. 229-232.

Streckeisen, A., 1979, Classification and nomenclature of volcanic rocks, lamprophyres, carbonatites, and melilitic rocks, recommendations and suggestions of the IUGS Subcommission on the Systematics of Igneous Rocks: Geology, v. 7, p. 331-335.

Sundell, K.A., 1985, The Castle Rocks chaos: a gigantic Eocene landslide-debris flow in the southeastern Absaroka Range, Bighorn Basin, Wyoming: American Association of Petroleum Geologists Bulletin, v. 67, p. 1357-1358.

Sundell, K.A., 1993, A geologic overview of the Absaroka volcanic province, *in* Snoke, A.W., Steidmann, J.R., and Roberts, S.M., eds., Geology of Wyoming: Geological Survey of Wyoming Memoir No. 5, p. 480-506.

Sundell, K.A., and Eaton, J.G., 1982, Stratigraphic relations within the southeastern Absaroka volcanic sequence, northwestern Wyoming: Wyoming Geological Association 33rd Annual Field Conference Guidebook, p. 65-71.

Tatsumi, Y., and Eggins, S., 1995, Subduction Zone Magmatism: Cambridge, Massachusetts, Blackwell Science, 211 p.

Thompson, R.N., 1982, British Tertiary volcanic province: Scottish Journal of Geology, v. 18, p. 49-107.

Tscuchiyama, A., 1985, Dissolution kinetics of plagioclase in the melt of the system diopside-albite-anorthite, and origin of dusty plagioclase in andesites: Contributions to Mineralogy and Petrology, v. 89, p. 1-16.

Urbanczyk, K.M., and Lilligren, S.P., 1990, Geology and geochemistry of the eastern Clarno Formation, Grant County, Oregon, U.S.A., *in* Vancouver '99; Geological Association of Canada, Mineralogical Association of Canada, annual meeting; program with abstracts: Waterloo, Ontario, Geological Association of Canada, v. 15, p. 133.

U.S. Geological Survey, 1972, Geologic Map of Yellowstone National Park: U.S. Geological Survey Map I-711.

Vance, J.A., 1965, Zoning in igneous plagioclase: patchy zoning: Journal of Geology, v. 73, p. 637-651.

Vance, J.A., 1988, New fission track and K-Ar ages from the Clarno Formation, Challis age volcanic rocks in north central Oregon: Geological Society of America Abstracts with Programs, v. 20, p. 473.

Ward, P.L, 1995, Subduction cycles under western North America during the Mesozoic and Cenozoic eras, *in* Miller, D.M., and Busby, C., eds., Jurassic magmatism and tectonics of the North American Cordillera: Boulder, Colorado. Geological Society of America Special Paper 299, p. 1-45.

Wilson, M., 1989, Igneous petrogenesis: a global tectonic approach: London, Unwin Hyman, 466 p.

Wilson, W.H., 1964, The Kirwin mineralized area, Park County Wyoming: Wyoming Geological Survey Preliminary Report, n. 2, 12 p.

Winterfield, G.F., and Conrad, J.B., 1983, Laramide tectonics and deposition, Washakie Range and northwestern Wind River Basin, Wyoming, *in* Lowell, J.D., ed., Rocky Mountain foreland basins and uplifts: Denver, Colorado, Rocky Mountain Association of Geologists, p. 137-148.

Wooden, J.L., and Mueller, P.A., 1988, Pb, Sr, and Nd isotopic compositions of a suite of Late Archean, igneous rocks, eastern Beartooth Mountains: implications for crust-mantle evolution: Earth and Planetary Science Letters, v. 87, p. 59-72.

Wooden, J.L., Mueller, P.A., Hunt, D.K., and Bowes, D.R., 1982, Geochemistry and Rb-Sr geochronology of Archean rocks from the interior of the southeastern Beartooth Mountains, Montana and Wyoming: *in* Mueller, P.A., and Wooden, J.L., eds., Precambrian geology of the Beartooth Mountains, Montana and Wyoming, Montana Bureau of Mines and Geology Special Publication 84, p. 45-55.

Wust, S.L., 1986, Extensional deformation with a northwest vergence, Pioneer core complex, central Idaho: Geology, v. 14, p. 712-714.

Yuretich, R.F., 1984, Yellowstone fossil forests: new evidence for burial in place: Geology, v. 12, p. 1159-1162.

APPENDICES

APPENDIX A

SAMPLE LOCATIONS AND PETROGRAPHIC DESCRIPTIONS

SM9701: Amphibole-andesite clast; UTM: 4981870N, 12518530E; sampled from autobreccia northwest of summit of Sepulcher Mountain; fine-to-medium-grained (0.3-2.0 mm), hypocrystalline, porphyritic, seriate; euhedral-to-subhedral phenocrysts of plagioclase feldspar (23%), some are partially resorbed spongy cellular laths, sparse euhedral orthopyroxene glomerocrysts (0.4%), euhedral-to-subhedral amphibole (5.5%), opaque minerals (3.0%), and a fine-grained groundmass.

SM9702: Dacite flow; UTM: 4981600N, 12518360E; sampled from platy outcrop southwest of summit of Sepulcher Mountain; hypocrystalline, porphyritic, fine-to-medium grained; phenocrysts of plagioclase feldspar (22.3%), clinopyroxene (2.2%), amphibole (1.9%), opaque minerals (1.5%), and orthopyroxene (0.4%).

SM9703: Orthopyroxene-amphibole-bearing dacite flow; UTM: 4981480N, 12518260E; sampled from platy outcrop southwest of summit of Sepulcher Mountain; fine-to-medium-grained (0.3-2.5 mm), hypocrystalline, porphyritic, seriate, hyalophitic; euhedral-to-anhedral phenocrysts of plagioclase feldspar (18%), some are spongy cellular laths, rare clinopyroxene (0.5%), orthopyroxene (1%), sparse oxidized amphibole (1.1%), and opaque minerals (2.4%). Groundmass is plagioclase feldspar, clinopyroxene, and opaque minerals.

SM9704: Two pyroxene-andesite flow; UTM: 4980520N, 12518340E; sampled from dark gray-black platy outcrop on south ridge of Sepulcher Mountain; fine-to-medium-grained (<1.5 mm), hypocrystalline, porphyritic, trachytic; phenocrysts of plagioclase feldspar (4.6%), clinopyroxene (4.7%), orthopyroxene (3.5%), and sparse amphibole, opaque minerals (0.9%). Groundmass is plagioclase feldspar, clinopyroxene, orthopyroxene, and opaque minerals. Amphibole grains are anhedral with thick, oxidized rims. Larger plagioclase grains are anhedral with spongy cellular cores.

SM9705: Amphibole-andesite flow; UTM: 4980740N, 12518380E; sampled from south ridge of Sepulcher Mountain; fine-to-medium-grained (<1.5 mm), hypocrystalline, porphyritic, trachytic; phenocrysts of plagioclase feldspar (9.3%), amphibole with oxidized rims (9.5%); glomerocrysts of orthopyroxene (0.3%) clinopyroxene (0.3%), and opaque minerals (1.6%). Groundmass consists of plagioclase feldspar, amphibole, and opaque minerals.

SM9706: Biotite-amphibole-rhyolite dome; UTM: 4985240N, 12519910E; sampled from large cliff just west of Rainbow Lake; fine-to-medium-grained (0.3-2.0 mm), holocrystalline, porphyritic; phenocrysts of plagioclase feldspar (24.2%), amphibole replaced by biotite (3.9%), biotite (3.2%), quartz (0.8%), and opaque minerals (0.3%). Groundmass is plagioclase feldspar, biotite, quartz, amphibole, and opaque minerals. Rhyolite is host to metasedimentary, hornblendite, and quenched magmatic inclusions.

SM9706.1i: Amphibole-trachyandesite quenched magmatic inclusion; UTM: 4982580N, 12513280E; sampled from large cliff just west of Rainbow Lake; holocrystalline with microcrystalline groundmass, fine-to-medium-grained, seriate, ophiomottled; crystals of plagioclase (52.6%) many contain melt inclusions, acicular amphibole (46.5%), and opaque minerals (0.9%).

SM9706.2i: Amphibole-dacite magmatic inclusion; UTM: 4982580N, 12513280E; sampled from large cliff just west of Rainbow Lake; holocrystalline, medium-grained, porphyritic, crystals of plagioclase (48.6%), amphibole (51.1%), and opaque minerals (0.3%).

SM9709: Clinopyroxene-andesite flow; UTM: 4983910N, 12518450E; sampled from 0.75 m thick black lava flow near base of north ridge of Sepulcher Mountain; fine-grained (0.3-1.0 mm), hypocrystalline, porphyritic, seriate, slightly vesicular; phenocrysts plagioclase feldspar(19.1%), clinopyroxene (6.4%), olivine altered to iddingsite (1.3%), and opaque minerals (3.4%). Glomerocrysts of clinopyroxene, with minor plagioclase and trace orthopyroxene. Groundmass consists of plagioclase feldspar, clinopyroxene, and opaque minerals.

SM9712: Olivine-clinopyroxene-basaltic andesite flow; UTM: 4983410N, 12518280E; sampled from a thin flow on north ridge of Sepulcher Mountain; fine-to-medium-grained (0.3-1.25 mm), hypocrystalline, porphyritic; phenocrysts of plagioclase feldspar (12.1%), clinopyroxene (8.1%), olivine replaced by iddingsite and serpentine (3.9%), and opaque minerals (0.2%). Groundmass is plagioclase feldspar > clinopyroxene > opaque minerals.

SM9713: Two pyroxene-andesite flow; UTM: 4977480N, 12518020E; sampled from small eruptive center south of Glen Creek; fine-to-medium-grained (0.3-1.2 mm), hypocrystalline, porphyritic, sub-trachytic, vitrophyric; phenocrysts of plagioclase feldspar (26.9%), orthopyroxene (3.6%), clinopyroxene (2.8%), rare heavily oxidized anhedral amphibole (0.1%) and opaque minerals (2.3%), set in glass with sparse microphenocrysts of plagioclase feldspar, clinopyroxene, and opaque minerals. Plagioclase grains exhibit spongy cellular cores, and some grains have thin, sieved rings which are mantled by non-sieved, euhedral rims. Clinopyroxene grains contain spongy cellular cores and are mantled by euhedral rims.

SM9715: Amphibole-bearing, clinopyroxene-orthopyroxene-andesite flow; UTM: 4978460N, 12517720E; sampled from small eruptive center south of Glen Creek; fine-to-medium-grained (0.3-2.0 mm), hypocrystalline, porphyritic; phenocrysts of plagioclase feldspar (17.7%), orthopyroxene (5.8%), clinopyroxene (4.6%), amphibole with clinopyroxene coronas (1.4%), and opaque minerals (0.6%). Glomerocrysts of orthopyroxene and clinopyroxene. Groundmass consists of plagioclase feldspar, orthopyroxene, clinopyroxene, and opaque minerals.

S9716: Two pyroxene-andesite flow; UTM: 4978560N, 12517550E; sampled from small eruptive center south of Glen Creek; fine-to-medium-grained (0.5-1.75 mm), porphyritic, subtrachytic; phenocrysts of plagioclase feldspar (13.4%), orthopyroxene (6.4%), clinopyroxene (5.9%), opaque minerals (0.1%), and rare oxidized amphibole. Rounded glomerocrysts of clinopyroxene > orthopyroxene. Microcrystalline groundmass of plagioclase feldspar > opaque minerals.

SM9717: Clinopyroxene-bearing andesite clast; UTM: 4978610N, 12517490E; sampled from heterolithologic clast-supported vent agglomerate near small eruptive center south of Glen Creek; hypocrystalline, fine-grained (0.3-0.75 mm), porphyritic, seriate, subtrachytic; phenocrysts of plagioclase feldspar (13%), clinopyroxene (1.3%), rare orthopyroxene (0.3%), and opaque minerals. Groundmass is microcrystalline and consists of plagioclase feldspar > clinopyroxene > opaque minerals.

SM9718: Two pyroxene-andesite clast; UTM: 4982380N, 12518780E; sampled from heterolithologic clast-supported breccia on south ridge of Sepulcher Mountain; fine-to-medium-grained (0.3-1.5 mm), porphyritic, hypocrystalline; phenocrysts of plagioclase feldspar (21.8%), rounded glomerocrysts of clinopyroxene (7.3%), orthopyroxene (4.5%), and subordinate plagioclase feldspar, opaque minerals (0.3%). Microcrystalline groundmass consists of plagioclase feldspar > opaque minerals. Inclusions (?) of orthopyroxene > clinopyroxene > opaque minerals are rare.

SM9719: Clinopyroxene-bearing andesite flow; UTM: 4981160N, 12518580E; sampled from flow on south ridge of Sepulcher Mountain; fine-to-medium-grained, hypocrystalline, porphyritic, phenocrysts of plagioclase feldspar (22.2%), clinopyroxene (1.4%), orthopyroxene (0.5%), and opaque minerals (1.8%). Microcrystalline groundmass consists of plagioclase feldspar > opaque minerals > clinopyroxene > orthopyroxene.

SM9720: Two pyroxene-andesite dike; UTM: 4981960N, 12518820E; sampled from 3.5 m wide dike (122°,69° SW) northeast of summit of Sepulcher Mountain; fine-to-medium-grained, porphyritic, hypocrystalline; phenocrysts of plagioclase feldspar (14.1%), clinopyroxene (8.2%), orthopyroxene (3.1%), and opaque minerals (1.0%). Glomerocrysts of orthopyroxene > clinopyroxene. Microcrystalline groundmass of plagioclase feldspar > opaque minerals.

SM9721: Olivine-orthopyroxene-bearing clinopyroxene-andesite dike; UTM: 4982070N, 12518460E; sampled from chilled margin of dike (115°,10° SW) northwest of summit of Sepulcher Mountain; fine-to-medium-grained, porphyritic, hypocrystalline, sub-trachytic; phenocrysts of plagioclase feldspar (14.4%), clinopyroxene (8%), orthopyroxene (1.9%), olivine replaced by iddingsite (1.4%) and opaque minerals(0.6%). Groundmass is microcrystalline and trachytic with plagioclase feldspar > opaque minerals.

SM9722: Orthopyroxene-bearing clinopyroxene-andesite flow; UTM: 4982110N, 12518400E; sampled on north ridge of Sepulcher Mountain; fine-to-medium-grained, porphyritic, hypocrystalline; phenocrysts of plagioclase feldspar, some sieve textured (31.3%), clinopyroxene (4.7%), orthopyroxene (0.9%), and opaque minerals (1.5%). Microcrystalline groundmass of plagioclase feldspar > opaque minerals.

SM9723: Orthopyroxene-bearing clinopyroxene-andesite dike; UTM: 4982320N, 12518250E; sampled from 1.5 m wide dike on north ridge of Sepulcher Mountain; fine-grained, porphyritic, hypocrystalline; phenocrysts of plagioclase feldspar (12.6%), clinopyroxene (8.3%), orthopyroxene (1.3%), and opaque minerals (0.2%). Sparse glomerocrysts of clinopyroxene > orthopyroxene ± plagioclase feldspar. Microcrystalline groundmass of plagioclase feldspar > opaque minerals.

SM9724: Amphibole-dacite flow; UTM: 4982440N 12518050E; sampled from 20-25 m thick flow on north ridge of Sepulcher Mountain; fine-to-very-coarse-grained, porphyritic, hypocrystalline, seriate, slightly vesicular; phenocrysts of euhedral plagioclase feldspar (27.5%), euhedral amphibole (0.15-30 mm) (3.7%), clinopyroxene (0.6%), orthopyroxene (0.1%), and opaque minerals (1.2%). Pyroxene phenocrysts are reacting to amphibole and biotite + opaque minerals. Microcrystalline groundmass of plagioclase feldspar > opaque minerals > pyroxenes.

SM9725: Amphibole-andesite flow; UTM: 4982600N, 12517980E; sampled from lava flow on north ridge of Sepulcher Mountain; fine-to-medium-grained, porphyritic, hypocrystalline, slightly vesicular, subtrachytic, seriate; euhedral phenocrysts of plagioclase feldspar, larger grains have distinctly sieved cores and unsieved rims (30.4%), sub-to-euhedral amphibole (2.4%), sub-to-euhedral orthopyroxene (0.4%), subhedral clinopyroxene (0.3%), and opaque minerals (1.1%). Glomerocrysts of clinopyroxene and orthopyroxene. Microcrystalline groundmass of plagioclase feldspar > opaque minerals >> rare orthopyroxene.

SM9726: Two pyroxene-andesite flow; UTM: 4982730N, 12517980E; sampled from chilled base of 2 m thick vertically jointed flow on north ridge of Sepulcher Mountain; fine-grained, porphyritic, hypocrystalline, slightly vesicular, seriate; phenocrysts of euhedral plagioclase feldspar (12.3%), sub-to-euhedral clinopyroxene (7.7%), euhedral orthopyroxene (2.8%), and opaque minerals (0.7%). Glomerocrysts of clinopyroxene > plagioclase feldspar > orthopyroxene, also orthopyroxene altering to uralite with a corona of orthopyroxene > plagioclase feldspar > opaque minerals, and olivine reacting to iddingsite.

SM9727: Orthopyroxene-clinopyroxene-andesite flow; UTM: 4982810N, 12517990E; sampled from a 25-30 thick flow on north ridge of Sepulcher Mountain; fine-to-medium-grained, porphyritic, hypocrystalline, seriate; phenocrysts of sub-to-euhedral plagioclase (10.6%), subhedral clinopyroxene (8.2%), euhedral orthopyroxene (2.7%), and opaque minerals (1.2%). Glomerocrysts of plagioclase and opaque minerals. Microcrystalline groundmass consisting of plagioclase > orthopyroxene > clinopyroxene > opaque minerals.

SM9730: Biotite-amphibole-dacite flow; UTM: 4986620N, 12517280E; sampled from a ~20 m thick flow on north spur of Sepulcher Mountain; fine-to-medium-grained, porphyritic, holocrystalline; phenocrysts of euhedral plagioclase feldspar (24.9%), sub-to-euhedral amphibole (7.7%), subhedral biotite (2.2%), and opaque minerals (0.7%). Abundant glomerocrysts with same phenocrysts, microcrystalline groundmass of plagioclase feldspar > biotite > opaque minerals.

SM9731: Biotite-amphibole-dacite flow; UTM: 4986340N, 12516800E; sampled from flow on "hill 7205", on north spur of Sepulcher Mountain; fine-to-medium-grained, porphyritic, hypocrystalline; phenocrysts of sub-to-euhedral plagioclase feldpsar (26.5%), some with a spongy cellular texture, an-to-euhedral amphibole (3.7%), sometimes pitted, sub-to-euhedral biotite (2.5%), and opaque minerals (1.0%). Groundmass is microcrystalline and is partially devitrified.

SM9732: Biotite-amphibole-dacite dike; UTM: 4986N, 12516E; sampled from dike south of "hill 7205", on north spur of Sepulcher Mountain; fine-to-medium-grained, porphyritic, hypocrystalline; phenocrysts of euhedral plagioclase feldspar (29.1%), euhedral amphibole (3.7%), sub-to-euhedral biotite (3.3%), and opaque minerals (2.4%). Sparse glomerocrysts of plagioclase feldspar > biotite. Groundmass is microcrystalline.

SM9733: Biotite-bearing amphibole-dacite flow; UTM: 4986120N, 12517990E; sampled from northeast stream drainage of "hill 7962" on north spur of Sepulcher Mountain; fine-to-medium-grained, porphyritic, hypocrystalline; phenocrysts of euhedral plagioclase feldspar (31.1%), some have resorbtion rings preserved and overgrown, sub-to-euhedral amphibole (6.5%), subhedral biotite(1.6%), opaque minerals (1.6%). Groundmass consists of plagioclase feldspar >> biotite. Sparse glomerocrysts of plagioclase feldspar + amphibole + clinopyroxene + orthopyroxene + opaque minerals.

SM9734: Biotite-amphibole-dacite flow; UTM: 4985990N, 12517680E; sampled from >80 m thick flow on northeast stream drainage of "hill 7962" on north spur of Sepulcher Mountain; fine-to-medium grained, porphyritic, hypocrystalline; phenocrysts of predominately euhedral plagioclase feldspar (24.9%), sub-to-euhedral amphibole (6.8%), sub-to-euhedral biotite (2.0%), opaque minerals (1.5%), and rare quartz (0.1%). Sparse glomerocrysts of amphibole. Groundmass is plagioclase feldspar + opaque minerals + quartz.

SM9735: Biotite-amphibole-dacite flow; UTM: 4985770N, 12517350E; sampled from thin, crudely columnar jointed flow on northeast stream drainage of "hill 7962" on north spur of Sepulcher Mountain; fine-to-medium grained, porphyritic, hypocrystalline; phenocrysts of euhedral plagioclase feldspar (27.3%), subhedral amphibole (3.7%), subhedral biotite (2.0%), and opaque minerals (1.7%). Sparse glomerocrysts of amphibole rimmed by plagioclase feldspar and opaque minerals. Groundmass consists of plagioclase feldspar and opaque minerals.

SM9736: Clinopyroxene-andesite flow; UTM: 4985700N, 12517270E; sampled from 2-3 m thick flow on northeast stream drainage of "hill 7962" on north spur of Sepulcher Mountain; fine-grained, porphyritic, hypocrystalline, trachytic, and seriate; phenocrysts of sub-to-euhdral, swallow-tailed plagioclase feldspar (4.1%), an-to-subhedral clinopyroxene (3.5%), usually in small clots with totally rounded edges, sparse an-to-subhedral orthopyroxene (0.3%), and opaque minerals (0.1%). Groundmass of plagioclase feldspar and opaque minerals.

SM9737: Olivine-clinopyroxene-basaltic andesite flow; UTM: 4985560N, 12517050E; sampled from flow on northeast stream drainage of "hill 7962" on north spur of Sepulcher Mountain; fine-to-medium grained, porphyritic, hypocrystalline, and seriate; phenocrysts of sub-to-euhedral plagioclase feldspar (9.7%), predominately sub-to-euhedral clinopyroxene (5.7%), some containing melt inclusions, predominately an-to-subhedral, pervasively serpentinized olivine, rare euhedral orthopyroxene (0.6%), and opaque minerals (0.1%). Groundmass consists of plagioclase feldspar and opaque minerals.

SM9738: Amphibole-andesite dike; UTM: 4985560N, 12516990E; sampled from thin (~1.2 m wide) eastern most dike northeast of summit of "hill 7962" on north spur of Sepulcher Mountain; fine-to-medium grained, porphyritic, hypocrystalline, with a sub-trachytic groundmass; phenocrysts of predominately euhedral plagioclase feldspar (15.8%), euhedral amphibole (6.2%), sparse subhedral orthopyroxene (0.3%), and opaque minerals (1.7%). Groundmass of swallow-tailed plagioclase feldspar and opaque minerals.

SM9740: Biotite-amphibole dacite; UTM: 4985510N, 12516950E; sampled from second western most dike near summit of "hill 7962" on north spur of Sepulcher Mountain; fine-to-medium grained, porphyritic-aphanitic, hypocrystalline; phenocrysts of euhedral plagioclase feldspar (31.1%), some are sieved and filled with melt inclusions, sub-to-euhedral amphibole (6.5%), some sieved and filled with plagioclase feldspar + opaque minerals, sub-to-euhedral biotite (4.2%), and opaque minerals (1.7%). Glomerocrysts of amphibole + opaque minerals are common. Groundmass consists of plagioclase feldspar, amphibole(?), and opaque minerals.

TLC9701: Biotite-amphibole dacite flow; UTM: 4986630N, 12517410E; sampled from east flank of "hill 7205" on north spur of Sepulcher Mountain; fine-to-medium grained, porphyritic, hypocrystalline, trachytic; phenocrysts of plagioclase feldspar (13.5%), some have boxy-cellular cores resorbtion "ring" of spongy-cellular feldspar, amphibole (6.8%), biotite (3.9%), and opaque minerals (0.9%). Glomerocrysts of opaque minerals + amphibole are common.

SM9810: Orthopyroxene-bearing, amphibole-clinopyroxene dacite dike; UTM: 4983070N, 12516900E; sampled on saddle north of Sepulcher Mountain which straddles the Montana - Wyoming state border; fine-grained, porphyritic, hypocrystalline, sub-trachytic, glomeroporphyritic; phenocrysts of plagioclase feldspar (7.4%), clinopyroxene (4.3%), amphibole (2.1%), orthopyroxene (1.1%), and opaque minerals (0.2%) set in groundmass of microcrystalline feldspar and opaque minerals and glass. Glomerocrysts are composed of orthopyroxene + clinopyroxene + plagioclase feldspar + opaque minerals +/- amphibole. Magmatic inclusions of plagioclase, amphibole, and opaque minerals are sparse. Xenocrystic amphibole might be present, amphibole has rounded, heavily oxidized rims.

SM9814: Orthopyroxene-amphibole dacite dike; UTM: 4983700N, 12516010E; sampled just west of "hill 8542" which is northeast of Sepulcher Mountain; fine-grained, porphyritic, seriate, trachytic, compositionally banded, quenched-inclusion bearing; phenocrysts of subhedral plagioclase feldspar (16.4%), amphibole (4.9%) with disequilibrium textures (eustructural with poor structural integrity, replaced by biotite and opaque minerals) , euhedral orthopyroxene (4.1%), and opaque minerals (1.4%) in pristine, crystal-free, glass; inclusions are holocrystalline with phenocrysts of plagioclase feldspar, amphibole, and opaque minerals set in a microcrystalline groundmass of plagioclase feldspar and opaque minerals, plagioclase feldspar grains are euhedral and commonly have notable compositional zoning and prominent resorbtion surfaces, plagioclase feldspar cores typically are spongy-cellular, amphibole commonly has pitted cores; inclusions are bounded by rime of brown glass containing crystals of plagioclase feldspar and amphibole; some inclusions are disaggregated and strung out in distinct compositional bands.

SM9825: Orthopyroxene-clinopyroxene andesite dike; UTM: 4982410N, 12511030E; sampled from 0.5 m wide dike trending 95°, 90 just NW of summit of Sepulcher Mountain; fine-to-medium grained, porphyritic, hypocrystalline, sub-trachytic; phenocrysts of euhedral, occasionally sieved plagioclase feldspar (17.3%), sub-to-euhedral clinopyroxene (8.1%), sparse, euhedral orthopyroxene (2.1%), opaque minerals (0.9%), rare olivine altered to iddingsite (0.6%), and very rare, possibly xenocrystic, fresh amphibole with rounded anhedral crystal faces. Common glomerocrysts of clinopyroxene ± orthopyroxene + plagioclase feldspar + opaque minerals ± olivine as well as glomerocrysts of clinopyroxene ± orthopyroxene. Groundmass consists of plagioclase feldspar and opaque minerals.

SM9826: Orthopyroxene-clinopyroxene andesite flow; UTM: 4982910N, 1251820E; sampled from 2 m thick flow on north ridge of Sepulcher Mountain; fine-to-medium grained, porphyritic, hypocrystalline; phenocrysts of euhedral plagioclase feldspar (13%), some having sieved cores overgrown with unsieved rims with rounded anhedral faces, sub-to-euhedral clinopyroxene (9.3%), predominately euhedral orthopyroxene (2.2%), opaque minerals (0.6%), and extremely rare amphibole. Glomerocrysts of clinopyroxene ± orthopyroxene ± plagioclase feldspar ± opaque minerals are quite common. Groundmass consists of plagioclase feldspar and opaque minerals.

SM9827: Orthopyroxene-bearing amphibole-clinopyroxene basaltic andesite flow; UTM: 4982940N, 12518200E; sampled from 2 m thick flow on north ridge of Sepulcher Mountain; fine-to-medium grained, porphyritic, hypocrystalline, phenocrysts of euhedral plagioclase feldspar (15.7%), sub-to-euhedral clinopyroxene (6.1%), anhedral amphibole, overgrown by a fresh rim of clinopyroxene + opaque minerals (5.7%), predominately euhedral orthopyroxene (1.8%), serpentinized olivine

SM9828: Clinopyroxene-olivine basaltic andesite clast; UTM: 4983340N, 12518200E; sampled from massive heterolithologic clast supported breccia on north ridge of Sepulcher Mountain; fine-grained, porphyritic, hypocrystalline, glomeroporphyritic; phenocrysts of predominately euhedral plagioclase feldspar (14.5%), both embayed and skeletal anhedral olivine (6.8%), glomerocrysts of sub-to-euhedral clinopyroxene (6.0%) and predominately euhedral orthopyroxene (5.0%), and opaque minerals (0.1%). Plagioclase feldspars commonly contain melt inclusions, olivine altered to iddingsite.

EP9711: Amphibole granodiorite (*modified TAS*) micro-porphyry dike; UTM: 4983310N, 12512900E; sampled from dike which cuts the summit of Electric Peak; fine-to-medium grained, porphyritic-aphanitic, holocrystalline with microcrystalline groundmass, seriate; phenocrysts of plagioclase feldspar (27.7%), amphibole (3.9%), biotite (0.9%), sparse opaque minerals, and scarce zircon. Amphibole is eustructural with poor integrity, biotite is heavily oxidized. Whole rock is pervasively sericitized.

EP9712*: Biotite-bearing quartz monzodiorite (*I.U.G.S.*) micro-porphyry; UTM4983680N, 12513620E; sampled from easternmost intrusive phase on the north side of Electric Peak east cirque; porphyritic-aphanitic, holocrystalline, inequigranular with aplitic finer-grained matrix, predominately medium-grained; crystals of plagioclase feldspar (46.5%), potassium feldspar (14.5%), quartz (8.7%), biotite (2.2%), and opaque minerals (0.2%). Larger phenocrysts of plagioclase, quartz, and biotite are set in aplitic matrix of orthoclase, quartz, and biotite. Plagioclase feldspar is sub-to-predominately euhedral and pervasively sericitized. Orthoclase is anhedral, interstitial, and intimately associated with quartz. Quartz is anhedral, larger crystals (0.3-0.9mm) are rectangular with embayments filled with melt. Large quartz crystals commonly have rings of melt inclusions near crystal faces, are eustructural with high integrity, and are micropoikilitic. Biotite is anhedral and almost pervasively altering to chlorite. Secondary calcite is also present. *Modal abundances are semi-quantitative as potassium feldspar was estimated while other minerals were point-counted. In the field EP9712 occasionally intrudes EP9713 as very thin (1 to 2 mm wide, 1 to 2 cm long) dikes.

EP9713: Biotite-bearing, orthopyroxene-clinopyroxene quartz diorite (*modified TAS*) micro-porphyry; UTM: 4983670N, 12513590E; sampled from second easternmost intrusive phase on the north side of Electric Peak east cirque; porphyritic, trachytic, seriate, holocrystalline with microcrystalline groundmass; phenocrysts of plagioclase feldspar (12.0%), clinopyroxene (10.8%), orthopyroxene (5.2%), opaque minerals (3.2%), biotite (1.3%), sparse quartz, and trace apatite set in a microcrystalline groundmass consisting of opaque minerals, apatite(?), quartz, potassium feldspar(?), and plagioclase feldspar. Mafic crystal clots are abundant and consist of biotite, clinopyroxene, orthopyroxene, and opaque minerals. Possibly a cumulate?

EP9714*: Biotite-amphibole granodiorite (*I.U.G.S.*) micro-porphyry; UTM: 4983660N, 12513560E; sampled from third easternmost intrusive phase on the north side of Electric Peak east cirque; porphyritic-aphanitic, holocrystalline, seriate (0.15 to 2.25 mm), fine-to-medium-grained; phenocrysts of plagioclase feldspar (54.8%), quartz (16.5), amphibole (12.4%), biotite (8.7%), potassium feldspar (8.0%), opaque minerals (0.2%), and trace sphene in matrix of microphenocrysts and microcrystalline groundmass. Plagioclase feldspar is predominately subhedral (smaller crystals) while larger crystals are euhedral and is pervasively saussertized. Potassium feldspar is fine-grained (0.3 mm), anhedral, and interstitial between plagioclase feldspar and quartz. Quartz is fine-grained (0.1 to 0.8 mm), anhedral, filling larger interstices between plagioclase feldspar crystal crystals, and commonly contains opaque minerals. Biotite is usually subhedral, fine-to-medium in grain size (0.1 to 1.8 mm), and associated in crystal clots with amphibole and opaque minerals. Amphibole (0.1 to 2.5 mm) is sub-to-eustructural with poor integrity and converting to biotite and opaque minerals. *Modal abundances are semi-quantitative as potassium feldspar was estimated while other minerals were point-counted. In the field EP9714 shares a narrow (0.3 m thick) gradational compositional contact with EP9713.

EP9715*: Amphibole-biotite granodiorite (*I.U.G.S.*) micro-porphyry; UTM: 4983640N, 12513540E; sampled from intrusion on north side of Electric Peak east cirque; holocrystalline, porphyritic, strong magmatic fabric; crystals of plagioclase feldspar (56.3%), quartz (25.6%), potassium feldspar (8.4%), biotite (5.4%), amphibole (3.1%), and opaque minerals (1.2 %). Plagioclase feldspar is sub-to-euhedral and strongly aligned. Amphibole is eustructural with poor integrity and is converting to biotite, opaque minerals, and plagioclase. Biotite is an-to-euhedral. Both quartz and potassium feldspar are anhedral and interstitial between plagioclase feldspar laths. Potassium feldspar is often pervasively sericitized. *Modal abundances are semi-quantitative as potassium feldspar was estimated while other minerals were point-counted. In the field EP9715 cuts EP9714 with a sharp compositional contact.

EP9716*: Biotite-amphibole quartz diorite (*I.U.G.S.*) micro-porphyry; UTM: 4978560N, 12517550E; sampled from knob just south of "hill 9803"; holocrystalline, porphyritic, weak magmatic fabric; crystals of plagioclase feldspar (46,4%), amphibole (25.9%), biotite (12.4%), quartz (10.5%), potassium feldspar (3.1%), and opaque minerals (1.7%); trace amounts of clinopyroxene, zircon, zoisite, and apatite are present. Quartz and potassium feldspar are anhedral and interstitial between plagioclase feldspar laths. Amphibole is eustructural with medium integrity. *Modal abundances are semi-quantitative as potassium feldspar was estimated while other minerals were point-counted.

EP9717*: Biotite-amphibole quartz diorite (*I.U.G.S.*) micro-porphyry; UTM: 4984230N, 12513630E; sampled from knob just southwest of "hill 9803"; holocrystalline, porphyritic, fine-to-medium grained, weak magmatic fabric; crystals of plagioclase feldspar (58.1%), amphibole (14.0%), quartz (13.0%), biotite (9.8%), opaque minerals (2.8%), and potassium feldspar (2.3%), clinopyroxene is rare. Plagioclase feldspar is sub-to-euhedral and strongly aligned. Amphibole is eustructural with poor integrity and is converting to biotite, opaque minerals, and plagioclase. Biotite is an-to-euhedral. Both quartz and potassium feldspar are anhedral and interstitial between plagioclase feldspar laths. Mafic crystal clots of amphibole, biotite, opaque minerals, and occasionally orthopyroxene are abundant. *Modal abundances are semi-quantitative as potassium feldspar was estimated while other minerals were point-counted.

EP9718*: Amphibole-bearing, biotite granodiorite (*I.U.G.S.*) micro-porphyry; UTM: 4984200N, 12513900E; sampled from knob southeast of "hill 9803"; holocrystalline, porphyritic; crystals of plagioclase feldspar (56.3%), quartz (23.7%), potassium feldspar (12.2%), biotite (5.2%), amphibole (1.3%), and opaque minerals (1.3%). Trace amounts of zoisite, apatite, and zircon (as inclusion in biotite) are present. Potassium feldspar is pervasively sericitized. Quartz and potassium feldspar are anhedral and interstitial between plagioclase feldspar laths. Amphibole is predominately eustructural with poor integrity. Occasional crystals of amphibole have a line of opaque crystals just within their crystal faces and are cored by biotite. *Modal abundances are semi-quantitative as potassium feldspar was estimated while other minerals were point-counted.

EP9719*: Amphibole-biotite tonalite (*I.U.G.S.*) micro-porphyry; UTM: 4984370N, 12513910E; sampled from apophyses trending north from intrusive phase EP9718; holocrystalline, porphyritic, strong magmatic fabric; crystals of plagioclase feldspar (59.4%), quartz (17.5%), biotite (11.1%), amphibole (7.0%), opaque minerals (3.0%), and potassium feldspar (2.0%). Trace amounts of apatite are present. Secondary silica and epidote are present in small quantities. Plagioclase feldspar is predominately subhedral. Quartz and potassium feldspar are predominately anhedral and interstitial between feldspar laths. Biotite contains numerous opaque mineral inclusions. Large eustructural amphibole crystals are present and in chemical disequilibrium, converting to biotite and opaque minerals. Pyroxene-cored, amphibole-rimmed, biotite and opaque mineral crystal clots are abundant. *Modal abundances are semi-quantitative as potassium feldspar was estimated while other minerals were point-counted.

EP9720: Amphibole-biotite tonalite (*I.U.G.S.*) micro-porphyry; UTM: 4983130N, 12513400E; sampled from largest intrusive phase on south side of Electric Peak east cirque; holocrystalline, mostly subhedral-granular, consertal; crystals of plagioclase feldspar (60.8%), quartz (19.5%), biotite (7.9%), potassium feldspar (6.1%), amphibole (4.7%), and opaque minerals (1.0%). Rare crystals of sphene are present. Mafic crystal clots of biotite, amphibole, and opaque minerals are abundant. Amphibole is commonly eustructural with poor integrity and is in chemical disequilibrium, converting to biotite and opaque minerals. Amphibole is very similar in appearance to amphibole found in samples EP9830 and EP9847 which are magmatic inclusions.

EP9830: Plagioclase hornblendite (*I.U.G.S.*) inclusion; UTM: 4983660N, 12513560E; sampled from intrusive phase EP9714 on north side of Electric Peak east cirque; holocrystalline, medium-grained, inequigranular; crystals of amphibole (64.5%), plagioclase feldspar (31.1%), quartz (3.9%), and opaque minerals (0.5%). Trace amounts of zoisite are present. Amphibole crystals are eustructural with low integrity and are commonly converting to biotite and opaque minerals. Plagioclase locally exhibits poikilitic texture with plagioclase oikiocrysts containing amphibole chadacrysts. Plagioclase exhibits compositional zoning. Quartz, and some plagioclase appears to have crystallized at a later time than amphibole.

EP9832: Amphibole-bearing, biotite granite (*I.U.G.S.*) micro-porphyry; UTM: 4984380N, 12513380E; sampled on ridge trending northeast from summit of Electric Peak approximately 1.5 km from summit; holocrystalline, fine-to-medium-grained, subhedral granular, granophyric; crystals of plagioclase feldspar (32.2%), potassium feldspar (32.2%), quartz (26.9%), biotite (4.7%), amphibole (1.7%), and opaque minerals (0.9%). Plagioclase feldspar is mostly subhedral with compositionally zoned rims, but compositionally homogenous cores. Potassium feldspar is anhedral and intimately associated with quartz filling interstices between plagioclase feldspar laths. Biotite is predominately subhedral and uniquely associated with amphibole and opaque minerals. Amphibole is substructural with low integrity and is converting to biotite and opaque minerals. Quartz exhibits vermicular intergrowths into potassium feldspar.

EP9840: Amphibole-bearing, biotite rhyolite (*TAS*) dike; UTM: 4983110N, 12513340E; sampled from apophyses west of EP9720 on south side of Electric Peak east cirque; hypocrystalline with microcrystalline groundmass, porphyritic; phenocrysts of plagioclase feldspar (47.9%), quartz (8.9%), biotite (4.0%), and amphibole (1.0%). Plagioclase feldspar is euhedral, biotite is subhedral, and amphibole is eustructural with poor integrity. Amphibole is converting to biotite, chlorite, opaque minerals, and calcite. Quartz is eustructural with medium integrity and has an embayed and boxy cellular structure. Potassium feldspar is very fine grained (<0.1 mm) and comprises about half of the microcrystalline groundmass.

EP9845: Amphibole-bearing, biotite granodiorite (*I.U.G.S.*) micro-porphyry dike; UTM: 4983450N, 12513270E; sampled from apophyses on west wall of Electric Peak east cirque; holocrystalline, porphyritic, fine-to-medium-grained; crystals of plagioclase feldspar (49.0%), quartz (21.9%), potassium feldspar (14.4%), biotite (10.5%), amphibole (2.5%), and opaque minerals (1.7%). Trace orthopyroxene, apatite, zoisite, alunite, and zircon are present. Quartz and potassium feldspar are anhedral and interstitial with an aplitic texture. Mafic crystal clots of amphibole, biotite, and opaque minerals are common.

EP9846: Amphibole-bearing, biotite granite (*I.U.G.S.*) micro-porphyry dike; UTM: 4983590N, 12513490E; sampled from intrusive phase which cuts EP9714 on north side of Electric Peak east cirque; holocrystalline, porphyritic, fine-to-medium-grained; crystals of plagioclase feldspar (41.6%), quartz (26.9%), potassium feldspar (23.5%), biotite (5.8%), opaque minerals (1.2%), and amphibole (1.0%). Amphibole is anstructural with low integrity and is uniquely associated with biotite. Quartz and potassium feldspar are anhedral and interstitial between plagioclase feldspar laths. EP9846 cuts EP9714, the contact is characterized by a sharp compositional contact with phase segregation parallel to the contact.

EP9847: Plagioclase hornblendite (*I.U.G.S.*) inclusion; UTM: 4983660N, 12513550E; sampled from EP9714 on north side of Electric Peak east cirque; holocrystalline medium-grained, inequigranular; crystals of amphibole (79.4%), plagioclase feldspar (18.1%), quartz (1.9%), and opaque minerals (0.6%). Amphibole crystals are eustructural with medium integrity and are commonly converting to biotite and opaque minerals. Plagioclase locally exhibits poikilitic texture with plagioclase oikiocrysts containing amphibole chadacrysts. Plagioclase exhibits compositional zoning. Quartz, and some plagioclase are interstitial and appear to have crystallized after amphibole.

EP9850: Biotite-amphibole granodiorite (*I.U.G.S.*) micro-porphyry dike; UTM: 4983630N, 12513510E; sampled from late stage dike which cuts EP9846 and EP9714 on the north side of Electric Peak east cirque; holocrystalline, porphyritic, fine-to-medium-grained; crystals of sub-to-euhedral sericitized plagioclase feldspar (41.6%), anhedral quartz (20.6%), anhedral potassium feldspar (17.2%), substructural with low structural integrity amphibole (10.5%), subhedral biotite (9.3%), and opaque minerals (0.8%). Trace amounts of zoisite, apatite, and zircon are present. Amphibole is in chemical disequilibrium and is converting to biotite and opaque minerals. Quartz and potassium feldspar are interstitial between plagioclase feldspar laths. Quartz locally exists as poikilitic domains enclosing all other mineral phases. EP9850 cuts EP9846 and EP9714.

APPENDIX B

FELDSPAR COMPOSITIONS

Appendix B. Feldpsar compositions.

Sample	Point	Remark	SiO_2	Al_2O_3	Na_2O	FeO*	MgO	BaO	CaO	K_2O	Total
EP97-14.A	1	Core	65.08	18.33	1.09	0.16	0.00	0.06	0.01	15.21	99.95
EP97-14.A	3	Core	65.05	18.38	0.86	0.12	0.00	0.10	0.00	15.42	99.94
EP97-14.A	6	Core	64.36	18.34	0.00	0.02	0.00	0.32	0.00	16.67	99.71
EP97-14.A	7	Core	64.56	18.50	1.28	0.06	0.00	0.01	0.03	15.02	99.47
EP97-14.A	10	Core	64.39	18.72	2.05	0.14	0.00	0.15	0.03	13.88	99.35
EP97.14.B	2	Intermediate	64.26	19.03	1.72	0.09	0.00	1.14	0.04	13.96	100.25
EP97.14.D	1	Intermediate	64.01	19.04	0.95	0.01	0.00	1.12	0.00	15.08	100.22
EP97.14.E	2	Intermediate	63.69	18.80	0.12	0.00	0.00	0.42	0.00	16.43	99.46
EP97.14.B.1	1	Core	59.10	26.18	6.79	0.20	0.00	0.09	7.72	0.50	100.58
EP97.14.E	1	Core	57.40	27.06	6.28	0.20	0.00	0.03	8.69	0.37	100.03
EP97-14.A	9	Core	55.42	27.94	5.60	0.29	0.00	0.12	9.95	0.30	99.61
EP97.14.B.1	2	Intermediate	58.56	26.57	6.67	0.23	0.00	0.09	8.17	0.39	100.68
EP97.14.B.1	3	Intermediate	58.89	24.55	7.31	0.26	0.00	0.12	6.40	0.45	97.98
EP97.14.B.1	4	Intermediate	59.23	26.15	6.81	0.24	0.00	0.11	7.66	0.41	100.61
EP97-14.A	5	Intermediate	58.78	25.81	6.73	0.29	0.00	0.20	7.57	0.44	99.82
EP97-14.A	8	Intermediate	56.76	27.14	6.19	0.31	0.00	0.07	8.96	0.33	99.77
EP97.14.B	3	Rim	65.14	22.33	9.26	0.18	0.00	0.01	3.26	0.66	100.85
EP97.14.B.1	5	Rim	61.86	24.23	8.01	0.16	0.00	0.14	5.44	0.58	100.41
EP97.14.D	2	Rim	65.99	21.82	9.75	0.14	0.00	0.04	2.57	0.56	100.87
EP98-45.A	3	Core	63.82	19.28	2.92	0.07	0.00	0.95	0.19	12.01	99.25
EP98-45.A	1	Core	55.64	27.97	5.65	0.17	0.00	0.04	9.75	0.28	99.51
EP98-45.A	2	Core	55.65	27.96	5.73	0.23	0.00	0.05	9.90	0.28	99.80
EP98-45.A	4	Core	62.46	23.15	8.71	0.13	0.00	0.03	4.49	0.46	99.44
EP98-45.E	1	Core	56.95	26.97	6.22	0.38	0.10	0.10	8.53	0.45	99.70
EP98-45.C	1	Intermediate	58.74	26.17	6.82	0.16	0.00	0.06	7.81	0.35	100.11
EP98-45.C	2	Intermediate	58.37	26.55	6.48	0.18	0.00	0.12	8.21	0.38	100.29
EP98-45.E	2	Intermediate	57.75	26.72	6.59	0.17	0.00	0.05	8.29	0.43	100.01
SM97-21.A.1	1	Core	52.67	29.32	4.26	0.74	0.08	0.04	12.24	0.25	99.60
SM97-21.A.2	1	Core	53.13	29.22	4.43	0.59	0.09	0.06	12.12	0.31	99.96
SM97-21.B.1	1	Core	53.72	28.72	4.81	0.60	0.07	0.08	11.31	0.34	99.64
SM97-21.B.2	1	Core	53.98	28.76	4.77	0.67	0.06	0.07	11.54	0.32	100.16
SM97-21.C.1	1	Core	51.99	29.52	4.18	0.59	0.07	0.07	12.45	0.26	99.13
SM97-21.C.2	1	Core	54.42	28.07	5.04	0.59	0.07	0.03	10.90	0.35	99.48

Note: FeO* = all Fe reported as Fe^{2+}.

Appendix B: continued.

Sample	Analysis pt	Remark	SiO_2	Al_2O_3	Na_2O	FeO*	MgO	BaO	CaO	K_2O	Total
SM97-21.D.2	1	Core	53.76	29.21	4.63	0.64	0.09	0.02	11.83	0.28	100.45
SM97-21.D	1	Intermediate	52.00	30.41	3.85	0.64	0.07	0.05	13.24	0.21	100.46
SM97-21.A.1	2	Intermediate	51.82	30.24	3.97	0.69	0.06	0.01	12.94	0.24	99.99
SM97-21.A.2	2	Intermediate	52.79	29.43	4.43	0.58	0.05	0.05	12.01	0.27	99.62
SM97-21.B.1	2	Intermediate	53.22	29.59	4.50	0.59	0.07	0.05	12.11	0.24	100.38
SM97-21.B.2	2	Intermediate	53.70	29.04	4.59	0.61	0.08	0.06	11.82	0.29	100.19
SM97-21.C.1	2	Intermediate	50.72	30.15	3.71	0.57	0.07	0.03	13.32	0.18	98.76
SM97-21.C.2	2	Intermediate	52.34	29.73	4.08	0.60	0.06	0.05	12.76	0.25	99.87
SM97-21.D.2	2	Intermediate	52.59	30.24	3.90	0.67	0.07	0.04	13.01	0.21	100.72
SM97-21.A.2	3	Intermediate	52.64	29.92	4.06	0.58	0.07	0.04	12.73	0.26	100.31
SM97-21.A.2	4	Intermediate	55.19	26.52	5.03	1.34	0.21	0.10	9.82	0.46	98.68
SM97-21.A.1	3	Rim	51.42	30.03	3.90	0.70	0.07	0.02	13.07	0.23	99.43
SM97-21.B.1	3	Rim	51.61	30.30	3.78	0.63	0.09	0.01	13.33	0.21	99.96
SM97-21.C.1	3	Rim	51.85	29.35	4.28	0.63	0.07	0.03	12.52	0.22	98.95
SM97-21.C.2	3	Rim	52.28	29.84	4.07	0.65	0.06	0.04	12.62	0.25	99.81
SM97-21.A.2	5	Rim	51.57	30.02	3.70	0.59	0.06	0.04	13.14	0.22	99.35
SM97-21.B.2	5	Rim	51.79	28.85	3.94	1.14	0.22	0.04	12.38	0.27	98.63
SM97-24.A.1	1	Core	57.90	26.63	6.58	0.52	0.01	0.11	8.27	0.37	100.39
SM97-24.A.2	1	Core	56.23	28.13	5.67	0.29	0.00	0.05	9.84	0.24	100.46
SM97-24.A.3	1	Core	56.57	26.66	6.37	0.32	0.00	0.07	8.24	0.32	98.56
SM97-24.B.1	1	Core	55.00	28.29	5.67	0.29	0.01	0.04	9.95	0.22	99.47
SM97-24.B.2	1	Core	56.50	27.16	6.27	0.23	0.00	0.07	8.69	0.28	99.20
SM97-24.B.3	1	Core	59.65	25.46	6.96	0.41	0.01	0.19	7.10	0.50	100.26
SM97-24.C.1	1	Core	56.30	27.78	5.87	0.26	0.00	0.07	9.54	0.33	100.16
SM97-24.C.2	1	Core	57.72	25.88	6.58	0.32	0.02	0.12	7.76	0.39	98.78
SM97-24.D.1	1	Core	56.92	27.65	5.92	0.25	0.01	0.07	9.28	0.27	100.36
SM97-24.C.2	2	Interemediate	59.78	25.57	6.99	0.31	0.02	0.13	7.16	0.47	100.43
SM97-24.D.1	2	Interemediate	56.06	27.73	5.85	0.27	0.00	0.06	9.35	0.25	99.55
SM97-24.A.1	2	Intermediate	59.26	24.45	7.22	0.41	0.02	0.26	5.93	0.64	98.20
SM97-24.A.2	2	Intermediate	54.26	28.16	5.62	0.28	0.01	0.08	10.02	0.23	98.67
SM97-24.A.3	2	Intermediate	54.37	28.11	5.62	0.25	0.00	0.06	9.74	0.24	98.41
SM97-24.B.1	2	Intermediate	56.02	27.42	5.95	0.26	0.00	0.10	9.17	0.24	99.16
SM97-24.B.2	2	Intermediate	55.92	27.13	6.16	0.22	0.00	0.06	8.86	0.29	98.65

Note: FeO* = all Fe reported as Fe^{2+}.

Appendix B: continued.

Sample	Analysis pt	Remark	SiO_2	Al_2O_3	Na_2O	FeO*	MgO	BaO	CaO	K_2O	Total
SM97-24.B.3	2	Intermediate	58.32	26.05	6.74	0.46	0.02	0.15	7.70	0.45	99.88
SM97-24.B.3	3	Intermediate	60.15	25.09	7.03	0.34	0.00	0.15	6.65	0.55	99.97
SM97-24.B.3	4	Intermediate	59.78	25.31	7.15	0.24	0.00	0.12	6.83	0.52	99.98
SM97-24.C.1	2	Intermediate	56.21	27.26	6.13	0.32	0.00	0.04	8.93	0.36	99.24
SM97-24.C.2	3	Intermediate	59.74	25.46	7.06	0.34	0.01	0.14	6.78	0.55	100.08
SM97-24.D.1	4	Intermediate	57.67	27.20	6.31	0.21	0.00	0.06	8.60	0.29	100.34
SM97-24.A.2	3	Rim	56.41	27.44	5.87	0.29	0.00	0.05	9.42	0.32	99.79
SM97-24.A.3	3	Rim	58.07	24.88	6.97	0.32	0.00	0.15	6.86	0.48	97.72
SM97-24.B.1	3	Rim	55.34	27.38	5.77	0.24	0.01	0.02	9.29	0.32	98.38
SM97-24.B.3	5	Rim	60.85	24.72	7.38	0.28	0.02	0.15	6.30	0.55	100.23
SM97-24.C.1	3	Rim	60.27	25.14	7.21	0.34	0.01	0.21	6.37	0.54	100.10
SM97-24.D.1	5	Rim	58.73	25.39	7.36	0.26	0.00	0.17	6.81	0.50	99.23
SM97-35.A.1	1	Core	58.24	24.92	7.35	0.34	0.01	0.17	6.35	0.52	97.89
SM97-35.A.2	1	Core	55.45	26.61	6.50	0.45	0.00	0.10	8.51	0.40	98.03
SM97-35.A.3	1	Core	55.00	26.91	6.15	0.31	0.01	0.08	8.82	0.35	97.63
SM97-35.B.1	1	Core	55.28	27.13	6.08	0.44	0.01	0.10	9.03	0.33	98.40
SM97-35.B.2	1	Core	57.10	25.86	6.92	0.42	0.00	0.11	7.77	0.41	98.60
SM97-35.C.1	1	Core	56.35	25.82	6.73	0.27	0.02	0.11	7.64	0.46	97.41
SM97-35.C.2	1	Core	57.33	26.66	6.29	0.20	0.00	0.05	8.39	0.29	99.21
SM97-35.C.3	1	Core	55.94	28.01	5.78	0.28	0.01	0.10	9.79	0.29	100.21
SM97-35.D.1	1	Core	55.70	26.53	6.32	0.21	0.00	0.08	8.25	0.38	97.48
SM97-35.D.1	3	Core	57.65	25.60	6.94	0.31	0.00	0.14	7.27	0.43	98.34
SM97-35.D.2	1	Core	55.58	27.07	6.27	0.30	0.00	0.12	8.74	0.31	98.40
SM97-35.A.1	2	Intermediate	56.55	25.48	6.77	0.35	0.00	0.12	7.47	0.41	97.16
SM97-35.A.2	2	Intermediate	56.14	26.51	6.51	0.38	0.03	0.12	8.15	0.35	98.18
SM97-35.A.2	3	Intermediate	57.25	25.65	6.85	0.34	0.00	0.14	7.36	0.39	97.98
SM97-35.A.2	4	Intermediate	58.06	24.78	7.44	0.35	0.01	0.13	6.42	0.51	97.71
SM97-35.A.3	2	Intermediate	56.75	25.68	6.80	0.35	0.02	0.10	7.49	0.46	97.65
SM97-35.B.1	2	Intermediate	54.79	26.20	6.12	0.42	0.02	0.10	8.43	0.41	96.49
SM97-35.B.1	3	Intermediate	55.71	26.66	6.24	0.39	0.01	0.13	8.79	0.42	98.36
SM97-35.B.1	4	Intermediate	57.12	25.60	6.91	0.41	0.00	0.16	7.45	0.51	98.16
SM97-35.B.2	2	Intermediate	57.49	25.39	7.10	0.23	0.01	0.12	7.00	0.41	97.74
SM97-35.C.1	2	Intermediate	59.25	24.41	7.82	0.35	0.01	0.11	5.98	0.54	98.47

Note: FeO* = all Fe reported as Fe^{2+}.

Appendix B: continued.

Sample	Analysis pt	Remark	SiO_2	Al_2O_3	Na_2O	FeO*	MgO	BaO	CaO	K_2O	Total
SM97-35.C.2	2	Intermediate	56.37	26.41	6.55	0.21	0.00	0.03	8.23	0.28	98.09
SM97-35.C.3	2	Intermediate	55.83	26.48	6.52	0.34	0.01	0.13	8.22	0.32	97.84
SM97-35.C.3	3	Intermediate	57.38	25.64	6.96	0.30	0.00	0.11	7.34	0.44	98.17
SM97-35.C.3	4	Intermediate	58.22	25.22	7.25	0.31	0.00	0.11	6.83	0.44	98.37
SM97-35.D.1	2	Intermediate	57.61	25.45	7.09	0.14	0.00	0.11	6.93	0.51	97.84
SM97-35.D.2	2	Intermediate	56.77	26.10	6.84	0.31	0.02	0.11	7.73	0.40	98.29
SM97-35.A.1	3	Rim	57.13	25.57	6.99	0.27	0.00	0.10	7.31	0.41	97.79
SM97-35.A.2	5	Rim	56.98	25.63	6.99	0.26	0.00	0.05	7.20	0.43	97.56
SM97-35.A.3	3	Rim	56.42	25.95	6.83	0.31	0.00	0.11	7.51	0.37	97.50
SM97-35.B	3	Rim	56.55	25.88	6.97	0.26	0.00	0.08	7.63	0.37	97.75
SM97-35.B.1	5	Rim	57.83	25.21	7.16	0.23	0.00	0.11	6.81	0.43	97.80
SM97-35.C.1	3	Rim	58.81	25.64	7.15	0.26	0.02	0.08	7.40	0.39	99.74
SM97-35.C.2	3	rim	58.62	25.58	7.18	0.21	0.00	0.12	7.11	0.42	99.25
SM97-35.C.3	5	Rim	57.07	25.68	6.86	0.24	0.00	0.09	7.46	0.37	97.76
SM97-35.D.2	3	Rim	57.94	25.51	7.18	0.22	0.00	0.11	7.20	0.42	98.59
SM97-40.A.1	1	Core	55.49	28.13	5.73	0.12	0.01	0.06	9.92	0.28	99.74
SM97-40.A.1	4	Core	55.92	25.65	6.07	0.19	0.00	0.09	8.03	0.51	96.46
SM97-40.A.2	1	Core	56.78	26.36	6.41	0.25	0.00	0.13	8.34	0.37	98.65
SM97-40.A.3	1	Core	55.40	28.05	5.32	0.22	0.00	0.08	10.12	0.27	99.46
SM97-40.B.1	1	Core	56.02	27.46	5.76	0.17	0.00	0.08	9.14	0.33	98.96
SM97-40.B.2	1	Core	56.14	27.92	5.74	0.16	0.00	0.06	9.68	0.28	99.98
SM97-40.C.2	1	Core	55.30	28.18	5.54	0.18	0.00	0.08	10.28	0.26	99.82
SM97-40.C.3	1	Core	56.49	27.25	5.89	0.17	0.00	0.07	8.95	0.30	99.13
SM97-40.D.1	1	Core	51.15	30.36	3.99	0.34	0.00	0.03	13.06	0.18	99.11
SM97-40.E.1	1	Core	54.86	28.22	5.21	0.17	0.00	0.07	10.22	0.25	99.01
SM97-40.E.2	1	Core	55.47	27.73	5.49	0.33	0.00	0.11	9.88	0.26	99.27
SM97-40.A.1	2	Intermediate	55.36	27.62	5.69	0.23	0.00	0.07	9.69	0.27	98.93
SM97-40.A.1	3	Intermediate	55.09	28.21	5.51	0.17	0.01	0.03	10.11	0.24	99.37
SM97-40.A.2	2	Intermediate	55.28	27.06	5.78	0.34	0.02	0.15	9.16	0.30	98.10
SM97-40.A.2	3	Intermediate	56.71	26.77	5.99	0.29	0.00	0.16	8.79	0.36	99.06
SM97-40.A.2	4	Intermediate	57.71	25.74	6.80	0.28	0.00	0.18	7.58	0.45	98.75
SM97-40.A.3	2	Intermediate	55.54	26.88	5.72	0.24	0.00	0.08	9.22	0.37	98.06
SM97-40.B.1	2	Intermediate	55.15	28.60	5.34	0.25	0.00	0.08	10.57	0.22	100.21

Note: FeO* = all Fe reported as Fe^{2+}.

Appendix B: continued.

Sample	Analysis pt	Remark	SiO_2	Al_2O_3	Na_2O	FeO*	MgO	BaO	CaO	K_2O	Total
SM97-40.B.2	2	Intermediate	55.68	27.58	5.70	0.20	0.00	0.09	9.70	0.27	99.23
SM97-40.C.2	2	Intermediate	54.42	28.78	5.01	0.19	0.00	0.05	10.95	0.23	99.64
SM97-40.C.2	3	Intermediate	54.41	29.03	5.04	0.22	0.00	0.03	10.79	0.23	99.75
SM97-40.C.2	4	Intermediate	56.66	27.28	6.00	0.18	0.00	0.13	8.95	0.33	99.52
SM97-40.C.3	2	Intermediate	56.94	26.25	6.19	0.17	0.00	0.11	7.96	0.44	98.06
SM97-40.D.1	2	Intermediate	51.81	30.43	4.10	0.26	0.01	0.01	12.93	0.15	99.71
SM97-40.D.1	3	Intermediate	54.63	28.32	5.10	0.30	0.01	0.10	10.40	0.26	99.13
SM97-40.D.1	4	Intermediate	52.63	29.94	4.33	0.24	0.00	0.04	12.30	0.18	99.66
SM97-40.D.1	5	Intermediate	53.37	29.26	4.77	0.22	0.00	0.09	11.63	0.21	99.55
SM97-40.D.1	6	Intermediate	53.67	29.04	4.78	0.30	0.01	0.04	11.29	0.25	99.37
SM97-40.A.1	5	Rim	57.30	26.42	6.23	0.16	0.00	0.07	8.21	0.33	98.73
SM97-40.A.2	5	Rim	57.75	26.18	6.50	0.20	0.00	0.14	8.00	0.40	99.17
SM97-40.A.3	3	Rim	57.02	26.76	6.11	0.31	0.00	0.10	8.55	0.37	99.22
SM97-40.B.1	3	Rim	56.91	27.58	6.08	0.20	0.00	0.09	8.89	0.34	100.09
SM97-40.B.2	3	Rim	56.19	27.93	5.68	0.21	0.00	0.10	9.69	0.29	100.09
SM97-40.C.2	5	Rim	56.22	27.42	5.81	0.20	0.00	0.11	9.30	0.33	99.39
SM97-40.C.3	3	Rim	57.63	26.46	6.28	0.26	0.00	0.11	8.36	0.37	99.49
SM97-40.D.1	7	Rim	58.43	25.64	6.61	0.29	0.00	0.15	7.60	0.41	99.13
SM97-40.E.1	2	Rim	56.29	26.90	5.84	0.21	0.00	0.11	9.17	0.31	98.83
SM97-40.E.2	2	Rim	57.07	26.35	6.17	0.25	0.00	0.14	8.35	0.38	98.72
SM98-14.A.1	1	Core	56.62	27.10	6.00	0.31	0.06	0.10	9.03	0.37	99.60
SM98-14.A.2	1	Core	56.01	28.02	5.63	0.29	0.00	0.08	9.82	0.28	100.13
SM98-14.A.3	1	Core	53.22	29.32	4.93	0.24	0.01	0.04	11.37	0.23	99.35
SM98-14.B.1	1	Core	55.46	28.48	5.43	0.34	0.00	0.10	10.49	0.25	100.56
SM98-14.B.3	1	Core	57.37	26.63	6.25	0.23	0.00	0.10	8.35	0.36	99.29
SM98-14.C.1	1	Core	57.05	27.05	6.05	0.31	0.01	0.12	8.92	0.40	99.91
SM98-14.C.2	1	Core	58.87	25.77	6.82	0.18	0.01	0.02	7.33	0.45	99.46
SM98-14.C.3	1	Core	52.91	29.15	4.82	0.36	0.00	0.06	11.29	0.37	98.96
SM98-14.C.4	1	Core	57.54	26.28	6.34	0.30	0.03	0.11	8.11	0.42	99.12
SM98-14.D.1	1	Core	60.11	24.43	7.33	0.19	0.00	0.07	6.02	0.52	98.68
SM98-14.D.2	1	Core	55.28	27.78	5.81	0.26	0.00	0.06	9.80	0.29	99.29
SM98-14.D.3	1	Core	57.06	26.76	6.33	0.27	0.00	0.04	8.45	0.33	99.25
SM98-14.E.1	1	Core	60.79	24.00	7.84	0.24	0.00	0.12	5.54	0.53	99.06

Note: FeO* = all Fe reported as Fe^{2+}.

Appendix B: continued.

Sample	Analysis pt	Remark	SiO_2	Al_2O_3	Na_2O	FeO*	MgO	BaO	CaO	K_2O	Total
SM98-14.E.2	1	Core	55.33	27.42	5.86	0.23	0.01	0.04	9.32	0.26	98.46
SM98-14.A.1	2	Intermediate	54.09	29.04	4.85	0.44	0.03	0.05	11.39	0.23	100.11
SM98-14.A.2	2	Intermediate	54.17	27.15	5.62	0.26	0.01	0.07	9.61	0.36	97.24
SM98-14.A.3	2	Intermediate	56.97	27.00	5.83	0.28	0.07	0.07	9.12	0.33	99.67
SM98-14.B.1	2	Intermediate	53.94	29.28	4.89	0.35	0.00	0.06	11.37	0.18	100.07
SM98-14.B.1	3	Intermediate	55.38	28.14	5.62	0.30	0.00	0.08	10.06	0.26	99.86
SM98-14.B.1	4	Intermediate	53.79	29.23	5.04	0.34	0.00	0.09	11.08	0.20	99.76
SM98-14.B.3	2	Intermediate	58.22	26.18	6.66	0.27	0.00	0.10	7.72	0.40	99.55
SM98-14.C.1	2	Intermediate	51.95	29.81	4.51	0.22	0.00	0.06	12.01	0.20	98.77
SM98-14.C.1	3	Intermediate	55.90	27.44	6.00	0.24	0.00	0.10	9.13	0.38	99.19
SM98-14.C.1	4	Intermediate	54.27	29.05	4.97	0.35	0.00	0.03	11.22	0.30	100.19
SM98-14.C.2	2	Intermediate	56.44	26.97	6.07	0.27	0.00	0.05	8.86	0.38	99.04
SM98-14.C.4	2	Intermediate	59.40	25.26	7.11	0.21	0.00	0.10	6.68	0.55	99.30
SM98-14.D.1	2	Intermediate	57.46	26.72	6.35	0.32	0.00	0.04	8.09	0.36	99.33
SM98-14.D.2	2	Intermediate	59.17	25.40	7.34	0.23	0.00	0.05	6.50	0.48	99.18
SM98-14.D.2	3	Intermediate	59.41	25.33	7.13	0.29	0.00	0.13	6.84	0.48	99.61
SM98-14.D.2	4	Intermediate	58.83	25.36	7.01	0.20	0.01	0.07	7.11	0.48	99.07
SM98-14.D.3	2	Intermediate	59.40	24.88	7.16	0.24	0.00	0.09	6.36	0.53	98.66
SM98-14.E.1	2	Intermediate	59.16	25.04	7.31	0.22	0.01	0.08	6.54	0.46	98.81
SM98-14.E.2	2	Intermediate	55.64	27.57	5.89	0.22	0.00	0.01	9.31	0.27	98.91
SM98-14.A.1	3	Rim	56.54	27.34	5.77	0.37	0.00	0.05	9.52	0.32	99.91
SM98-14.A.2	3	Rim	56.74	26.39	6.49	0.30	0.00	0.06	8.05	0.37	98.39
SM98-14.A.3	3	Rim	55.50	27.54	5.78	0.40	0.02	0.07	9.59	0.30	99.19
SM98-14.B	4	Rim	58.02	25.93	6.80	0.35	0.00	0.14	7.54	0.41	99.20
SM98-14.B.1	5	Rim	58.25	25.83	7.01	0.35	0.00	0.14	7.25	0.43	99.25
SM98-14.B.3	3	Rim	57.74	26.61	6.57	0.29	0.01	0.05	8.22	0.37	99.87
SM98-14.C	5	Rim	56.32	26.95	5.82	0.30	0.04	0.06	8.66	0.42	98.58
SM98-14.C	6	Rim	58.00	25.94	6.55	0.32	0.00	0.11	7.74	0.47	99.13
SM98-14.C.1	5	Rim	54.24	27.64	5.06	0.36	0.13	0.06	9.97	0.39	97.85
SM98-14.C.2	3	Rim	56.19	27.68	5.67	0.43	0.01	0.10	9.68	0.33	100.08
SM98-14.C.4	3	Rim	56.44	26.84	6.26	0.40	0.01	0.09	8.51	0.40	98.95
SM98-14.D	4	Rim	57.61	26.09	6.60	0.26	0.00	0.11	7.79	0.45	98.90
SM98-14.D.1	3	Rim	58.13	26.86	6.24	0.23	0.00	0.08	8.45	0.35	100.35

Note: FeO* = all Fe reported as Fe^{2+}.

Appendix B: continued.

Sample	Analysis pt	Remark	SiO_2	Al_2O_3	Na_2O	FeO*	MgO	BaO	CaO	K_2O	Total
SM98-14.D.2	5	Rim	56.30	27.18	5.91	0.33	0.00	0.10	8.98	0.36	99.15
SM98-14.D.3	3	Rim	59.24	25.21	7.20	0.22	0.00	0.08	6.61	0.50	99.07
SM98-14.E	3	Rim	55.59	27.34	5.82	0.30	0.03	0.09	9.19	0.30	98.65
SM98-14.E.1	3	Rim	56.14	27.07	6.25	0.26	0.01	0.06	8.58	0.32	98.71
SM98-14.E.2	3	Rim	56.22	26.77	6.18	0.38	0.01	0.08	8.62	0.38	98.65
SM98-25.A.1	1	Core	53.41	29.35	4.44	0.59	0.07	0.07	11.84	0.30	100.08
SM98-25.B	1	Core	54.07	29.11	4.56	0.64	0.07	0.07	11.53	0.29	100.34
SM98-25.C	1	Core	51.77	30.29	3.84	0.68	0.07	0.10	12.76	0.24	99.75
SM98-25.D.1	1	Core	52.89	28.99	4.52	0.65	0.08	0.07	11.56	0.31	99.07
SM98-25.D.2	1	Core	52.11	30.32	3.94	0.54	0.05	0.03	13.01	0.24	100.23
SM98-25.A.1	2	Intermediate	51.68	29.54	4.28	0.65	0.06	0.08	12.37	0.27	98.93
SM98-25.D.1	2	Intermediate	54.42	28.62	4.92	0.57	0.06	0.07	11.13	0.33	100.11
SM98-25.D.2	2	Intermediate	53.10	29.31	4.31	0.68	0.09	0.07	11.93	0.28	99.78
SM98-25.A.1	3	Rim	51.23	29.61	4.31	0.63	0.06	0.05	12.10	0.26	98.26
SM98-25.D.1	3	Rim	52.21	30.48	3.92	0.74	0.05	0.03	13.19	0.24	100.86
SM98-25.D.2	3	Rim	52.19	30.92	3.85	0.75	0.08	0.04	13.03	0.21	101.07

Note: FeO* = all Fe reported as Fe^{2+}.

APPENDIX C

PYROXENE COMPOSITIONS

Appendix C. Pyroxene compositions.

Sample	Point	Remark	SiO_2	TiO_2	Al_2O3	Cr_2O_3	Fe_2O_3*	FeO*	MnO	MgO	CaO	Na_2O	Total
SM97-21.C	2	Core	53.75	0.2	1.73	0.13	3.23	11.6	0.29	28.56	1.28	0	100.78
SM97-21.C	3	Core	55.13	0.21	0.48	0.07	1.55	15.45	0.4	27.09	1.54	0	101.92
SM97-21.D	1	Core	54.83	0.22	0.72	0.05	2	15.21	0.37	26.98	1.62	0	102
SM97-21.D	5	Core	54.43	0.33	1.39	0.06	1.73	15.97	0.41	26.3	1.65	0	102.27
SM97-21.A.3	1	Core	53.95	0.31	1	0.04	2.88	15.06	0.42	26.36	1.79	0	101.82
SM97-21.A.3	2	Core	53.71	0.33	1.46	0.06	2.26	16.12	0.42	25.59	1.84	0	101.79
SM97-21.B.1	1	Core	51.83	0.63	2.04	0.04	2.73	7.37	0.32	15.83	19.75	0.29	100.84
SM97-21.B.2	2	Core	51.87	0.51	1.9	0.06	3.07	7.1	0.31	15.81	19.79	0.33	100.76
SM97-21.B	4	Core	52.19	0.53	1.98	0.09	2.38	7.4	0.28	15.99	19.83	0.28	100.94
SM97-21.B.1	2	Core	51.32	0.65	2.61	0.1	3.38	7.03	0.26	15.46	19.81	0.37	101.01
SM97-21.D	4	Core	52.48	0.34	2.5	0.36	2.67	5.03	0.22	17.02	20.35	0.3	101.26
SM97-21.C.1	1	Core	51.09	0.71	2.87	0.06	2.29	8.62	0.27	14.39	19.83	0.39	100.52
SM97-21.D	2	Core	51.79	0.53	1.91	0.07	2.98	6.21	0.22	16.06	20.44	0.25	100.46
SM97-21.C	4	Core	51.06	0.67	3.78	0.18	2.61	5.95	0.21	15.98	20.08	0.28	100.81
SM97-21.B.2	1	Core	52.27	0.35	2.08	0.25	2.88	4.58	0.18	16.86	21.19	0.18	100.83
SM97-21.C.1	2	Core	50.83	0.5	4.14	0.09	2.68	6.88	0.23	14.76	20.43	0.35	100.88
SM97-21.D	3	Core	52.43	0.4	2.31	0.63	2.44	3.92	0.2	17.12	21.35	0.23	101.03
SM97-21.A.3	3	Rim	54.48	0.23	0.83	0.05	1.68	15.64	0.4	26.54	1.56	0	101.42
SM97-21.B.1	3	Rim	52.41	0.43	1.76	0.03	2.15	7.18	0.33	16.21	20.08	0.2	100.78
SM97-21.B.2	3	Rim	52.36	0.49	2.06	0.04	2.93	6.08	0.24	16.3	20.77	0.23	101.49
SM97-21.C.1	3	Rim	51.23	0.57	2.51	0.06	3.42	5.83	0.21	15.89	20.6	0.22	100.55
SM98-14.B.1	1	Core	52.59	0.1	1.85	0.03	2.62	19.47	0.74	23.61	0.47	0.01	101.49
SM98-14.B.1	2	Core	52.48	0.09	1.88	0.01	2.43	19.6	0.78	23.39	0.51	0.02	101.19
SM98-14.A	2	Core	53.36	0.23	1.02	0.01	1.62	18.34	0.7	24.76	0.56	0.03	100.61
SM98-14.D	1	Rim	53.76	0.13	0.97	0.01	0.5	18.86	0.75	24.65	0.57	0.02	100.24
SM98-14.D	2	Rim	53.73	0.11	1.15	0.02	0.85	18.69	0.7	24.73	0.61	0.02	100.6
SM98-14.A	3	Rim	54.53	0.12	0.41	0.01	1.03	17.16	0.63	26	0.82	0.03	100.73
SM98-14.A	1	Rim	52.04	0.17	1.48	0.05	2.6	17.84	0.71	23.61	1.25	0.03	99.78
SM98-25.B	2	Core	53.28	0.2	2.56	0.02	2.53	13.39	0.33	27.14	1.25	0.04	100.74
SM98-25.A.2	2	Core	53.02	0.19	1.98	0.08	3.75	12.4	0.31	27.53	1.32	0.02	100.59
SM98-25.B.1	2	Core	53.2	0.15	2.28	0.11	3.79	11.66	0.27	27.97	1.37	0.04	100.86

Note: Fe_20_3*, FeO*: Fe^{2+} and Fe^{3+} calculated by charge balance.

Appendix C: continued.

Sample	Point	Remark	SiO_2	TiO_2	Al_2O3	Cr_2O_3	Fe_2O_3*	FeO*	MnO	MgO	CaO	Na_2O	Total
SM98-25.A.2	1	Core	53.03	0.19	2.17	0.13	3.78	11.67	0.28	27.9	1.42	0.02	100.6
SM98-25.B.1	1	Core	55.04	0.12	2.12	0.36	1.26	11.53	0.21	29.25	1.48	0.03	101.41
SM98-25.A.1	2	Core	52.88	0.22	1.04	0.01	2.91	14.05	0.33	26.23	1.66	0.04	99.35
SM98-25.A.1	1	Core	53.49	0.23	0.84	0.01	2.3	14.73	0.36	26.17	1.75	0.04	99.92
SM98-25.B	3	Core	52.62	0.17	2.39	0.18	4.87	9.57	0.27	28.32	1.91	0.06	100.37
SM98-25.D	4	Core	52.74	0.21	1.61	0.3	2.73	3.7	0.17	18.17	20	0.3	99.92
SM98-25.D	5	Core	53.7	0.21	1.64	0.34	1.67	4.78	0.18	18.08	20.08	0.32	101
SM98-25.D.6	1	Core	53.05	0.18	1.62	0.35	2.76	3.79	0.19	17.65	20.73	0.34	100.66
SM98-25.D	2	Core	52.86	0.23	1.96	0.38	2.46	4.19	0.17	17.41	20.57	0.36	100.58
SM98-25.D	3	Core	51.48	0.53	2.22	0.03	3.1	5.87	0.21	15.9	20.4	0.32	100.06
SM98-25.D	1	Core	51.77	0.23	2.1	0.36	3.99	2.87	0.15	17.29	20.89	0.32	99.98
SM98-25.A	6	Core	51.5	0.33	2.4	0.13	3.78	3.85	0.16	16.47	20.92	0.37	99.92
SM98-25.A	4	Core	51.87	0.54	3.11	0.1	2.92	5.51	0.17	15.77	21.04	0.38	101.41
SM98-25.C	1	Core	52.04	0.25	2.03	0.66	3.08	2.57	0.14	17.41	21.17	0.34	99.69
SM98-25.B.1	3	Rim	53.71	0.15	1.66	0.06	3.01	12.71	0.37	27.78	1.26	0.03	100.74
SM98-25.A.2	3	Rim	53.42	0.22	2.42	0.08	1.85	15.83	0.32	25.78	1.34	0.06	101.31
SM98-25.A	3	Rim	52.96	0.25	1.46	0	3.58	13.41	0.35	26.8	1.47	0.03	100.33
SM98-25.A.1	3	Rim	51.76	0.26	1.49	0.01	4.54	12.38	0.37	26.52	1.52	0.04	98.89
SM98-25.D.6	3	Rim	51.14	0.51	2.08	0.03	3.46	5.52	0.22	15.72	20.55	0.33	99.56

Note: Fe_20_3*, FeO*: Fe^{2+} and Fe^{3+} calculated by charge balance.

APPENDIX D

AMPHIBOLE COMPOSITIONS

Appendix D. Amphibole compositions.

Sample	Point	Remark	SiO_2	Al_2O_3	FeO*	Fe_2O_3*	MgO	CaO	Na_2O	K_2O	TiO_2	Cr_2O_3	MnO	Cl	F	Sum	H_2O*
EP97-14	1	Rim	51.1	4.95	8.23	3.38	16.44	10.99	1.27	0.27	0.8	0.09	0.34	0.06	0	97.91	2.09
EP97-14.A.1	2	Rim	50.06	5.82	8.42	3.46	16.29	11.13	1.36	0.33	0.93	0.04	0.38	0.03	0	98.24	1.75
EP97-14.A.4	1	Rim	50.96	5.02	7.94	3.26	17.11	11.11	1.16	0.28	0.74	0	0.29	0.07	0.23	98.06	1.95
EP97-14.B.1	1	Rim	49.48	6.15	8.2	3.37	16.48	11.15	1.45	0.37	1.07	0.02	0.4	0.06	0.16	98.28	1.72
EP97-14.B.3	1	Rim	51.3	4.86	7.97	3.28	16.77	11.05	1.18	0.27	0.79	0.01	0.41	0.04	0	97.92	2.08
SM97-24.A.1	1	Core	44.76	11.02	8.69	3.57	14.91	11.08	2.01	0.49	1.6	0	0.12	0.03	0.17	98.37	1.63
SM97-24.A.1	3	Rim	44.33	11.41	9.34	3.84	14.17	10.95	1.99	0.46	1.65	0	0.19	0.03	0.27	98.51	1.49
SM97-24.A.2	1	Rim	45.08	10.88	8.29	3.41	15.45	11	2.04	0.43	1.5	0.06	0.14	0.04	0.28	98.47	1.53
SM97-24.B.1	1	Core	43.33	10.7	9.24	3.8	13.85	10.95	2.13	1.04	3.15	0.01	0.16	0.08	0.19	98.53	1.47
SM97-24.B.1	3	Core	44.36	10.97	9.45	3.88	14.15	10.86	2.09	0.71	1.69	0.07	0.2	0.08	0.22	98.62	1.38
SM97-24.B.2	1	Core	44.02	11.01	9.43	3.88	13.92	10.81	2.05	0.8	1.61	0.05	0.22	0.06	0.19	97.96	2.05
SM97-24.B.2	3	Rim	44.36	10.38	9.13	3.75	14.24	10.77	2.02	0.8	2.27	0.01	0.17	0.06	0.4	98.18	1.83
SM97-24.B.3	1	Core	46.77	9.71	6.73	2.77	16.97	10.96	1.97	0.39	1.33	0.16	0.09	0.03	0.16	97.97	2.04
SM97-24.C.1	1	Core	47.63	9.3	6.03	2.48	17.83	10.85	1.93	0.42	1.25	0.43	0.13	0.01	0.2	98.4	1.6
SM97-24.C.2	1	Core	45.55	10.3	8.77	3.61	14.92	10.9	1.87	0.4	1.54	0	0.19	0.05	0.22	98.22	1.78
SM97-24.D.2	1	Rim	46.33	10.08	7.73	3.18	15.68	10.66	1.94	0.48	1.39	0.09	0.13	0.03	0.5	98	2
SM97-35.A.1	1	Core	46.87	8.13	8.8	3.62	15.46	11.05	1.7	0.59	1.9	0.02	0.18	0.07	0.26	98.52	1.48
SM9735.B.1	1	Core	45.61	9.2	9.05	3.72	14.51	11.07	1.82	0.91	1.91	0.04	0.17	0.12	0.3	98.28	1.72
SM97-35.D.1	1	Core	44.26	11.27	8.33	3.42	15.13	10.91	2.22	0.58	1.93	0.02	0.13	0.02	0.39	98.44	1.56
SM97-35.D.2	1	Core	43.67	11.96	10.11	4.16	13.66	10.24	2.1	0.52	1.76	0	0.16	0.04	0.27	98.53	1.48
SM97-35.D.3	1	Core	42.13	12.69	10.9	4.48	12.41	10.61	2.21	0.61	1.86	0.01	0.1	0.05	0.13	98.12	1.88
SM97-35.D.3	3	Rim	42	12.44	11.21	4.61	12.25	10.77	2.14	0.53	2.06	0	0.14	0.06	0.12	98.27	1.74
SM97-35.C.1	1	Core	43.52	10.92	9.53	3.92	13.92	11.03	2.16	0.62	2.17	0.06	0.25	0.03	0.27	98.28	1.73
SM97-35.C.1	3	Rim	47.95	7.11	8.38	3.44	16.32	11.11	1.56	0.46	1.61	0.01	0.31	0.06	0.31	98.49	1.51
SM97-40.A.3	1	Core	44.97	9.96	8.46	3.48	14.99	11.14	1.97	0.58	2.15	0.01	0.2	0.03	0.3	98.11	1.89
SM97-40.A.4	1	Core	44.22	11.52	8.38	3.44	15.09	10.66	2.03	0.77	1.74	0.03	0.15	0.03	0.3	98.23	1.77
SM97-40.B.1	3	Rim	43.67	12.19	9.76	4.01	13.54	10.87	1.96	0.55	1.35	0.06	0.16	0.05	0.21	98.28	1.72
SM97-40.B.2	1	Core	43.55	11.83	8.75	3.59	14.57	10.87	2.23	0.8	1.97	0.02	0.12	0.01	0.36	98.52	1.48
SM97-40.C.1	1	Core	44.4	9.15	10.69	4.4	13.48	10.89	1.8	0.94	2.32	0.01	0.19	0.1	0.19	98.46	1.54
SM97-40.C.2	1	Core	47.35	7.4	10.29	4.23	14.28	10.97	1.4	0.66	1.26	0	0.29	0.1	0.24	98.35	1.65
SM97-40.C.3	1	Core	44	11.6	8.45	3.47	14.85	10.81	2.1	0.84	1.86	0	0.15	0	0.15	98.22	1.79
SM97-40.C.3	5	Rim	44.28	10.57	8.27	3.4	15.08	11.14	2.08	0.69	1.97	0	0.27	0.08	0.37	98.03	1.97

Note: H_20* = water calculated by difference; Fe_2O_3* and FeO* = Fe^{2+} and Fe^{3+} were calculated on the assumption that $Fe^{+3}/(Fe^{+2} + Fe^{+3}) = 0.27$.

Appendix D: continued.

Sample	Point	Remark	SiO_2	Al_2O_3	FeO*	Fe_2O_3*	MgO	CaO	Na_2O	K_2O	TiO_2	Cr_2O_3	MnO	Cl	F	Sum	H_2O*
SM97-40.E.3	1	Core	44.38	10.68	8.62	3.54	15.03	11.04	2	0.64	1.97	0.01	0.19	0.03	0.09	98.18	1.82
SM98-14.A.1	3	Rim	46.98	9.58	7.72	3.17	16.72	11.03	1.67	0.46	0.45	0.19	0.13	0.02	0.24	98.25	1.74
SM98-14.A.3	1	Core	44.59	10.65	8.82	3.62	14.57	11.17	1.86	0.67	1.72	0.07	0.2	0.06	0.12	98.06	1.94
SM98-14.A.4	1	Core	44.57	10.32	9.36	3.85	14.45	10.82	1.84	0.5	1.83	0.03	0.23	0.03	0.27	97.98	2.03
SM98-14.A.4	3	Rim	43.3	12.04	9.35	3.84	13.74	10.73	2.13	0.64	1.8	0.01	0.17	0.05	0.4	98.02	1.97
SM98-14.B.1	1	Core	42.71	12.36	9.56	3.93	13.14	11	1.94	0.73	2.3	0	0.19	0.03	0.33	98.07	1.93
SM98-14.B.2	1	Core	48.71	7.65	9.05	3.72	15.25	10.29	1.43	0.38	1.21	0.03	0.33	0.08	0.26	98.26	1.73
SM98-14.B.3	1	Core	44.41	10.44	9.99	4.1	13.88	10.81	1.75	0.66	1.9	0.04	0.24	0.05	0.27	98.42	1.58
SM98-14.C.1	1	Core	43.6	11.96	9.36	3.85	13.78	10.66	2.16	0.54	1.69	0.02	0.19	0.05	0.2	97.96	2.04
SM98-14.C.1	2	Rim	45.91	9.2	8.77	3.6	15.28	11.12	1.69	0.53	1.96	0.03	0.22	0.07	0.4	98.6	1.4
SM98-14.D.1	1	Core	47.83	7.68	9.11	3.74	15.66	10.54	1.53	0.42	1.35	0.02	0.32	0.09	0.22	98.4	1.6
SM98-14.D.3	1	Core	44.48	11.08	8.05	3.31	15.38	10.94	2.07	0.52	1.98	0.02	0.15	0.03	0.26	98.15	1.84
SM98-14.E.2	1	Core	43.69	11.76	8.16	3.35	14.96	11.03	2.12	0.6	1.97	0.04	0.11	0.02	0.29	97.97	2.02
SM98-14.E.4	1	Rim	43.94	11.29	9.08	3.73	14.3	11.06	2.06	0.55	1.82	0	0.25	0.05	0	98.12	1.88

Note: H_20* = water calculated by difference; Fe_2O_3* and FeO* = Fe^{2+} and Fe^{3+} were calculated on the assumption that $Fe^{+3}/(Fe^{+2} + Fe^{+3}) = 0.27$.

APPENDIX E

MAGNETITE COMPOSITIONS

Appendix E. Magnetite compositions.

Sample	SiO_2	TiO_2	Fe_2O_3*	FeO*	MnO	MgO	Al_2O_3	V_2O_3	ZnO	Cr_2O_3	Sum Ox%	%Ulv	%Mt
SM97-21 N1_4	0.13	6.11	52.44	33.72	0.5	1.11	1.77	0.36	0.22	0.21	96.56	46.05	53.95
SM97-24 N1_3	0.09	6.22	51.73	33.96	0.47	0.77	1.57	0.25	0.16	0.11	95.33	46.39	53.61
SM97-24 N1_4	0.4	6.08	50.6	34.1	0.41	0.75	1.55	0.29	0.12	0.17	94.48	46.72	53.28
SM97-24 N2_3	0.62	6.1	50.9	34.49	0.4	1.02	1.81	0.32	0.14	0.09	95.89	46.79	53.21
SM97-24 N3_4	0.06	6.05	52.08	34.03	0.44	0.71	1.79	0.26	0.14	0.07	95.61	46.26	53.74
SM97-24 N3_5	0.11	6.2	51.97	34.16	0.48	0.76	1.77	0.32	0.21	0.03	96.01	46.39	53.61
SM97-24 N3_5	0.15	6.12	52	34.19	0.43	0.73	1.68	0.33	0.21	0.01	95.86	46.36	53.64
SM97-24 N4_3	0.94	6.03	50.29	35.04	0.45	0.83	1.64	0.35	0.12	0.08	95.77	47.14	52.86
SM97-24 N4_5	0.19	5.87	51.97	33.91	0.48	0.65	1.6	0.34	0.18	0.08	95.26	46.18	53.82
SM97-24 N5_4	0.6	6.42	49.99	35.05	0.41	0.76	1.74	0.33	0.1	0.13	95.55	47.36	52.64
SM97-24 N5_5	0.08	6.49	51.46	34.47	0.45	0.73	1.66	0.34	0.2	0.13	96	46.75	53.25
SM97-24 N6_6	0.34	6.28	50.69	34.41	0.41	0.7	1.61	0.36	0.2	0.08	95.07	46.88	53.12
SM97-24 N6_7	0.06	6.4	51.07	34.35	0.41	0.61	1.67	0.28	0.18	0.14	95.17	46.79	53.21
SM97-35 N1_2	0.16	5.09	56.71	33.59	0.44	0.91	0.97	0.22	0.21	0.04	98.33	44.45	55.55
SM97-35 N1_5	0.94	3.04	56.15	32.56	0.26	0.43	0.84	0.26	0.14	0.07	94.69	43.45	56.55
SM97-35 N1_6	0.87	3.2	55.68	32.23	0.23	0.52	0.83	0.27	0.27	0.07	94.17	43.49	56.51
SM97-35 N2_4	0.72	3.12	56.48	32.16	0.19	0.53	0.92	0.23	0.21	0	94.56	43.21	56.79
SM97-35 N2_5	0.7	3.04	56.7	31.93	0.26	0.63	0.99	0.23	0.16	0	94.65	43.01	56.99
SM97-35 N2_6	0.83	3.07	55.75	31.99	0.21	0.57	0.93	0.21	0.15	0.01	93.71	43.32	56.68
SM97-35 N3_4	0.12	4.9	56.46	33.17	0.48	0.96	1.28	0.26	0.22	0.08	97.94	44.28	55.72
SM97-35 N3_5	0.47	4.46	56.31	33.31	0.43	0.85	1.12	0.25	0.18	0.08	97.46	44.23	55.77
SM97-35 N4_5	0.06	5.19	56.65	33.29	0.54	0.95	0.85	0.23	0.2	0.06	98.02	44.38	55.62
SM97-35 N4_6	0.97	3.48	55.8	32.73	0.35	0.57	0.78	0.27	0.33	0.06	95.35	43.78	56.22
SM97-35 N4_7	0.04	4.76	58.44	33.56	0.56	0.91	1.14	0.27	0.2	0.1	99.97	43.86	56.14
SM97-35 N4_8	0.03	4.1	59.32	33.11	0.49	0.82	1.22	0.3	0.11	0.07	99.58	43.21	56.79
SM97-35 N5_5	0.15	4.99	56.89	33.64	0.47	0.98	1.27	0.27	0.13	0.08	98.87	44.39	55.61
SM97-35 N5_6	0.04	5.11	57.15	33.69	0.46	0.96	1.32	0.24	0.23	0.06	99.26	44.38	55.62
SM97-35 N5_7	0.02	5.18	57.14	33.72	0.47	1.05	1.34	0.27	0.13	0.06	99.39	44.42	55.58
SM97-40 N1_4	0.04	5.34	56.48	33.14	0.79	1.36	1.92	0.19	0.21	0	99.49	44.42	55.58
SM97-40 N1_5	0.05	5.08	56.83	32.95	0.8	1.31	1.96	0.12	0.18	0	99.28	44.15	55.85
SM97-40 N1_6	0.02	5.43	56.36	33.11	0.86	1.4	1.98	0.17	0.18	0	99.5	44.47	55.53

Note: Fe_2O_3*, FeO*: Fe^{+3} and Fe^{+3} calculated by charge balance; binary end-members normalized to 100%.

Appendix E: continued.

Sample	SiO_2	TiO_2	Fe_2O_3*	FeO*	MnO	MgO	Al_2O_3	V_2O_3	ZnO	Cr_2O_3	Sum Ox%	%Ulv	%Mt
SM97-40 N1_7	0.05	4.99	56.84	32.81	0.75	1.29	1.9	0.17	0.25	0.01	99.04	44.06	55.94
SM97SM98-14 N1_	0.12	6.16	54.02	33.44	0.34	1.94	2.18	0.29	0.16	0.07	98.73	45.51	54.49
SM97SM98-14 N1_	0.28	5.91	53.79	33.61	0.42	1.74	2.26	0.28	0.08	0.01	98.36	45.56	54.44
SM97SM98-14 N1_	0.09	6.26	53.89	33.5	0.33	1.96	2.21	0.31	0.12	0.04	98.7	45.60	54.40
SM97SM98-14 N1_	0.22	6	53.71	33.44	0.37	1.85	2.25	0.23	0.09	0.02	98.19	45.54	54.46
SM97SM98-14 N2_	0.53	6.54	49.18	35.18	0.28	0.71	2.13	0.3	0.1	0.08	95.02	47.69	52.31
SM97SM98-14 N2_	0.56	6.64	49.26	35.29	0.3	0.78	2.12	0.31	0.17	0.11	95.53	47.73	52.27
SM97SM98-14 N3_	0.08	6.29	53.5	33.78	0.38	1.71	2.23	0.31	0.14	0.08	98.49	45.83	54.17
SM97SM98-14 N4_	0.06	6.13	54.69	33.52	0.33	1.99	2.19	0.29	0.12	0.09	99.41	45.34	54.66
SM97SM98-14 N6_	0.04	6.48	54.09	33.93	0.35	1.99	2.28	0.33	0.05	0.07	99.62	45.79	54.21

Note: Fe_2O_3*, FeO*: Fe^{+3} and Fe^{+3} calculated by charge balance; binary end-members normalized to 100%.

APPENDIX F

ILMENITE COMPOSITIONS

Appendix F. Ilmenite compositions.

Sample	SiO_2	TiO_2	Fe_2O_3*	FeO*	MnO	MgO	Al_2O_3	V_2O_3	Cr_2O_3	ZnO	Sum Ox%	%Hem	%Ilm
SM97-21 N1 Ti	0.04	32	37.36	25.77	0.82	1.21	0.26	0.07	0.06	0.06	97.66	39.27	60.73
SM97-21 N1_2	0.04	31.29	38.41	25.26	0.76	1.17	0.26	0.14	0.1	0.09	97.52	40.45	59.55
SM97-21 N1_3	0.01	33.22	36.14	26.63	0.87	1.33	0.22	0.08	0.05	0	98.55	37.65	62.35
SM97-24 N1_1	0.22	35.02	29.34	28.98	0.57	1.21	0.24	0.09	0.06	0.05	95.79	31.43	68.57
SM97-24 N1_2	0.16	36.23	27.65	28.73	1.31	1.49	0.31	0	0.07	0.07	96.01	29.86	70.14
SM97-24 N2_1	0.01	35.27	31.68	28.29	0.63	1.55	0.22	0	0.03	0.05	97.73	33.26	66.74
SM97-24 N2_2	0.02	34.97	31.72	27.92	0.74	1.57	0.21	0.04	0.04	0	97.22	33.53	66.47
SM97-24 N4_2	0.62	36.72	26.86	30.51	0.77	1.37	0.29	0.06	0.06	0.04	97.3	28.55	71.45
SM97-24 N5_1	0.05	33.6	33.54	27.74	0.66	1.01	0.24	0.03	0.08	0.06	96.99	35.35	64.65
SM97-24 N5_2	0.05	33.43	33.77	27.61	0.71	1	0.24	0.09	0.06	0.02	96.99	35.62	64.38
SM97-24 N5_3	0.04	33.38	33.55	27.55	0.65	1.01	0.23	0.02	0.07	0.07	96.58	35.51	64.49
SM97-35 N1_1	0.01	40.25	24.47	30.81	0.97	2.43	0.1	0	0.01	0.1	99.14	25.61	74.39
SM97-35 N1_3	0.01	38.91	26.88	29.93	1.01	2.26	0.1	0	0.02	0.01	99.14	28.08	71.92
SM97-35 N1_4	0.02	38.79	27.06	29.8	0.96	2.28	0.1	0	0.03	0.08	99.1	28.29	71.71
SM97-35 N2_1	0	31.39	40.47	24.72	0.46	1.67	0.22	0	0.03	0.07	99.03	41.90	58.10
SM97-35 N2_2	0	33.22	37.5	25.97	0.58	1.82	0.15	0	0.01	0.08	99.33	38.78	61.22
SM97-35 N2_3	0	30.7	42.69	24.08	0.48	1.67	0.29	0	0.02	0.07	99.99	43.80	56.20
SM97-35 N3_1	0	35.27	33.5	27.84	0.8	1.69	0.13	0	0.04	0.06	99.34	34.68	65.32
SM97-35 N3_2	0.01	35.18	33.89	27.81	0.86	1.62	0.13	0.01	0.04	0.08	99.64	34.98	65.02
SM97-35 N3_3	0.03	34.91	33.74	27.58	0.82	1.65	0.1	0	0.02	0.08	98.94	35.06	64.94
SM97-35 N4_1	0.18	37.36	28.86	29.72	0.86	1.77	0.13	0	0.03	0.06	98.98	30.08	69.92
SM97-35 N4_3	0.01	36.18	32.13	28.56	0.85	1.69	0.1	0	0.06	0.13	99.7	33.17	66.83
SM97-35 N4_4	0.09	39.17	26.17	30.64	1	2.03	0.11	0	0.03	0.08	99.31	27.27	72.73
SM97-35 N5_1	0	37.94	29.39	30.05	0.66	1.9	0.15	0	0.01	0	100.1	30.18	69.82
SM97-35 N5_2	0	35.79	32.37	28.24	0.77	1.75	0.11	0	0.02	0.05	99.1	33.58	66.42
SM97-35 N5_3	0	37.14	30.68	29.3	0.67	1.85	0.15	0	0.02	0.13	99.94	31.59	68.41
SM97-35 N5_4	0.18	35.4	32.64	28.25	0.81	1.63	0.21	0	0.07	0.08	99.27	33.90	66.10
SM97-40 N1_1	0.01	31.74	40.81	24.93	0.52	1.72	0.31	0	0.04	0.03	100.11	41.86	58.14
SM97-40 N1_2	0.02	34.67	34.75	27.25	0.72	1.79	0.28	0	0.09	0.05	99.62	35.95	64.05
SM97-40 N1_3	0.03	32.68	38.33	26.22	0.59	1.45	0.29	0	0.01	0.04	99.65	39.42	60.58
SM97-40 N1_8	0	30.04	43.25	24.4	0.4	1.21	0.36	0.02	0.02	0.06	99.77	44.27	55.73

Note: Fe_2O_3*, FeO*: Fe^{+2} and Fe^{3+} calculated by charge balance; binary end-members normalized to 100%.

Appendix F: continued.

Sample	SiO_2	TiO_2	Fe_2O_3*	FeO*	MnO	MgO	Al_2O_3	V_2O_3	Cr_2O_3	ZnO	Sum Ox%	%Hem	%Ilm
SM98-14 N2_1	0.03	29.28	43.62	23.29	0.16	1.63	0.41	0.05	0.02	0	98.48	45.35	54.65
SM98-14 N2_2	0.03	29.24	43.86	23.23	0.16	1.63	0.41	0.09	0.05	0.03	98.73	45.53	54.47
SM98-14 N3_1	0.02	31.55	40.53	24.65	0.23	1.97	0.42	0	0.05	0	99.41	41.90	58.10
SM98-14 N4_1	0.09	29.74	42.04	23.19	0.23	1.92	0.4	0.09	0.1	0	97.79	44.27	55.73
SM98-14 N5_2	0.06	29.46	43.7	23.18	0.22	1.74	0.41	0.05	0.06	0.05	98.94	45.36	54.64

Note: Fe_2O_3*, FeO*: Fe^{+2} and Fe^{3+} calculated by charge balance; binary end-members normalized to 100%.

APPENDIX G

MAJOR AND TRACE ELEMENT CONCENTRATIONS OF EPSM ROCKS

Appendix G. Major and trace element concentrations of EPSM rocks.

Sample	SiO_2	TiO_2	Al_2O_3	Fe_2O_3*	MnO	MgO	CaO	Na_2O	K_2O	P_2O_5	Total	Ni	Cr	V	Ba	Rb	Sr	Zr	Y	Nb	Pb	Th	Sc
Type 1 Extrusive Rocks																							
SM9828	55.81	0.85	16.17	7.93	0.12	5.76	7.53	3.22	1.89	0.25	98.74	74	195	165	1364	38	642	137	16	9.1	13	2	21
SM9712	56.27	0.84	16.22	8.46	0.13	6.00	7.48	3.26	1.87	0.25	99.93	77	187	173	1348	36	647	150	16	9.3	11	5	19
SM9737	57.40	0.73	16.15	7.13	0.12	5.49	6.47	3.58	2.25	0.26	98.87	95	172	139	1567	46	856	170	15	7.9	20	4	19
SM9827	57.79	0.72	15.30	6.98	0.10	6.02	6.71	3.25	1.88	0.23	98.28	108	289	144	1639	29	846	123	14	6.5	21	10	22
SM9721	58.38	0.71	15.92	7.50	0.10	4.37	6.54	3.33	2.17	0.24	98.51	48	146	142	1383	37	775	149	15	7.2	17	5	21
SM9720	58.42	0.71	16.08	7.18	0.09	4.54	6.67	3.27	2.12	0.24	98.60	55	149	144	1440	39	784	149	14	7.5	15	6	20
SM9726	58.50	0.72	15.76	6.73	0.11	4.76	6.54	3.39	2.13	0.28	98.24	60	169	139	1394	36	779	149	16	8.8	14	6	25
SM9718	58.60	0.72	16.13	6.88	0.11	4.74	6.80	3.33	2.29	0.26	99.17	44	116	143	1388	38	762	151	15	8.4	17	7	22
SM9825	58.67	0.71	15.99	7.18	0.10	4.46	6.63	3.38	2.18	0.24	98.81	47	159	146	1415	37	769	129	15	6.8	15	6	24
SM9826	58.75	0.74	15.62	6.97	0.11	4.88	6.54	3.66	2.04	0.21	98.82	60	171	142	1551	34	727	133	17	7.8	16	0	24
SM9716	58.80	0.77	15.58	7.76	0.11	5.72	6.31	3.58	1.98	0.23	100.05	127	262	140	1291	37	718	150	15	7.7	17	5	14
SM9727	59.02	0.73	15.59	7.55	0.11	4.75	6.38	3.55	2.01	0.20	99.14	62	161	144	1491	34	728	146	15	6.8	16	5	18
SM9723	59.05	0.71	15.85	6.76	0.10	4.75	6.58	3.21	2.26	0.25	98.83	56	164	142	1408	36	787	149	15	8.4	15	5	20
SM9736	59.07	0.71	16.31	6.45	0.14	3.99	6.54	3.80	2.19	0.35	98.89	56	134	108	1947	40	930	216	18	14.1	17	8	21
SM9717	59.51	0.73	17.77	6.56	0.11	2.20	5.72	4.07	2.22	0.30	98.53	0	4	116	1499	48	801	178	18	9.3	17	5	18
SM9722	60.36	0.67	16.17	6.62	0.09	3.89	5.90	3.86	2.19	0.22	99.30	31	91	130	1451	36	780	150	14	6.9	20	5	21
SM9715	61.05	0.62	15.90	5.88	0.09	5.06	5.74	3.34	2.41	0.20	99.69	99	209	108	1436	48	791	154	12	7.1	20	5	14
SM9725	61.34	0.60	16.45	6.13	0.09	3.08	5.50	3.88	2.32	0.22	99.00	25	46	136	1549	35	837	152	13	7.4	26	5	18
SM9705	62.09	0.61	16.98	6.17	0.07	2.79	5.34	3.99	2.28	0.25	99.95	22	41	115	1756	38	970	166	13	7.1	27	6	16
SM9719	62.60	0.59	15.99	5.47	0.06	3.06	5.00	4.03	2.30	0.19	98.75	32	61	109	1578	42	742	154	12	6.7	20	5	13
SM9701	62.78	0.60	16.73	5.80	0.08	2.46	5.16	3.69	2.62	0.21	99.54	11	26	104	1489	41	782	150	13	7.2	23	6	15
SM9702	63.56	0.59	16.20	5.76	0.08	2.60	4.84	4.28	2.32	0.19	99.84	29	51	111	1699	41	750	155	13	7.0	21	5	16
SM9703	63.71	0.59	16.09	5.79	0.09	2.75	4.99	4.07	2.30	0.19	99.99	29	55	107	1551	41	729	153	12	6.3	22	5	16
SM9709	58.01	0.87	17.31	7.61	0.18	3.17	6.73	3.94	2.33	0.37	99.76	14	49	156	1955	45	1016	210	19	15.8	18	9	21
SM9706.1i	59.67	0.60	14.60	6.66	0.10	6.59	5.01	4.67	2.31	0.19	99.74	110	452	127	1736	43	485	130	11	5.8	15	6	13
Type 1 Intrusive Rocks																							
EP9720	57.49	0.68	15.79	7.53	0.11	6.20	6.83	3.75	2.06	0.22	99.91	82	224	149	1316	39	745	174	14	6.8	12	6	21
EP9716	57.77	0.67	15.09	7.57	0.12	6.55	6.64	3.74	1.93	0.25	99.57	108	305	123	1462	38	805	131	15	7.7	21	2	18
EP9713	58.38	0.72	15.37	8.03	0.12	5.65	6.70	3.50	2.02	0.22	99.91	67	193	154	1243	36	695	139	16	6.8	17	4	23
EP9719	60.20	0.66	15.84	6.92	0.10	4.79	5.92	4.19	1.94	0.21	100.08	57	130	128	1351	42	710	161	15	8.1	21	8	18
EP9715	60.85	0.60	17.15	6.75	0.10	3.21	5.70	3.94	2.15	0.24	100.02	30	65	103	1314	41	764	164	16	8.1	16	7	12
EP9714	61.59	0.55	15.69	5.89	0.08	4.59	5.21	3.93	2.28	0.21	99.42	69	184	108	1610	39	817	151	13	8.6	15	5	17

Note: Major element data are wt%, trace element data are ppm; all analyses by XRF, Fe_2O_3* = all Fe reported as Fe^{+3}.

Appendix G: continued.

Sample	SiO_2	TiO_2	Al_2O_3	Fe_2O_3*	MnO	MgO	CaO	Na_2O	K_2O	P_2O_5	Total	Ni	Cr	V	Ba	Rb	Sr	Zr	Y	Nb	Pb	Th	Sc
Type 2 Extrusive Rocks																							
SM9713	62.16	0.69	16.89	6.11	0.10	2.72	5.10	4.29	2.20	0.23	99.89	18	31	112	1575	67	617	215	19	10.6	25	10	15
SM9738	62.54	0.51	16.84	4.61	0.09	1.75	4.52	3.85	3.18	0.28	97.70	11	26	70	2034	62	858	188	14	8.6	26	5	9
SM9704	62.85	0.58	14.65	5.50	0.05	4.57	4.96	4.01	2.78	0.28	99.69	121	169	83	2779	42	1410	187	12	5.7	39	16	12
SM9814	63.53	0.52	16.24	4.36	0.07	2.50	4.47	4.33	2.15	0.17	97.91	21	57	79	1471	46	768	133	9	5.8	24	10	11
TLC9701	63.83	0.50	16.40	4.42	0.06	2.02	4.82	3.36	3.26	0.25	98.47	19	37	77	2226	52	1000	194	14	12.4	24	9	13
SM9740	63.84	0.46	16.58	3.97	0.07	1.51	4.04	4.29	2.72	0.25	97.32	13	15	58	2475	48	1295	198	11	7.1	35	10	10
SM9731	64.29	0.46	16.57	3.90	0.05	2.10	3.37	3.64	3.50	0.24	97.73	10	18	63	2430	52	978	187	10	7.2	34	8	11
SM9810	64.43	0.56	15.05	4.23	0.09	3.39	4.74	4.10	2.61	0.21	98.97	95	159	83	2277	42	1090	130	9	6.1	36	21	6
SM9732	65.70	0.46	16.49	4.00	0.05	1.54	3.81	4.17	3.10	0.24	99.16	13	20	64	2432	46	1179	192	11	7.3	33	9	8
Type 2 Intrusive Rocks																							
EP9850	65.27	0.48	15.77	3.80	0.06	2.64	4.10	3.76	3.19	0.16	98.84	40	101	68	2019	53	855	117	8	7.8	21	9	9
Type 3 Extrusive Rocks																							
SM9733	65.42	0.48	16.45	4.11	0.05	2.07	3.91	4.45	2.65	0.17	99.35	22	35	68	1575	49	706	151	10	6.7	22	6	14
SM9730	66.57	0.37	15.49	3.53	0.05	2.12	3.52	4.20	2.91	0.16	98.57	31	62	56	1714	52	716	144	8	7.1	24	6	11
SM9706.2i	66.92	0.38	15.32	3.83	0.06	2.93	3.31	4.79	2.48	0.13	99.77	56	146	60	1704	47	749	133	8	4.7	22	4	13
SM9734	67.07	0.42	15.81	3.61	0.04	1.84	3.53	4.33	2.66	0.15	99.09	25	50	72	1530	49	693	146	9	5.9	26	4	9
SM9724	68.43	0.36	16.03	2.88	0.05	1.12	3.30	4.66	2.56	0.13	99.23	25	29	60	1742	48	711	137	8	6.5	26	5	10
SM9735	68.95	0.39	15.58	2.89	0.03	1.26	3.18	4.37	2.65	0.13	99.14	15	17	54	1612	48	688	141	8	5.9	30	4	10
SM9706	69.35	0.32	15.39	2.92	0.04	2.06	2.15	5.38	2.58	0.11	100.01	38	81	53	1751	48	631	127	7	4.7	19	5	7
Type 3 Intrusive Rocks																							
EP9711	65.87	0.47	16.52	3.93	0.03	1.93	4.17	4.43	2.44	0.17	99.57	20	33	78	1556	72	813	156	10	6.2	12	5	13
EP9845	65.97	0.40	16.19	3.40	0.05	1.71	3.69	4.50	2.79	0.17	98.53	24	36	50	1814	51	837	132	8	7.7	13	12	11
EP9717	67.48	0.38	16.66	3.73	0.05	1.56	3.64	4.65	2.42	0.17	100.37	18	25	52	1894	45	833	156	9	6.9	19	6	3
EP9840	69.56	0.29	15.49	2.00	0.02	0.91	2.29	4.85	2.74	0.10	98.04	7	14	41	1912	50	752	105	4	5.5	9	8	0
EP9718	70.07	0.29	15.74	2.57	0.04	1.29	2.77	4.66	2.75	0.11	100.03	22	40	37	1835	49	763	138	6	5.5	17	5	4
EP9712	70.46	0.26	15.49	1.65	0.01	0.64	2.00	5.15	2.97	0.09	98.55	11	6	19	1860	42	787	127	6	6.4	15	3	3
EP9846	71.90	0.28	14.36	1.99	0.02	0.99	2.09	3.87	3.74	0.09	99.13	11	27	33	2758	56	591	115	4	4.9	18	1	2
EP9832	72.59	0.29	13.96	2.18	0.03	0.89	2.07	3.74	3.99	0.07	99.59	10	16	36	1780	70	333	128	7	6.9	24	11	3
Hornblende Gabbro Inclusions																							
EP9847	48.19	1.97	12.56	12.78	0.13	10.98	9.28	2.74	1.15	0.08	98.58	130	285	484	904	16	388	82	26	7.2	6	2	72
EP9830	50.35	1.49	12.01	11.20	0.16	11.12	8.96	2.67	1.15	0.13	98.12	121	387	359	916	18	424	67	23	6.0	8	5	61

Note: Major element data are wt%, trace element data are ppm; all analyses by XRF, Fe_2O_3* = all Fe reported as Fe^{+3}.

APPENDIX H

MINERAL/MELT PARTITION COEFFICIENTS FOR BASALTIC AND BASALTIC-ANDESITIC MELTS USED IN AFC MODELING

Appendix H. Mineral/melt partition coefficients for basaltic and basaltic-andesitic melts used in AFC modeling.

Element	Olivine	Clinopyroxene	Orthopyroxene	Plagioclase	Amphibole	Fe-Ti Oxides*
Rb	0.0225	0.034	0.022	0.1128	0.4175	0.15
Ba	0.065	0.039	0.059	0.43	1.01	0
Sr	0.02	0.06	0.04	1.83	0.46	0.11
Ni	17.45	7.75	5	0	6.8	27.1
Zr	0.012	0.2	0.18	0.048	1.032	0.422
Cr	0.7	34	10	0	12.5	153
Ti	0.02	0.4	0.2	0.04	1.5	70

Note: Mineral/melt partition coefficients represent average values from the GERM database;
Fe-Ti Oxides* = 34% ilmenite and 66% magnetite.

APPENDIX I

MINERAL/MELT PARTITION COEFFICIENTS USED IN CRUSTAL MELTING MODELS

Appendix I. Mineral/melt partition coefficients used in crustal melting models.

Element	Plagioclase	Clinopyroxene	Amphibole	Orthopyroxene	Magnetite	Ilmenite
La	0.28	0.02	0.26	0.10	0.66	0.01
Ce	0.25	0.04	0.63	0.02	0.71	1.19
Nd	0.19	0.17	1.24	0.02	0.93	0.96
Sm	0.14	0.46	2.38	0.02	1.20	0.69
Eu	2.11	0.41	3.65	0.09	0.44	0.40
Gd	3.72	0.04	0.88	5.00	0.07	0.10
Dy	0.11	0.78	3.08	2.63	1.60	0.37
Yb	0.13	0.64	1.31	0.80	0.44	0.55

Note: Mineral/melt partition coefficients represent average values from the GERM database.